



BRNO UNIVERSITY OF TECHNOLOGY

VYSOKÉ UČENÍ TECHNICKÉ V BRNĚ

FACULTY OF MECHANICAL ENGINEERING

FAKULTA STROJNÍHO INŽENÝRSTVÍ

INSTITUTE OF AUTOMOTIVE ENGINEERING

ÚSTAV AUTOMOBILNÍHO A DOPRAVNÍHO INŽENÝRSTVÍ

BLADELESS FAN COOLING MODULE

CHLADÍCÍ MODUL BEZLOPATKOVÉHO VENTILÁTORU

MASTER'S THESIS

DIPLOMOVÁ PRÁCE

AUTHOR

AUTOR PRÁCE

Bc. Adam

Šišpera

SUPERVISOR

VEDOUCÍ PRÁCE

Ing. Jiří Bazala

BRNO 2023

Assignment Master's Thesis

Institut: Institute of Automotive Engineering
Student: **Bc. Adam Šišpera**
Degree programm: Automotive and Material Handling Engineering
Branch: no specialisation
Supervisor: **Ing. Jiří Bazala**
Academic year: 2022/23

As provided for by the Act No. 111/98 Coll. on higher education institutions and the BUT Study and Examination Regulations, the director of the Institute hereby assigns the following topic of Master's Thesis:

Bladeless fan cooling module

Brief Description:

The fan currently used for aftercooling the car coolant exchanger is a blade type fan. Another possible solution may be a fan based on the principle of the Coand effect.

Master's Thesis goals:

Research on fans suitable for forced air circulation in car coolers.
Analysis of the requirements for the fan.
Necessary mass flow rate, air distribution, size, power analysis.
Comparison with a convection fan on a single cooler.

Recommended bibliography:

STONE, Richard. Introduction to internal combustion engines. 3rd edition. Warrendale, Pa.: Society of Automotive Engineers, 1999. 641 s. ISBN 0768004950.

Deadline for submission Master's Thesis is given by the Schedule of the Academic year 2022/23

In Brno,

L. S.

prof. Ing. Josef Štětina, Ph.D.
Director of the Institute

doc. Ing. Jiří Hlinka, Ph.D.
FME dean

ABSTRACT

This diploma thesis aims at researching the possibility of implementing a bladeless fan module, using Coanda effect, in a cooling system of a passenger vehicle. Its goal is to evaluate the feasibility of such system, its operational characteristic and establish a guideline for its design. A suitable cooling module is proposed, further examined, and finally proven in a real-world experiment.

KEYWORDS

Coanda effect, bladeless fan, computational fluid dynamics (CFD), efficiency, MQB cooler module, heat exchanger requirements, anemometer, measurement, experiment, CFX, ducting, mass flow, pressure, optimisation.

ABSTRAKT

Tato diplomová práce se zaměřuje na prozkoumání možností implementace bezlopatkového modulu ventilátoru založeného na Coanda efektu v chladícím systému osobního vozidla. Jejím cílem je prozkoumat proveditelnost takového řešení, jeho provozní charakteristiky a stanovit soubor doporučení pro návrh konkrétního designu. Vhodný chladící modul je navržen, následně hlouběji testován a jeho funkčnost je ověřena také reálným experimentem.

KLÍČOVÁ SLOVA

Coandův efekt, bezlopatkový ventilátor, výpočetní dynamika tekutin, účinnost, MQB chladící modul, požadavky tepelného výměníku, anemometr, měření, experiment, CFX, potrubí, hmotnostní tok, tlak, optimalizace.

BIBLIOGRAPHIC CITATION

Šišpera, A. *Bladeless fan cooling module*. Brno, 2023. Diploma thesis. Brno University of Technology, Faculty of Mechanical Engineering, Institute of Automotive Engineering. Supervisor Jiří Bazala. Available from: <https://www.vut.cz/studenti/zav-prace/detail/149999>



AFFIDAVIT

I declare that this diploma thesis is my original work, created under the supervision of Ing. Jiří Bazala and using the literature listed in sources at the end of this thesis.

In Brno 22nd of May 2023

.....

Adam Šišpera



ACKNOWLEDGEMENTS

I would like to thank my supervisor Ing. Jiří Bazala, for valuable notices and friendly behaviour throughout my work on this thesis. Hanon Systems Autopal in Hluk for providing me with access to their testing facility and measuring equipment. Ing. Jiří Vacula for providing insight into the Ansys CFX modelling and Tomáš Prejda for a technical consult of computational fluid dynamics problems. Last, but not least, I would like to thank my family for an outstanding level of support during my study efforts.

SUMMARY

Introduction.....	12
1 Cooling needs of a modern vehicle	13
1.1 Road going vehicle power requirement.....	13
1.1.1 Rolling resistance.....	13
1.1.2 Aerodynamic resistance	14
1.1.3 Total resistance	14
1.2 Heat dissipation	16
1.2.1 Radiation.....	16
1.2.2 Convection and conduction.....	17
1.3 Combustion engine efficiency.....	18
1.4 Battery electric vehicle powertrain efficiency.....	19
2 Current cooler design	21
3 Coanda effect.....	23
3.1 Historical references.....	23
3.1.1 Magnus effect.....	23
3.1.2 Coanda Effect.....	23
3.1.3 Distinction.....	23
3.2 Test subject.....	24
4 Experiment	26
4.1 Measurement methodises	26
4.2 Positioning system.....	27
4.3 Data collection.....	28
4.4 Data representation.....	28
4.5 Calibration.....	28
4.6 Conducted experiments	29
4.6.1 Default device with no additional accessories	30
4.6.2 Default device with ducting	31
4.6.3 Default device with ducting and radiator	32
4.7 MQB Radiator evaluation - production assembly.....	33
5 Boundary conditions.....	36
5.1 Air mass flow rate at inlet	36
5.1.1 Anemometer mounting	37
5.1.2 Measured data evaluation.....	38
5.2 Radiator parametrization	39
5.2.1 Specifying the boundary conditions.....	40
6 Simulation of the original state	43
6.1 3D model.....	43
6.1.1 Scanning.....	43
6.1.2 Raw 3D data processing.....	44
6.1.3 Final model	44
6.1.4 Model properties	45
6.2 Computational fluid dynamics	45

6.2.1	Meshing	46
6.2.2	Simulation parameters	48
6.2.3	Simulation convergence	49
6.3	Results Evaluation	49
6.3.1	Yplus.....	49
6.3.2	Data collection.....	50
6.3.3	Evaluation of the measurement	52
6.4	Simulation accuracy.....	53
7	Optimalization	56
7.1	Parametric model	56
7.1.1	Parametric single-side default model	57
7.1.2	Parametric symmetrical default model.....	60
7.2	Radiator parametrisation.....	61
7.2.1	Default state evaluation and confirmation of established coefficients.....	61
7.2.2	Incorporating the radiator into the parametric model.....	63
7.3	Characteristic model elements	65
7.3.1	Separation surface delete	65
7.3.2	Primary curvature	67
7.3.3	The channel width	68
7.3.4	The secondary curve.....	70
7.3.5	The separation edge	70
7.3.6	Profile length optimisation	71
7.3.7	Chapter conclusion	72
7.4	Proposing the optimised design	73
7.4.1	Distance to the radiator.....	73
7.4.2	The length of the profile	74
7.4.3	The separation curve and relative distance.....	75
7.4.4	Conclusion and the final design presentation.....	77
8	Operational characteristics.....	78
8.1	Usage of the optimised profile in a moving vehicle	78
8.1.1	Mass flow at speed	78
8.1.2	mass flow at speed with inlet mass flow	79
8.2	Pressure drop evaluation	79
9	Verification.....	81
9.1	Testing methodology	81
9.2	Default shape remanufactured measurement.....	82
9.3	Optimised shape measurement	84
9.4	Noise characteristics	87
10	Conclusion	89
	Sources.....	92
	List of abbreviations and symbols.....	95
	Attachments list	98

INTRODUCTION

In the current state of the automotive industry, the engineering effort is focused mainly on improving the efficiency of every aspect of the passenger vehicle. Powertrain and bodywork aerodynamics have changed dramatically in the past decades, reducing the overall resistance forces. However apart from the introduction of electric radiator fans in place of their viscous-coupled predecessors, the means of radiator heat-dissipation did hardly change.

This thesis aims at analysing the cooling needs of a modern vehicle and evaluating the possibility of a bladeless fan design deployment. Such bladeless fan designs usually use an aerodynamic phenomenon referred to as the Coanda effect. Technological company Dyson, best known as a manufacturer of small electric home-appliances sells multiple devices based on this principle. It's tabletop fan Dyson AM07 will be used as a baseline for examining this design approach.

This design will be further optimised based on the multiple findings not only to improve its efficiency, but also to meet the installation dimensions required for a use in a personal vehicle. The intention is not to develop a finalised product, but rather to inspect the limits of this cooling strategy and provide a deeper understanding of the principles applied in designing a bladeless cooling system.

The knowledge, acquired by this study will be used to design and manufacture a prototype device, which will be subjected to testing – not only confirming, or refuting the expected behaviour, but also evaluating its real-life operational characteristics. To provide a sufficient context for these tests, the results will be compared to a production cooler assembly.

Finally, the possible path of further development will be outlined along with identifying the deficiencies of this design.

1 COOLING NEEDS OF A MODERN VEHICLE

As of today, the shift of transportation from combustion engines to electric powertrain is evident. Since the emission standards are setting unreasonable limits for combustion engine emission levels, it is important to evaluate requirements of the alternative means of propulsion and their respective cooling system needs.

1.1 ROAD GOING VEHICLE POWER REQUIREMENT

To establish a baseline for the heat, that needs to be dissipated by a cooling system of a vehicle, it is important to review its resistance forces.

The vehicles resistance forces can be divided to two main categories:

- Rolling resistance
- Aerodynamic resistance

1.1.1 ROLLING RESISTANCE

The rolling resistance originates in the contact of a tire with a road.

The total rolling resistance for a road with no gradient can be described as:

$$F_{rr} = C_r \cdot F_g \quad (1)$$

Where:

F_{rr} – rolling resistance [N]

C_r – coefficient of rolling resistance [-]

F_g – normal (gravitational) force [N]

Let's consider both – combustion engine vehicle and a battery electric vehicle.

As a representative of the combustion engine vehicle, the 4th generation of Skoda Octavia was chosen, equipped with the 1.5 TSI 110kW gasoline engine. The weight of this vehicle is: $m_{comb} = 1342 \text{ kg}$ [1]

To represent the battery electric vehicle, a Tesla Model 3 with standard range was chosen. The weight of this vehicle is: $m_{BEV} = 1617 \text{ kg}$ [2]

The coefficient of resistance on an asphalt road is usually found in between of values 0,01 and 0,02 [3]. The coefficient is chosen as: $c_{aspha} = 0,015$

The final resistance is then:

$$F_{rrcomb} = 0,015 \cdot 1342 \cdot 9,81 = 197,5 \text{ N} \quad (2)$$

$$F_{rrBE} = 0,015 \cdot 1617 \cdot 9,81 = 237,9 \text{ N} \quad (3)$$

1.1.2 AERODYNAMIC RESISTANCE

The aerodynamic resistance can be described by the equation:

$$F_{ar} = c_d \cdot \frac{1}{2} \cdot \rho \cdot v^2 \cdot A \quad (4)$$

Where:

F_{ar} – aerodynamic resistance [N]

C_d – aerodynamic resistance coefficient [-]

ρ – domain density [kg/m^3] - A density of $1,185 \text{ kg}/\text{m}^3$ was chosen since it is defined as a baseline air density in Ansys software.

v – relative speed of object and domain [m/s]

A – frontal surface area [m^2]

The typical aerodynamic resistance coefficient is found in between values of 0,3 and 0,4 for personal vehicles. [3]

For the 4th generation of Skoda Octavia, it is 0,24 [4] and for the Tesla Model 3, it is 0,23 [5]. Since the typical coefficient was retrieved from a publication released in the year 2000, it can be noted that the shift in the vehicles aerodynamics is evident.

The frontal area of Skoda Octavia is $S_{\text{Octavia}} = 2,15 \text{ m}^2$ [6], the area was measured in Autodesk inventor from a picture, that included dimensions for scale. This approach might not be 100% accurate but should provide sufficient data for this thesis.

While the frontal area of Tesla model 3 is $S_{\text{Model3}} = 2,2 \text{ m}^2$. [7]

1.1.3 TOTAL RESISTANCE

To establish the total resistance, the driving scenario must be defined. For the purposes of this thesis, 3 most likely scenarios were chosen – driving at 50, 90 and 130 km/h since these speeds coincide with the official legal speed limits in the Czech Republic for town, out of town and highway driving respectively.

The *Table 1* represents individual resistances at given conditions:

Table 1. Vehicle resistances

	Rolling resistance [N]	Aerodynamic resistance at 50km/h [N]	Aerodynamic resistance at 90km/h [N]	Aerodynamic resistance at 130 km/h [N]
Skoda Octavia	197,5	58,98	191,08	398,68
Tesla Model 3	237,9	57,83	187,38	390,95

The *Table 2* represents total resistances at given conditions:

Table 2. Total vehicle resistance

	50 km/h [N]	90 km/h [N]	130 km/h [N]
Skoda Octavia	256,48	388,58	596,18
Tesla Model 3	295,73	425,28	628,85

The resistance in current form is calculated as a force, acting against the vehicle's movement. For the purposes of the evaluation however, the expression of these values as a power is much more helpful.

The power can be calculated as follows:

$$P = F \cdot \frac{s}{t} = F \cdot v \quad (5)$$

Where:

P – Power [W]

F – Force [N]

s – distance [m]

t – time [s]

v – relative speed of object and domain [m/s]

Table 3. Power to maintain speed

Power to maintain speed	50 km/h [kW]	90 km/h [kW]	130 km/h [kW]
Skoda Octavia	3,56	9,71	21,53
Tesla Model 3	4,11	10,63	22,71

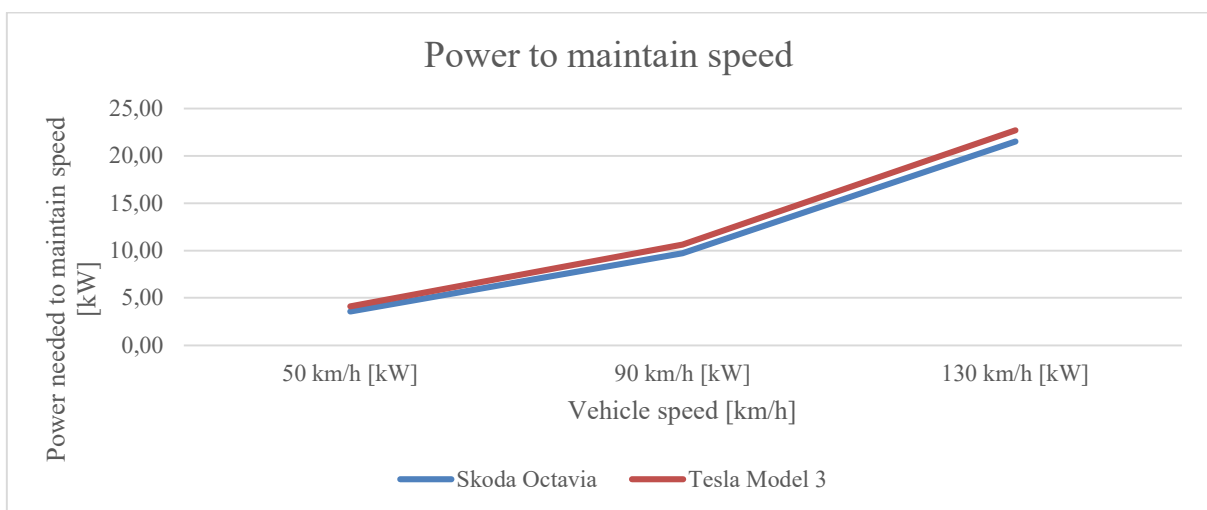


Figure 1. Power to maintain speed

Since the frontal area measurement of Skoda Octavia can contain some level of deviation, it can be stated that both vehicles driving resistances are very similar, if not identical.

To obtain single values, that will be further used for the purposes of this thesis, it was decided to combine these two vehicles and obtain their arithmetic mean.

Table 4. Average power to maintain speed

Power to maintain speed	50 km/h [kW]	90 km/h [kW]	130 km/h [kW]
Mean value	3,83	10,17	22,12

1.2 HEAT DISSIPATION

The standard cooling system of a personal vehicle consists of:

1. Radiator, 2. Coolant pump, 3. Fan, 4. Thermostat, 5. Cabin heater radiator, 6. Heater valve, 7. Engine coolant passages

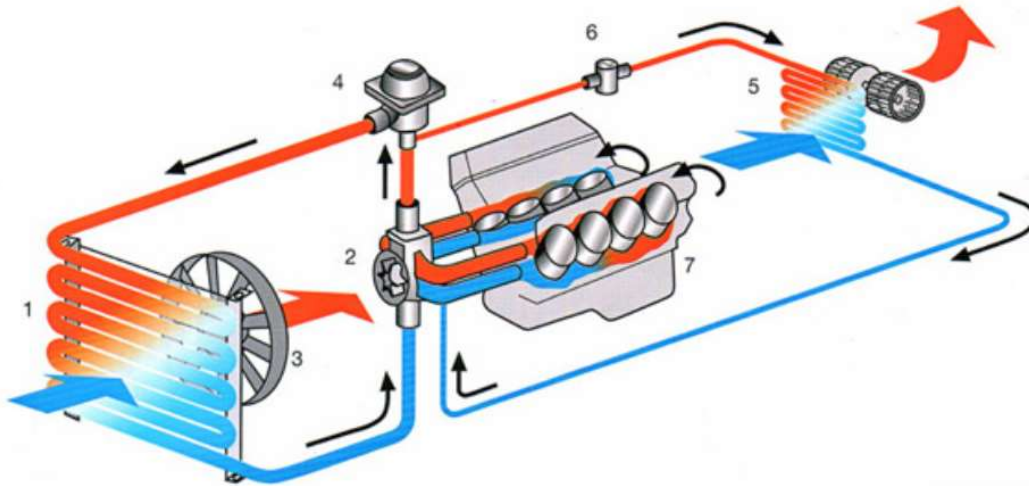


Figure 2. Cooling system of a combustion vehicle [8]

For the purposes of this thesis, it will be considered that the cabin heater radiator is disabled, since the vehicle needs to be able to dissipate the heat energy without compromising the cabin comfort.

A typical vehicle's cooling system is filled with a 1:1 mix of demineralized water and Ethylene Glycol to prevent freezing and corrosion. A typical boiling temperature of this mixture is 106 °C at atmospheric pressure. The cooling system is usually pressurised to 15 psi, which increases the boiling point to up to 130 °C.

However, the coolant is typically maintained at 90 to 100 °C. The thermostat, moderating the flow through radiator to control the temperature is usually fully open at a coolant temperature of 85 °C.

1.2.1 RADIATION

Heat transfer can happen through three different mechanisms: Conduction, convection, and radiation.

The radiation does certainly occur in the cooling system of a car but can be neglected when describing the radiator. In the given conditions, it plays only a minor role in contrast with the other means of heat transfer.

1.2.2 CONVECTION AND CONDUCTION

The radiator benefits from both principles to dissipate heat.

The radiator can be simplified as a metal tube, which has a hot coolant flowing inside, while being surrounded by cold, flowing air.

The heat enters the radiator (or the tube) and transfers its heat into the tube via convection.

Then, the heat is transferred from the inner wall of the tube to the outer wall of the tube via conduction.

Then, it is transferred via convection to the surrounding air, which flows over the tube.

The conduction is defined by the material, used to construct the radiator, which is usually an aluminium based alloy.

The convection is a heat transfer method, which defines the radiator and fan design.

Convection can be expressed as:

$$Q = \alpha_k \cdot A_{surf} \cdot \Delta t \quad (6)$$

Where:

Q – Heat energy [W]

α_k – Heat transfer coefficient [$W \cdot m^{-2} \cdot K^{-1}$]

A_{surf} – surface area [m^2]

Δt – temperature difference [K]

This equation sums up basically all the points of radiator design. To achieve the best possible heat transfer, it is beneficial to increase the surface area and temperature difference of the coolant and air as much as possible. The heat transfer coefficient is defined by the material, surface structure, level of contamination etc.

On the other hand, the density of the individual fins and passages needs to be set wisely to not pose too big of a back pressure on the air, trying to flow through the radiator.

1.3 COMBUSTION ENGINE EFFICIENCY

As a result of emission regulations, it can be said that today's level of combustion engine development had come close to the realistically obtainable efficiency. Even at this stage, the efficiency of combustion engine reaches at best 40%. This is however true to a large displacement industrial-grade engines, not typically used in a road-going vehicle. The efficiency of engines in said vehicles can usually range from 20 to 30%. [9]

The inefficiency can be further categorized to pumping, frictional and heat losses. As a matter of fact, all of these inefficiencies exit the engine as heat.

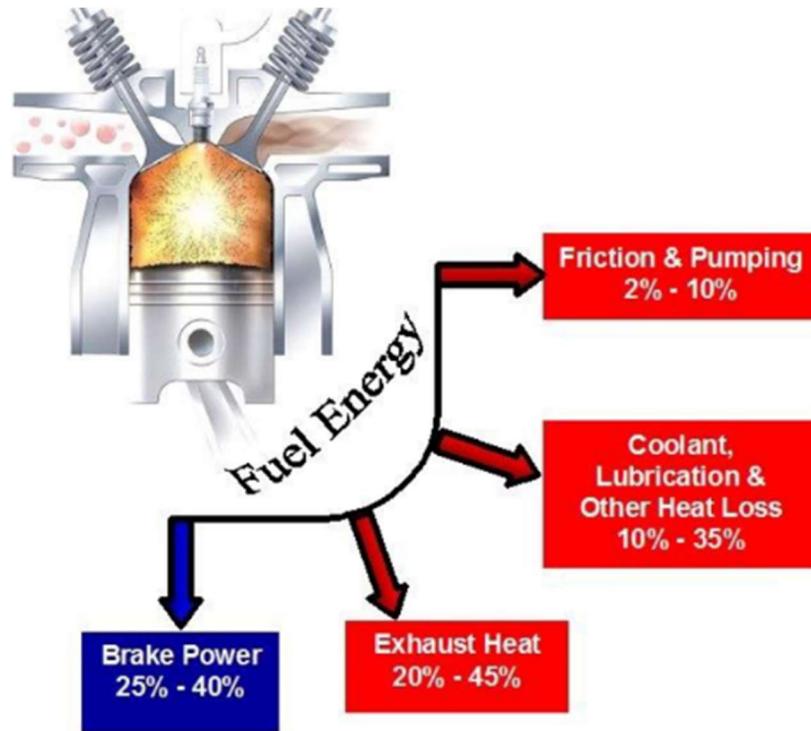


Figure 3. Combustion engine energy distribution [9]

It can be concluded that the energy distribution in a typical vehicle combustion engine is roughly as follows:

30% - brake power

30% - exhaust heat

40% - coolant

The Skoda Octavia, chosen as an example of such vehicle has a dispositive brake power of 110 kW. This would indicate that its cooling system must provide sufficient cooling capacity of 146 kW if maintained constantly at the highest power possible.

At idle, the car uses approximately 0,7 l of gasoline per hour. Accounting for its 32 MJ/l energy density and approximately 40% of it going into coolant heat, the heat load for the cooling system is 2kWh, while the coolant exiting the engine is at temperatures of 90-100 °C.

1.4 BATTERY ELECTRIC VEHICLE POWERTRAIN EFFICIENCY

The current battery technology poses a challenge in the cooling system design, because of a narrow operating temperature range. To demonstrate this, a model situation was proposed.

Tesla model 3 standard range battery as specified by the manufacturer offers 50kWh of capacity at a nominal voltage 350 V. It consists of 2976 cells, distributed into 96 groups, each comprised of 31 cells in a 21700 package. This designation indicates that the battery diameter is 21 mm and its length is 70 mm.

The characteristics of the cells, used in the vehicle are trade secret and are not readily available. It was chosen to obtain a datasheet for a battery of the same 21700 package from the same Lithium-Ion category.

A cell: *Li Ion 21700 5000mAh 18Wh* made by the company *AMS batteries* was chosen. [10]

The supplier specifies two critical parameters for battery efficiency – temperature and the discharge rate.

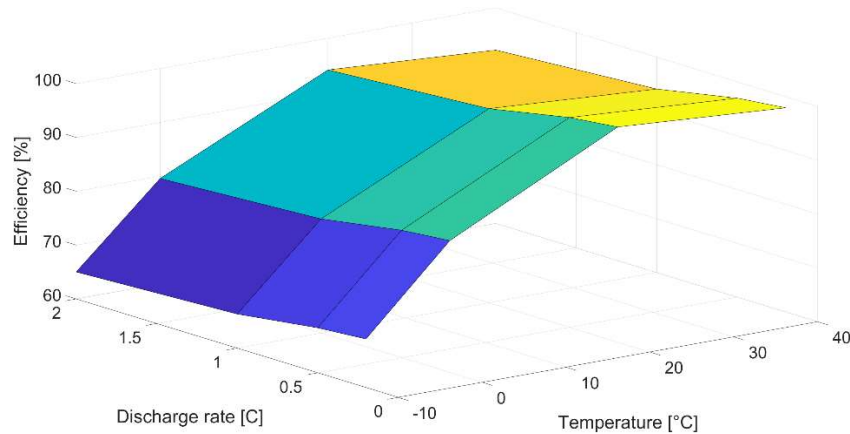


Figure 4. Battery efficiency characteristics [10]

As it can be observed in the graph, the peak efficiency is found at 20 °C and a low discharge rate. However, if the battery is kept at the sufficient temperature, the efficiency is held above 90 %, while possibly reaching 99% at a specific operating point.

For a speed of 130 km/h and a power draw of 22,12 kWh, the battery is being discharged at 0,44 C.

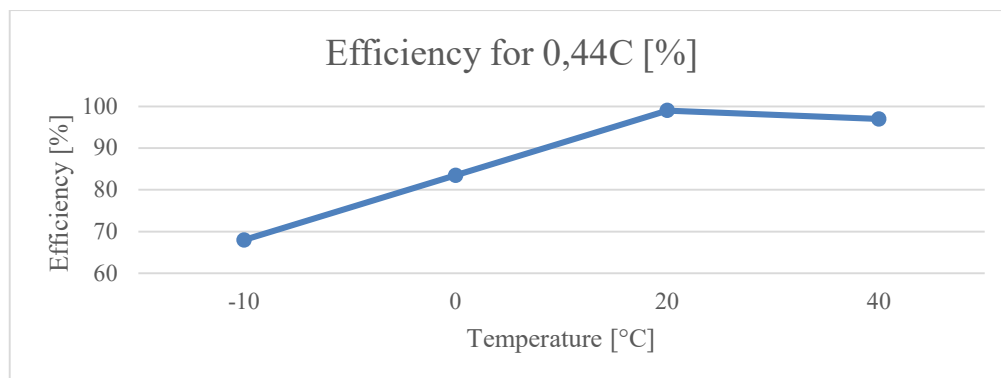


Figure 5. Battery efficiency for constant C [10]

As it is evident, the efficiency of the battery is dependent on its temperature. The manufacturer specifies that the maximum operating temperature of the cell is 60 °C at discharge and 45 °C at charging scenario.

Considering the driving at 130 km/h at a temperature of 20 °C, the battery produces 0,684 kWh of waste heat, which is manageable even in this low temperature delta scenario. This value was obtained by calculating the heat output of the battery given its internal electric resistance. The problem arises while charging.

The peak charging power can reach 250 kWh. [11] At this time, the vehicle is not moving, meaning that 100% of its cooling is reliant on forced air circulation. Considering even 97% efficiency, the waste heat is equal to 8 kWh, which is 4 times the amount of a combustion engine at standstill and idling. Furthermore, the temperature difference between the ambient air and the desired temperature might be only a couple of degrees Celsius.

Multiple approaches can be used to solve this problem. The charging rate can be limited, which is inconvenient for the vehicle's user. The airflow through the radiator might be increased, or the heat exchange surface can be increased – probably by adding radiators to wheel arches, or other so far unused spaces. The ultimate solution is to use a heat pump, that helps to generate a higher temperature difference. It is however a costly and technically complex solution.

The findings of this thesis can be beneficial to improving the radiator heat exchange efficiency and allowing the radiator installation to atypical areas of the vehicle.

2 CURRENT COOLER DESIGN

As of today, most vehicles use a heat exchanger with a traditional axial fan. As a base test subject, a production assembly of said heat exchanger was chosen. This assembly can be found in several vehicles based on VW AG platform MQB with part number 5WA.121.205.E. For the purposes of this thesis, the radiator from this assembly will be referred to as the “MQB radiator”.



Figure 6. MQB platform cooling assembly

The assembly is placed in the front of the vehicle’s engine bay with the fan facing backwards into the engine compartment. This positioning is beneficial from the standpoint of “passive” cooling – when the vehicle is moving, the movement of the vehicle forces air through the radiator. In this scenario however a problem arises, where the fan and its shroud acts as a restriction, adding backpressure to the already restrictive radiator. The effect of the shroud restriction is partially mitigated by flaps, which open in higher speeds, decreasing the restrictiveness of the shroud. The blades of the fan, the motor hub and the plastic shroud however stay to create a pressure loss environment.

This design however carries more things to consider.

Shape of the fan (circle) does not usually match the shape of the radiator (rectangle) This leads to a coverage inefficiency, resulting in areas not directly covered by the fan. If an oblong radiator must be covered by a fan, this inefficiency increases. The coefficient of oblongness is expressed as the ratio of the radiators side lengths.

When the oblongness of the radiator increases, the surface coverage drops down significantly. However, for coefficient of oblongness higher than 2, multiple fans can be installed onto the radiator, improving the situation. This complicates the design and adds points of failure.

The measurement methodises and results of MQB platform cooler assembly will be further described in the *Chapter 4.7* of this thesis.

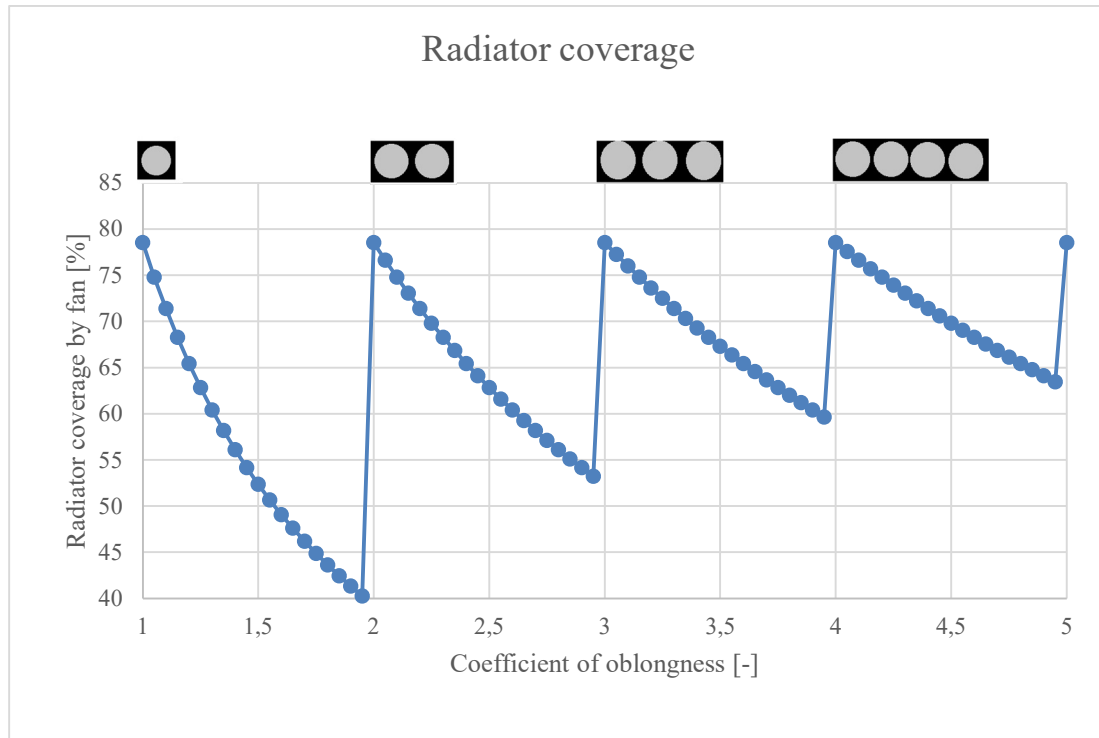


Figure 7. Radiator coverage
The depictions on top represent a radiator (black) and a fan (grey)

3 COANDA EFFECT

3.1 HISTORICAL REFERENCES

The Coanda effect was patented in 1936 by Henri Coanda, interestingly however, interaction between solid body and fluid domain, proves to have caused scientific disagreements even before then.

3.1.1 MAGNUS EFFECT

In 1742, Benjamin Robins had observed, that a ballistic projectile tends to follow a curved trajectory, caused most likely by its spin. [12] This theorem was disagreed by Leonhard Euler, who claimed the trajectory is caused by surface irregularities of said projectile. This effect was rediscovered in 1835 by Gustav Magnus, who gave it its name – Magnus Effect.

3.1.2 COANDA EFFECT

Thomas Young in the year 1800 noticed that the dimple in a water surface, caused by a narrow stream of air, directed perpendicularly to the surface, is bound to change its location with regards to a curved body, placed into its proximity. [13]

In another words, he describes that a narrow jet of air is influenced by a near, curved body, resulting in a force, acting on the jet of air as well as on the body itself - Preserving the third Newton's law.

The effect got the name after Henri Coanda, who actively used it in designs of aircrafts around 1910. Patenting the effect explicitly in 1936.

Mr. Coanda used this effect in his aircraft design, where he noticed that a motor-driven turbine created a hot airflow, which tend to attract to nearby aircraft surfaces.

The Coanda's findings not only describe this fluid-solid behaviour, but extend this principle to real world situations, where interaction between two fluids and a solid take place – i.e. in atmospheric conditions. Here, the effect can be used to influence stationary, or moving fluid domain by another jet of moving fluid, or a shape of solid body.

3.1.3 DISTINCTION

Be aware that Coanda and Magnus effects are two separate phenomena. The use of Coanda effect in an aircraft design might cause a confusion, which this paragraph aims to eliminate.

Magnus effect describes the creation of a lift, caused by a divergence of airflow by a body in the flow's path, where the fluid domain is in an extended flow – meaning the dimensions of said fluid domain are superior to those of the solid body considered. [14]

Coanda effect describes that flowing fluid sticks to curved surface and continues to follow the shape of said surface unless its curvature deviates significantly – for example sharp edge. In this case, dimensions of fluid domain and solid body are in the same order of magnitude. i.e., similarly sized.

3.2 TEST SUBJECT

Measuring a device, already using a Coanda effect seemed to be a good way to establish a measurement baseline. For these purposes a Dyson AM07 was obtained.

The Dyson AM07 model was chosen for several positive properties:

- The size of the device is big enough to allow for local measurements. This allows for investigation of locally occurring effects, distribution of the airflow etc. If the device was of a smaller size, these effects could blend in and might not be detectable by available measuring methods, described in the next chapter.
- The device is also not too large, which is beneficial for its 3D scanning, modelling, and simulating in Computational Fluid Dynamics simulations.
- The construction of the device is simple, consisting of just a cross section, swept along a simple curve. This too allows for easy replication in 3D models.

The main drawbacks of this model are:

- It is not designed to deal with back pressure. This is a strong deficiency, since this thesis is aimed at application of Coanda effect on vehicle cooling, which inherently requires combination of this fan module with a radiator, providing a level of back pressure.
- The original intended use is a simple table-fan. The cross-sectional shape of the fan is than optimised for circulation of air in enclosed spaces. This leads to a completely different optimisation targets than that of this thesis.
- The airflow achieved is quite limited to satisfy consumer needs such as a quiet operation.



Figure 8. Dyson AM07 [15, 16]

As the *Figure 8* illustrates, the air is pumped into the hollow profile via a compressor, located in the cylindrical base. As the air escapes the profile through a thin opening, it sticks to the walls due to the Coanda effect. As the air is travelling along the wall, additional air is being dragged along with it, resulting in an area of low pressure. This sucks even more air through the intake side of the fan. This effect is referred to by the manufacturer as an Air Multiplier™.

With usage of Ansys default material library, for Air at room temperature of 25 °C and an absolute pressure of $p = 1$ bar a density of $\rho = 1,185\text{kg/m}^3$ will be used as a baseline.

To calculate the mass airflow from the volumetric airflow, the following equation is used:

$$\dot{m} = \dot{V} \cdot \rho \quad (7)$$

Where:

\dot{m} – mass air flow [kg/s]

\dot{V} – volumetric air flow [m^3/s]

ρ – domain density [kg/s]

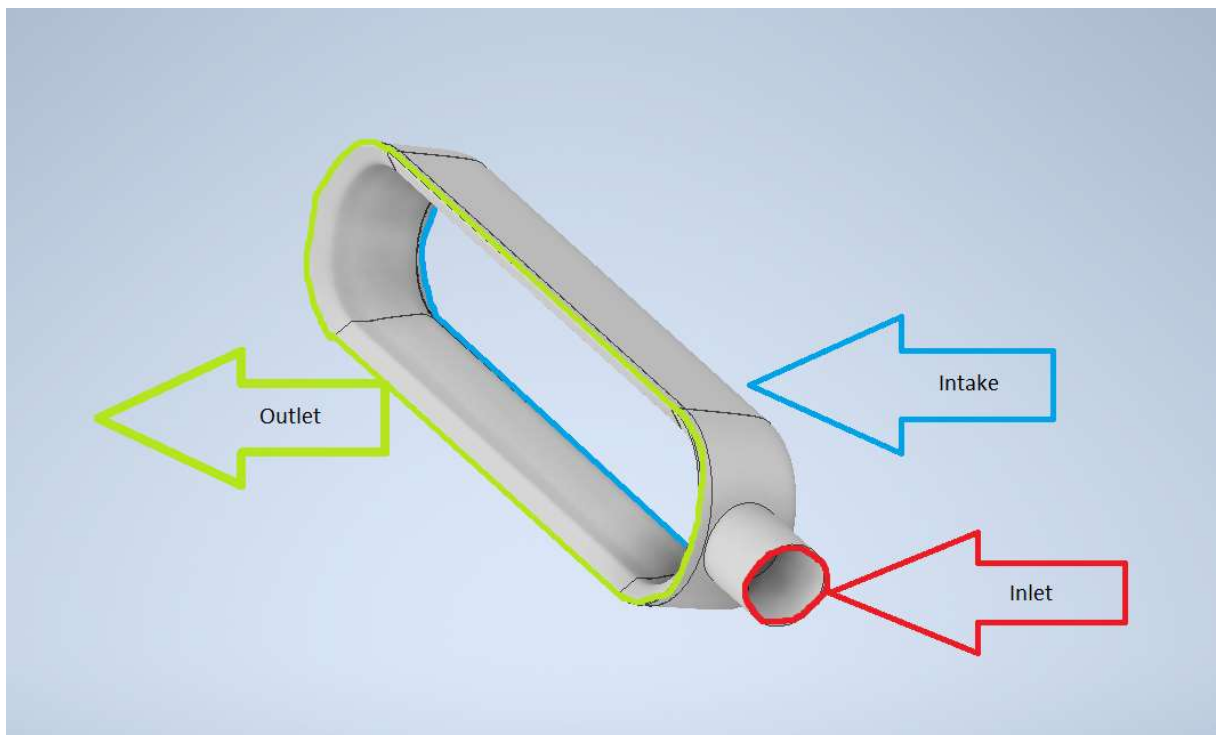


Figure 9. Labelling the areas of air exchange

For further clarification of the airflow, there are 3 air flow regions labelled in the *Figure 9*.

Inlet – air is pushed into the profile thanks to a compressor.

Intake – air is pulled in due to low pressure area caused by the Coanda effect.

Outlet – air escapes from the device. Its mass airflow is equal to the sum of mass airflows from intake and inlet.

4 EXPERIMENT

The objective of conducted measurements is to establish a set of boundary conditions to be applied in CFD (Computational Fluid Dynamics) modelling and further design optimisation.

4.1 MEASUREMENT METHODOISES

Tests are performed in a closed room of a size significantly greater, than the distance affected by airflow, coming from the measured object.

The primary measured parameter is air-flow speed in a discrete region of the object.

Datapoints are arranged into a recurring perpendicular mesh, as *Figure 10* shows:

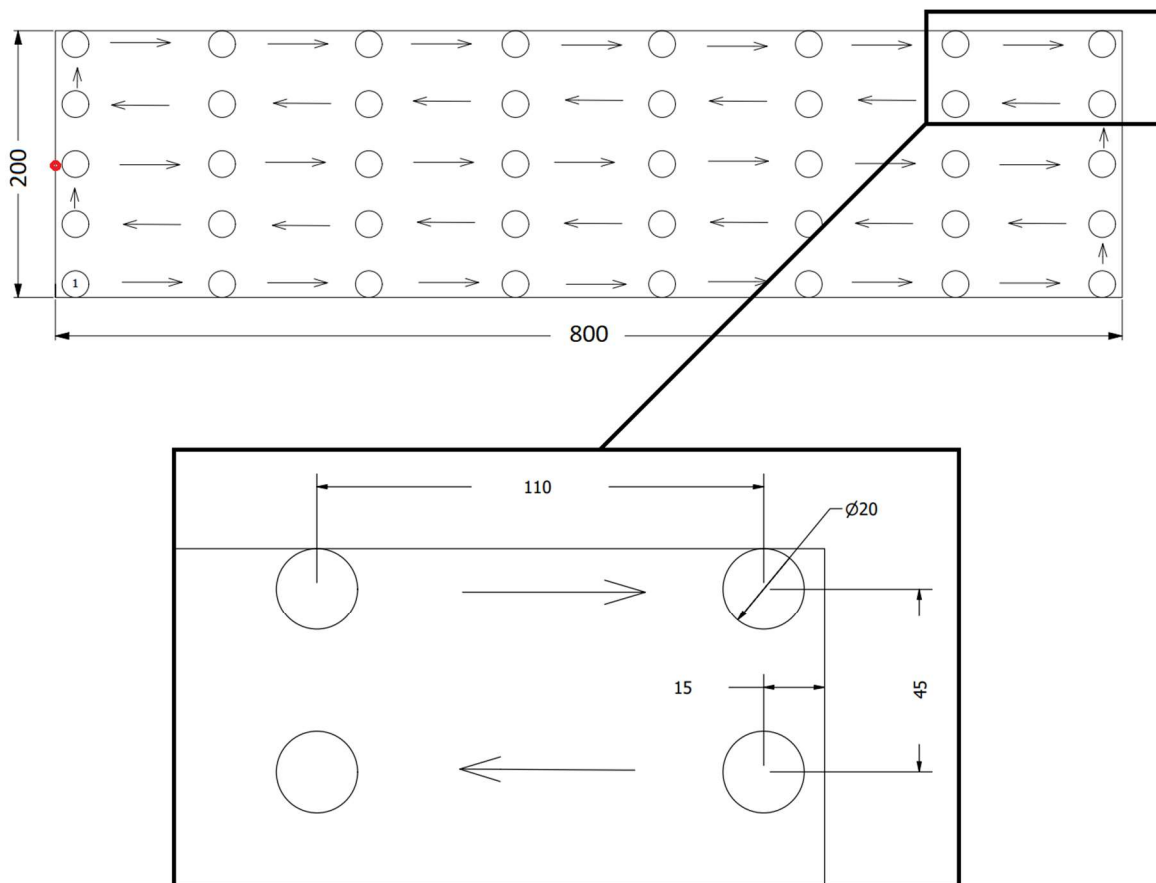


Figure 10. Measurement methodises

The imaginary mesh was aligned with measured object, ensuring the mesh and the object are parallel to each other. Midpoint of left vertical axes (represented by a red dot) was aligned with midpoint of measured object's left vertical edge. First measurement is read from the bottom left datapoint, labelled "1". The following measurements are taken consecutively, following the arrows to form an s-shaped pattern. This methodology was chosen primarily for the ease of measurement itself, targeting minimal changes to the measuring probe fixing between measurements.

4.2 POSITIONING SYSTEM

To ensure a repeatability of experiments a system of holders and rails was constructed to position the anemometer into measuring points specified above. This also ensures that the Anemometers axis stays parallel to the airflow streamlines and maintains a constant distance from the measured object. This is a crucial condition for conducting an accurate measurement.

The mechanics of this positioning system is inspired by industry standard used in 3D printers. A multiple of LM8UU linear ball bearings is press-fitted into 3D printed parts, sliding on two guiding pairs of 8mm steel rods.

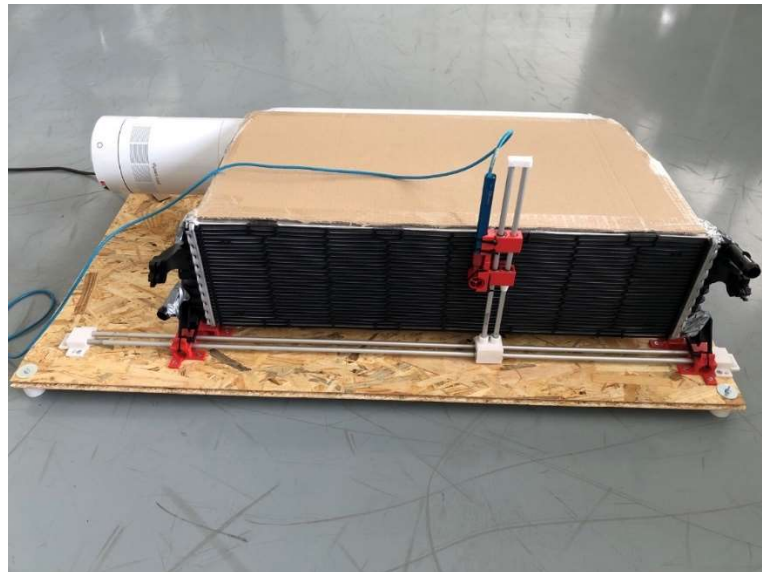


Figure 11. Measurement assembly

The positioning of the probe-housing is secured by two friction contacts. The horizontal axis remains stable just from a static friction between the two ball bearings and rods. Vertical axis is secured by a flexible 3D printed white cone.

The anemometer is tied down with zip-ties to the measuring probe housing body. It is of utmost importance to maintain a constant distance of anemometer probe to the measured body as well as the anemometers axis to be perpendicular with the measured object. Every conducted experiment ensures that the distance of a probe is within a tolerance of 0 to 3 mm from the measured body.

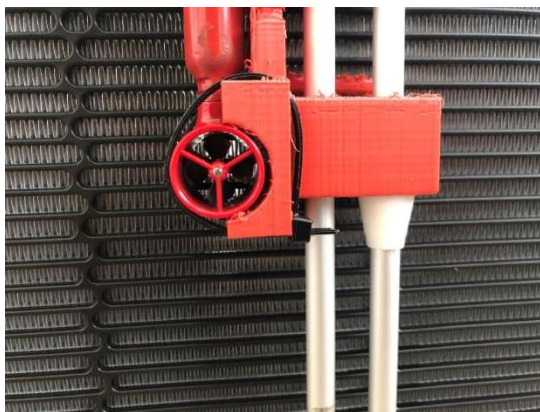


Figure 12. Detailed view of measurement probe – anemometer housing

4.3 DATA COLLECTION

Air-flow speed is measured by an anemometer Almemo zähler FV A915-S120 with measuring range of 0-20 m/s. Its inner diameter is 18mm which will be used in the upcoming chapters during simulation analysis.

Data is collected on to a datalogger Almemo 2890-9.

Data is collected by the following operations:

- Dyson bladeless fan is turned on, with the highest power setting available.
- Anemometer probe is moved to 1st datapoint, labelled 1 in the *Figure 10*.
- After said movement, at least 10 seconds is allowed for the anemometer propeller to reach the speed of the airflow.
- During these 10 seconds, it is visually confirmed that the airflow is of expected direction, checking the anemometer's blade direction of rotation and confirming this with a deformation of a piece of fine paper, glued to the probe.
- Data-logging is started on Almemo datalogger, which takes 10 seconds.
- During these 10 seconds, 100 values are stored, and arithmetic mean calculated right on the datalogger itself.
- The resulting value is entered manually into a table of results.
- Measured device remains turned on, while the anemometer probe is moved to the next measuring point.
- The process repeats, until all data points are collected for given experiment.

4.4 DATA REPRESENTATION

- O/R – out of range, the measuring probe was located outside of the measured body, while also returning values of less than 0,5 m/s. In case the probe was located outside of the measured body and despite that was returning stable values, they were recorded.
- T0 – the probe was returning unstable values. In locations marked with this symbol, turbulent airflow was very likely occurring, since the air speed and direction of flow was changing rapidly.
- The red scale represents the significancy of individual values, aimed at better visualisation. The darker the shade, the higher the air speed.
- The blue scale represents areas, where airflow was flowing in the opposite direction than expected. Similarly, the darker the shade, the higher the air speed in this direction.

4.5 CALIBRATION

Anemometers tend to provide distorted results due to their high sensitivity. If for example a blade on the sensing propeller was bent, it might impose higher than accounted for back pressure, leading to a divergence from expected rotational speed and thus inaccurate calculated air speed. In all the performed measurements, the maximum deviation from the optimal position was limited to an angle of 1° in all axes to ensure comparability of measured data.

To ensure that the obtained results can be trusted, the anemometer and datalogger were sent to calibration facility of Czech Metrological Institute. The scan of the original calibration protocol Nr. 6015-KL-P0911-22 is provided in the *Attachment 1*.

As it can be seen in the protocol, the anemometer proved to be a reliable measurement device with deviation ranging from 0,016 to 0,1 m/s depending on the speed.

The highest measured speed during the measurements in the next chapter was 8,71 m/s so it can be concluded that the anemometer operates within its range. On this basis, it was calculated, that the absolute measurement error in the speed range from 0 to 10 m/s averages under 2% which can be considered negligible in the scope of this thesis.

4.6 CONDUCTED EXPERIMENTS

The mass flow of air can be calculated as:

$$\dot{m} = v \cdot S \cdot \rho \quad (8)$$

Where:

\dot{m} – mass air flow [kg/s]

v – relative speed of object and domain [m/s]

S - the cross-sectional area of anemometer probe, alternatively when investigating the volumetric flow throughout the whole body, the area of datapoint zone

ρ – the density of the domain [kg/m³]

For the purposes of this thesis, the air density is considered to be a constant $\rho = 1,185 \text{ kg/m}^3$. Multiple sources provide numerous values for air's density, which is understandable, since it is a compressible gas with variable composition – the main factors, having impact on density being humidity level, pressure and temperature.

Since the simulations are to be performed in Ansys CFX software, it was decided to use the Ansys library default Air density for a room temperature at 25 °C as a constant for this thesis.

To calculate the mass air flow, cross sectional area of the intake and outlet must be established. For high level of precision, 3D model was used, further described in the *Chapter 6*.

Experiment parameters were chosen to cover a wide range of conditions, to help with understanding the effects influencing the airflow.

It was also decided as stated in the *Chapter 4.5*, that given the high accuracy of the anemometer, measured data will not be corrected in any way. Speed values in the upcoming tables are representing the direct measured air speed, recorded from Almemo datalogger.

As described before in the *Chapter 3.2*, the measured device has 3 areas of air exchange:

- Inlet – Air is provided by a compressor in the base.
- Intake – Air is sucked in due to low pressure zone, created by Coanda effect.
- Outlet – Air is forced out.

The surface area was measured to be:

$$\text{Intake} = 83\,456,606 \text{ mm}^2 = 0,083457 \text{ m}^2$$

$$\text{Outlet} = 128\,542,139 \text{ mm}^2 = 0,128542 \text{ m}^2$$

4.6.1 DEFAULT DEVICE WITH NO ADDITIONAL ACCESSORIES

INTAKE DATA

Table 5. Air speed default device no accessories intake [m/s]

Inlet	0,7	1,13	1,45	1,43	1,45	1,62	1,37	O/R
	1,26	2,19	2,34	2,54	2,63	2,63	2,63	1,28
	1,03	1,34	1,82	2,04	2,19	2,15	1,92	0,99
	0,98	1,33	1,52	1,64	1,87	1,91	1,92	1,03
	0,84	1,11	1,32	1,51	1,65	1,66	1,77	1,15

$$V_{in1a} = 1,6241 \text{ m/s}$$

$$\dot{m}_{in1} = 0,1606 \text{ kg/s}$$

OUTLET DATA

Table 6. Air speed default device no accessories outlet [m/s]

Inlet	O/R	4,88	5,4	6,67	6,67	6,58	4,21	O/R
	1,01	1,26	1,41	1,55	1,71	1,07	2,83	1,72
	0,31	1,01	1,28	1,27	1,2	1,02	0,86	2,46
	0,33	0,59	1,19	1,13	1	0,89	1,13	1,98
	O/R	5,08	5,55	6,38	7,03	8,71	8,23	O/R

$$V_{out1a} = 2,9333 \text{ m/s}$$

$$\dot{m}_{out1} = 0,4468 \text{ kg/s}$$

In this experiment, it was observed, that the airflow seems to follow a cone-shaped pattern upon exiting the fans circumference. This is very likely due to the original purpose of the measured device, where this behaviour would be beneficial for its intended use as a room fan.

4.6.2 DEFAULT DEVICE WITH DUCTING

A cardboard ducting was constructed to mitigate the uneven air speed distribution from the previous experiment with hopes of homogenising the flow. This change might result in a better precision of measured values, since it gets rid of extreme changes, which might impose an inaccuracy problem.

The ducting can be seen in the *Figure 11* in the *Chapter 4.2*. In this test however, it is measured without the radiator installed.

In the final deployment, this effect shall be mitigated by a change of the profile itself.

INTAKE DATA

Table 7. Air speed default device ducting intake [m/s]

Inlet	O/R	0,87	1,09	1,29	1,44	1,52	1,44	0,84	
		0,56	1,19	1,62	1,92	1,94	2,08	2,13	2,05
		0,78	1,06	1,35	1,6	1,81	1,87	1,93	1,89
		0,71	1,21	1,59	1,69	1,89	1,9	2,02	1,96
		0,5	1,03	1,2	1,5	1,67	1,65	1,87	1,42

$$V_{in2av} = 1,4892 \text{ m/s}$$

$$\dot{m}_{in2} = 0,1473 \text{ kg/s}$$

OUTLET DATA

Table 8. Air speed default device ducting outlet [m/s]

Inlet		0,86	0,58	3,68	4,97	5,32	4,99	4,75	2,84
		0,99	0,53	1,81	3,4	3,27	2,93	3,03	2,46
		0,8	0,56	1,51	1,98	1,71	1,51	1,54	2,3
		0,73	0,54	0,9	2,05	2,2	2,8	2,05	2,45
		0,57	0,34	2,62	3,98	4,06	4,94	4,55	3,6

$$V_{out2a} = 2,4175 \text{ m/s}$$

$$\dot{m}_{out2} = 0,3682 \text{ kg/s}$$

As it can be observed, the total mass flow rate is reduced by 21% compared to the measurement with no accessories, however the air speed distribution is more homogenous, which is a desired effect.

4.6.3 DEFAULT DEVICE WITH DUCTING AND RADIATOR

For the final measurement, a narrow radiator further described in the *Chapter 5.2* was installed on the end of the ducting to simulate a usage of bladeless fan in a passenger vehicle. This also provides data for bladeless fan behaviour while operating with high back pressure.

INTAKE DATA

Table 9. Air speed default device radiator intake [m/s]

O/R	-0,45	TO	TO	TO	0,54	0,7	O/R
-0,3	-0,73	TO	TO	TO	0,85	1,07	0,97
TO	-1,16	TO	TO	TO	0,9	1,06	1,07
-0,25	-1,14	TO	TO	TO	0,9	1,1	0,97
O/R	-0,8	TO	TO	TO	0,7	0,78	O/R

$$V_{in3ave} = 0,339 \text{ m/s}$$

$$\dot{m}_{in3} = 0,0335 \text{ kg/s}$$

OUTLET DATA

Table 10. Air speed default device radiator outlet [m/s]

0,76	0,77	1,78	1,65	1,49	1,55	1,31	1,15
0,73	0,59	1,3	1,49	1,49	1,41	1,13	1,06
0,73	0,53	1,14	1,28	1,33	1,27	1,19	1,1
0,75	0,48	1,31	1,27	1,28	1,3	1,27	1,3
0,74	0,6	1,77	1,44	1,51	1,56	1,52	1,35

$$V_{out3ave} = 1,192 \text{ m/s}$$

$$\dot{m}_{out3} = 0,1816 \text{ kg/s}$$

As it can be observed in the intake data, the radiator caused a great disturbance in the air flow. It was observed in all measurements, that the lowest air speed can be found in the vicinity of the inlet to the profile. It might be caused by a sub-optimal design of the internal part, leading to a poor air distribution. However further investigation was deemed unimportant at this stage.

It must be noted that the back pressure of the radiator had a negative impact on the behaviour of the device. The air, coming from the compressor is being deflected back by the radiator and exhausted through the left part of the intake, bypassing the radiator. It can be concluded that the benefits of Coanda effect are basically negated by the radiator's disturbance.

Table 11. Conclusion of real-world measurements

	Average intake velocity [m/s]	Mass air flow intake [kg/s]	average outlet velocity [m/s]	Mass flow outlet [kg/s]	Intake ratio [%]
No accessories	1,6241	0,1606	2,9333	0,4468	35,94
Ducting only	1,4892	0,1473	2,4175	0,3682	40,01
Ducting and radiator	0,339	0,0335	1,192	0,1816	18,45

4.7 MQB RADIATOR EVALUATION - PRODUCTION ASSEMBLY

To evaluate the cooler assembly performance, a similar approach was chosen. Thanks to its design however, there was no need to construct a positioning system. A pattern of measuring points was drawn onto the surface of the radiator. These points were manually measured one by one with the anemometer, directly touching the radiator surface. They can be seen on the right side in the *Figure 6* in the *Chapter 2*.

Multiple measurements were performed to be able to track the correlation of power draw of the fan and airflow. Here, the distribution of air speed for maximum power is depicted in the *Table 12*. The distributions for low and medium power can be found in the *Attachments 2* and *3* respectively.

Table 12. MQB assembly air speed distribution maximum power

		<u>Position X [mm]</u>													
		2,5	5	10	15	20	25	30	35	40	45	50	55	60	62
Position Y [mm]	44	0,87	0,95	1,32	1,98	2,87	4,11	5,27	6,03	6,28	5,61	4,25	2,96	2,27	2,22
	40	0,9	1,03	1,51	2,32	3,53	5,12	6,1	6,45	6,5	6,12	5,21	3,57	2,52	2,38
	35	1,01	1,09	1,91	2,94	4,8	5,88	6,24	6,33	6,26	6,18	5,93	4,71	3,16	3,01
	30	1,05	1,2	2,12	3,77	5,68	6,07	5,98	5,17	5,18	5,89	6,05	5,62	3,73	3,46
	25	1,16	1,36	2,35	4,21	5,81	5,91	5,13	3,39	3,52	5,34	6	5,94	3,97	3,59
	20	1,15	1,35	2,21	4,03	5,75	6,01	5,28	3,65	3,91	5,41	6,12	5,84	3,99	3,31
	15	0,91	1,18	2,07	3,54	5,46	6,18	5,99	5,82	5,88	6,11	6,08	5,29	3,43	3
	10	0,7	0,89	1,75	2,7	4,42	6	6,33	6,47	6,45	6,38	5,92	4,13	2,86	2,7
	5	0,77	0,81	1,29	2,1	3,26	4,73	6,11	6,58	6,48	5,74	4,46	2,93	1,99	1,9
	2,5	0,63	0,75	1,27	1,98	3,03	3,76	4,61	5,45	5,01	4,46	3,68	2,43	1,82	1,66

CHARACTERISTICS

Table 13. MQB assembly operational characteristics

Level	Power [W]	Average velocity [m/s]	Mass air flow [kg/s]
Low	8,1	0,77	0,268176741
Medium	216,46	2,97	1,03612608
Maximum	444,8	3,89	1,35730523

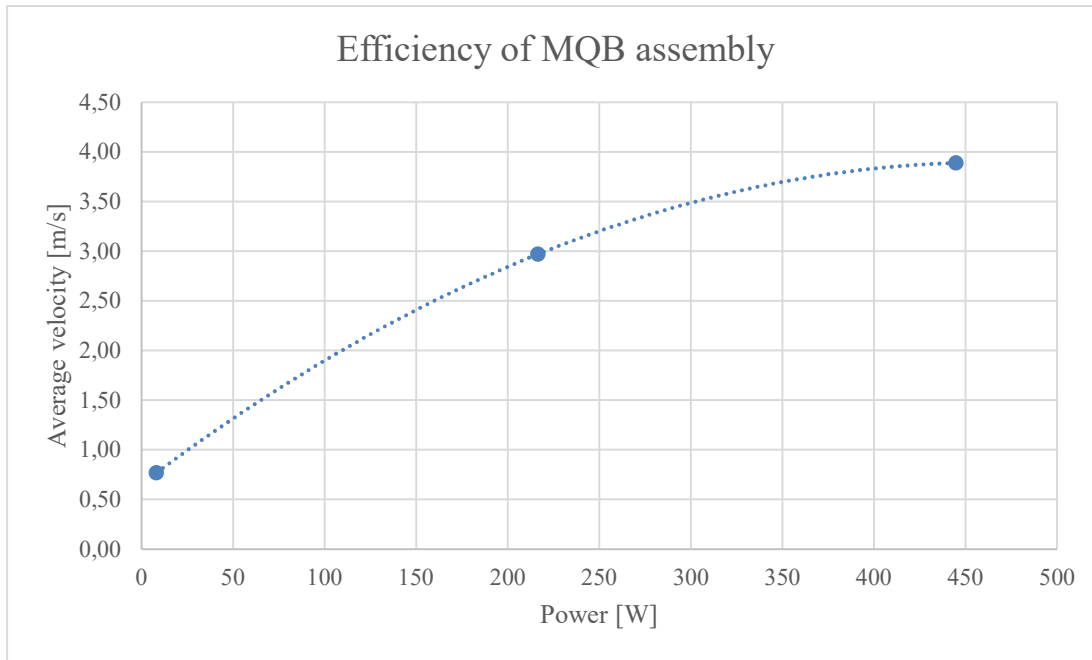


Figure 13. Efficiency of MQB assembly

As it is expected, the power requirements rise non-linearly with the demand for higher average velocity.

It also must be noted, that as visible in the *Table 12*, the distribution of the air speed is inhomogeneous, which is further represented by this histogram:

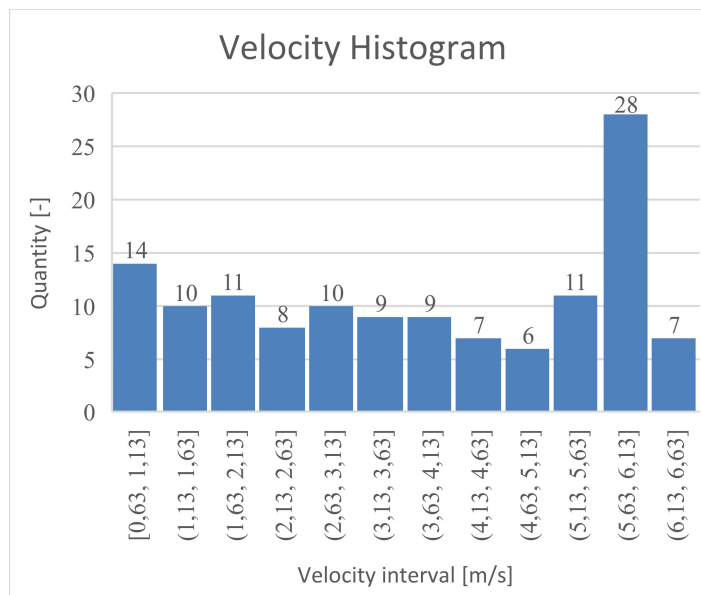


Figure 14. MQB assembly, velocity histogram for maximum power

A very simplistic Newton's resistance formula:

$$F = \frac{1}{2} \cdot C \cdot \rho \cdot S \cdot v^2 \quad (9)$$

Where:

F – Force, acting against an object, moving through a domain [N]

C – Friction coefficient [-]

ρ – Domain density [kg/m³]

S – Surface area normal to the direction of movement [m²]

v – velocity in the direction of movement [m/s]

Can point out that the resistance grows quadratically with the increase of velocity.

Applying this knowledge, for the least resistance, it would be optimal to have a homogenous distribution of the velocity across the whole radiator surface, which would achieve the lowest possible local resistance values for a given air flow request.

Since the left side of the radiator along with all corners is receiving visibly less airflow, it is believed that the overall distribution can be improved with the new design, decreasing the resistance of the radiator.

5 BOUNDARY CONDITIONS

This chapter's purpose is to analyse measured data and establish a set of boundary conditions that shall be used for simulation.

5.1 AIR MASS FLOW RATE AT INLET

For the purpose of Ansys CFX simulation it was determined that mass flow rate and radiator resistance have to be parametrised.

The test subject as described in the *Chapter 3.2* was separated into two parts – the hollow profile and the base with a turbine. Only the base was used for this measurement, neglecting the pressure loss of the upper part.

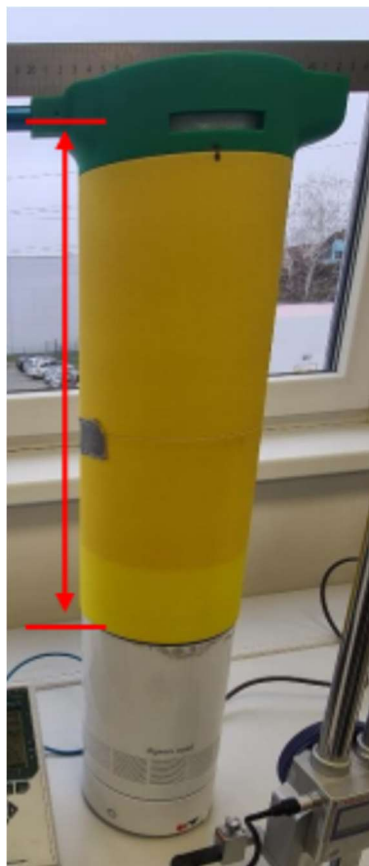


Figure 15. Turbine measurement assembly

It was decided to use the same measuring devices as in *Chapter 4.3*. An extension with the option to variate the distance between anemometer and test subject was designed. The distance between the anemometer and base – dimension marked by a red line in the *Figure 15* can be varied to achieve distances of 215, 395 and 595 mm.

5.1.1 ANEMOMETER MOUNTING

Since the positioning of the anemometer is critical for a reliable measurement, a mounting system was designed. It consists of a holder and 3 stackable parts to vary the distance.



Figure 16. Anemometer mounting

The mounting allows for translational movement of the anemometer. To capture the air mass flow rate accurately, along with testing in three heights, the whole module will be rotated by 0, 45 and 90° along its vertical axis.

As pointed out in the *Figure 16*, the vertical difference between two red points was measured, to ensure, the axis of anemometers propeller is parallel to the air flow. This measurement was done only once since its purpose was to ensure the correct orientation for the hole through which the anemometer is mounted. The average angle, achieved from these measurements was calculated to be 0.46 ° providing satisfactory accuracy.

Table 14. Anemometer mount alignment

Measurement	X1 [mm]	X2 [mm]	Difference [mm]	Length [mm]	Angle (Rad)	Angle (Deg)
1	0	-1	-1	117	-0,0085	-0,49
2	0,93	0	-0,93	117	-0,0079	-0,46
3	0	-0,93	-0,93	117	-0,0079	-0,46
4	0,88	0	-0,88	117	-0,0075	-0,43
Average						-0,46



Figure 17. Anemometer second axis alignment

To ensure that the approach angle of the anemometer probe is optimal, it had to be aligned in the second axis. This was achieved through measuring the position deviation of two points depicted in the *Figure 17* on the second axis of the anemometer. The maximum vertical difference allowed for this measurement was set to not exceed 0.37 mm which accounts for a deviation of 1 °.

5.1.2 MEASURED DATA EVALUATION

The raw data and its analysis are included in the *Attachments 4, 5, 6, 7 and 8*.

It was observed that the distribution of air velocity is not homogenous and is dependent on the position relative to the centre of the fan as well as on the angle at which the measurement assembly is rotated along the vertical axis. It is considered to be intentional, since the turbine is not placed concentrically within the housing. It was determined to neglect this behaviour, since it most likely serves to provide optimal approach angle of the flow to the upper part of the test subject.

EVALUATION

Table 15. Base mass flow measurement evaluation

Height of the measurement [mm]	Average velocity [m/s]	Median velocity [m/s]	Average deviation angle [°]
595	4,27	4,42	0,54
395	4,18	4,24	0,65
215	6,03	6,64	0,48

It was decided to use the measurement at the height of 595 mm since it is most likely to provide accurate results. As stated before, the Anemometer is highly sensitive on the approach angle of the measured fluid. Using the highest possible height should achieve the best laminarity of the airflow, which is beneficial for an accurate measurement using this method of data collection.

The opening of the base was measured to have a surface area:

$$D = 132 \text{ mm}$$

$$S = 0,013684778 \text{ m}^2$$

Using the same equation as in *Chapter 4.6* we can establish the mass air flow to be:

$$\dot{m} = v \cdot S \cdot \rho \quad (10)$$

$$\dot{m} = 4,27 \cdot 0,013684778 \cdot 1,185$$

$$\dot{m} = 0,069204 \text{ kg/s}$$

It would be ideal to obtain multiple points of measurement with different back pressure, to be able to estimate the impact of change of back pressure on the measured velocity and establish a pressure/volume curve. Since the purpose of this thesis is to evaluate feasibility of the concept as a whole and not to propose the optimal solution for a given case, it was decided not to establish this characteristic.

5.2 RADIATOR PARAMETRIZATION

Two radiators were chosen for the concluded experiments, already mentioned before. Radiator A has dimensions very close to the test subject, while the radiator B is used in a production vehicle, so it represents the typical radiator size and density, used in a production passenger vehicle. The radiator B was also sourced along with its production fan, which had been tested in the *Chapter 4.7*.

RADIATOR A – NARROW

Table 16. Radiator A characteristics

Height [mm]	187,5		
Width [mm]	719,7		
Depth [mm]	25,2		
Velocity [m/s]	2	4	6
Pressure drop [Pa]	48,6	127,9	228,7

This radiator was used in the real-world experiments and measurements since its shape fit the test subject perfectly as depicted in the *Figure 11*. The values were extended through polynomial approximation to estimate that the pressure drop for a velocity of 8 and 10 m/s is equal to 348,5 and 495,3 Pa respectively.

RADIATOR B – MQB PLATFORM PRODUCTION VEHICLE COOLER

This radiator was chosen to represent a module, used in a real-world vehicle.

Table 17. Radiator B characteristics

Height [mm]	452,4				
Width [mm]	719,2				
Depth [mm]	25,2				
Velocity [m/s]	2	4	6	8	10
Pressure drop [Pa]	83	202	334	505	700

As it can be identified from the tables, the radiators have the same depth and a similar width.

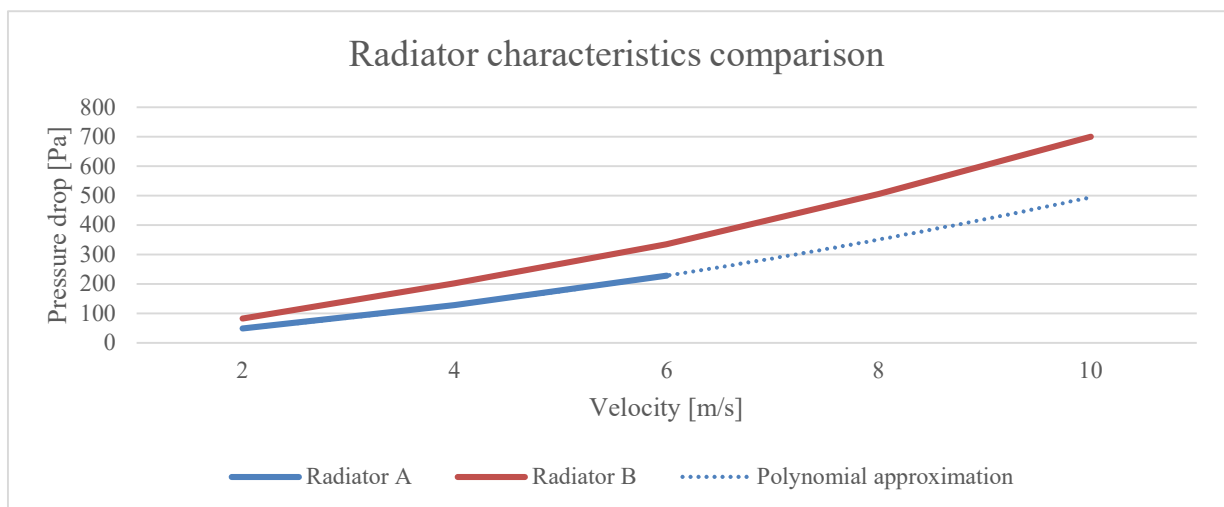


Figure 18. Radiator A and B characteristics comparison

5.2.1 SPECIFYING THE BOUNDARY CONDITIONS

In Ansys CFX software, multiple approaches can be chosen to parametrise the radiator.

It was decided to define the radiator as a porous domain. This simplifies the model, since the individual air channels don't have to be modelled, meshed using extremely fine elements etc. The porous domain can be modelled in a form of a solid block, whose properties are defined numerically.

The porous domain has the following parameters:

- Volume porosity
- Loss Model

VOLUME POROSITY

This parameter defines the ratio of the volume of fluid. Volume porosity of 1 means, there is no restriction for the fluid flow. Volume porosity of 0 means, the material is completely impervious to fluid. [17]

A typical vehicle radiator has a porosity of 0,7 to 0,8. [18, 19] A Volume porosity of 0,75 was chosen to represent both radiators used in experiments.

The impact of porosity had been tested in Ansys CFX application and it was found that the variation of porosity between 0,7 and 0,8 does not have a significant impact on the results. Setting a higher value for the porosity setting also led to a slightly better convergence of the calculation. On the other hand, when a low porosity of e.g., 0,25 was set, the calculation tends to diverge even with a very well-defined conditions.

LOSS MODEL

Directional, Isotropic, or No loss can be specified. In this case, to imitate the behaviour of a radiator, directional loss was chosen. As it is evident from the radiator's construction (depicted in the *Figure 6* at *Chapter 2*) the radiator allows flow only in the direction, normal to its main surface.

DIRECTIONAL LOSS

The directional loss can be specified with cartesian or cylindrical components. Cartesian components were chosen for this application, so the loss parameters in X, Y and Z components will be specified separately.

The directional loss parameters define the direction of possible flow through the porous body. They can also act as a multiplier of further defined streamwise loss parameters. This allows for simulating patterns, that are anisotropic – having different properties in different directions, just like the radiator in this case. [20]

The cartesian components of directional loss were set in accordance with the radiator orientation as: $X=1$, $Y=0$, $Z=0$. *Figure 19* bellow provides illustration of the orientation.

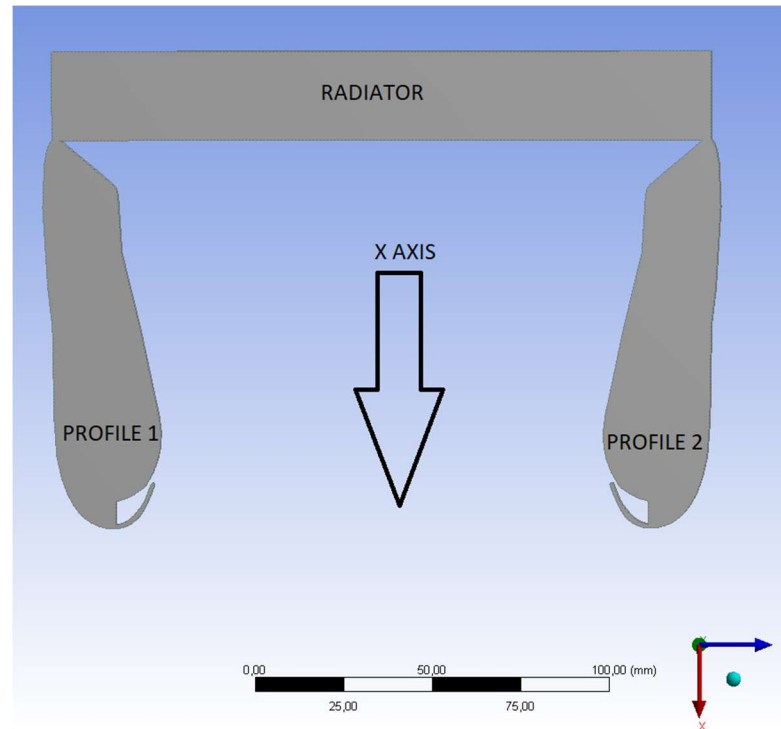


Figure 19. Directional loss definition

STREAMWISE LOSS

The streamwise loss can be defined by multiple options:

- Permeability and Loss coefficients
- Linear and Quadratic coefficients
- No loss

For the purposes of this simulation, the combination of linear and quadratic coefficient was selected to use. Defining these parameters can be a bit tricky, because there is a lot of factors that can influence them.

For the narrow radiator, the p/v curve was obtained from a datasheet supplied by its manufacturer. This curve was approximated by a second-degree polynomial:

$$y = 3,2928x^2 + 18,441x \quad (11)$$

To calculate the quadratic coefficient for Ansys CFX, the following equation is used:

$$c_2 = \frac{2 \cdot B}{\Delta x \cdot \rho} = \frac{2 \cdot 3,2928}{0,0252 \cdot 1,185} = 220,534 \quad (12)$$

Where:

B – Coefficient of the quadratic term [-]

Δx – Depth of the porous material [m]

ρ – Domain density [$kg \cdot m^{-3}$]

c_2 – Quadratic coefficient [-]

For the radiator B, the p/v curve was also obtained.

It was approximated by a second-degree polynomial:

$$y = 3,4429x^2 + 35,583x \quad (13)$$

To calculate the coefficient for Ansys CFX, the following equation is used:

$$c_2 = \frac{2 \cdot B}{\Delta x \cdot \rho} = \frac{2 \cdot 3,4429}{0,0252 \cdot 1,185} = 230,587 \quad (14)$$

It can be observed that the coefficients of the narrow and MQB radiator are of a similar range, which coincides with the comparison in the *Figure 20*.

The linear coefficient was set experimentally as $c_1 = 500$ for both radiators.

TRANSVERSE LOSS

The transverse loss of a radiator is straight-forward to define, since the radiator allows airflow in only one direction, described in directional loss. To define this state, it is recommended to use a streamwise coefficient multiplier of 10 to 100. [20]

It was chosen to use a streamwise coefficient multiplier of 10.

EVALUATION

The chosen parameters were compared with the real-world measurements of the radiator pressure curves. The model proved to be sufficiently capturing the radiator characteristics, mainly in the lower speed region. It tends to slightly diverge in the speeds in excess of 6 m/s which is considered sufficient given the expected operating range being 2 to 4 m/s.

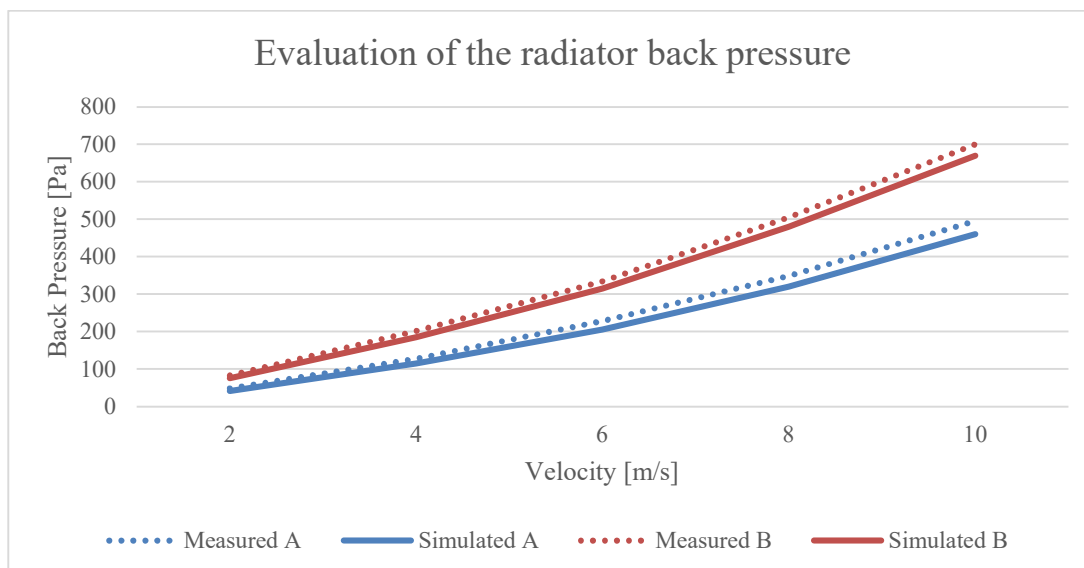


Figure 20. Evaluation of radiator back pressure

6 SIMULATION OF THE ORIGINAL STATE

To ensure that the effects, measured on real subject can be transferred to a computational fluid dynamics simulation with boundary conditions, set in the *Chapter 5*, experiments from the *Chapter 4* were reproduced in Ansys CFX software. These results will be compared to determine the accuracy of the model.

6.1 3D MODEL

For the purposes of CFD simulation, an accurate 3D model was needed.

6.1.1 SCANNING

3D scanner Atos Compact 2M was used to obtain the 3D model of the test subject.

The scanner works based on a light distortion on the scanned surfaces. This creates a high demand for surface uniformity. Also, reflective surfaces tend to produce worse results, since the scanner might confuse reflections with distortions.

To mitigate any unwanted effects and produce a matte, uniform surface a chalk spray was used.

Since the scanner has no possibility of automatic positioning, it must be positioned manually. It also has no mechanical means of determining its position, which creates a challenge for merging individual takes. To solve this problem, software merging and position approximation is used.

The scanned object must be covered with reference points – small circular stickers with a diameter of 7 mm. These are placed on the surface in a semi-random pattern. The requirement is that every measurement must include at least 3 reference points, that were included in the previous measurements. The software then calculates the reference position of the scanner thanks to these 3 basepoints.



Figure 21. Test subject ready for 3D scanning

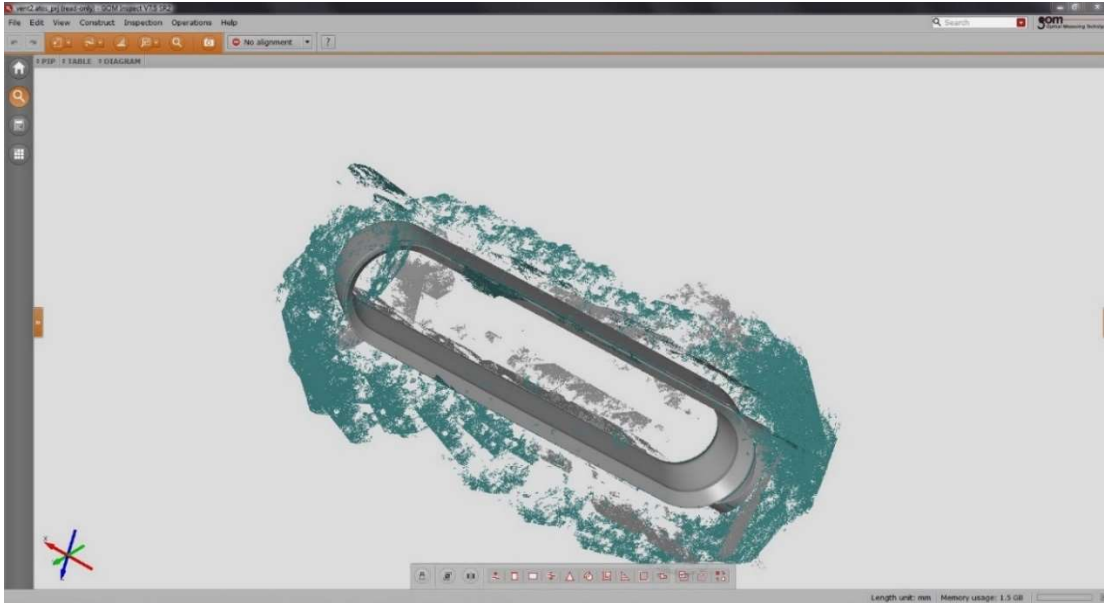


Figure 22. Raw data from the scanner

6.1.2 RAW 3D DATA PROCESSING

The cloud of points, generated from the scanner is imported to GOM Inspect application. The disadvantage of 3D scanning of this type is that along with the scanned surface, the surroundings is scanned as well. In this instance, the table upon which the object was scanned.

This is solved by trimming and deleting the additional points. The remaining points can be merged into a surface and exported as an .STL file.

In this phase, it became apparent that it will be difficult to accurately cover the area through which the air exits the profile, because the thin opening has only a very narrow angle upon which it can be shined through by the scanner's light.

To overcome this deficiency of scanned data, the model was searched for areas, where the scanning angle was close to optimal. Since the object is symmetrical in the sense it consists of a cross section, which is swept along a curve. It was decided to obtain multiple cross sections to compare against each other in case it is not constant. All cross sections in different places of the object were found to be identical, so the one which was of the best quality had been chosen as the basis for the final 3D model. Finally, it was offset by 1 mm on the inner side, to represent a wall-thickness of 1 mm, which was measured with caliper.

Also, the curvature of the whole object was captured and represented as a secondary curve.

6.1.3 FINAL MODEL

It was chosen to generate the model in Autodesk Inventor.

The cross section was swept along the curve. Then the inlet was designed in a simplified manner. The original part has mounting points and other technological shapes. For the purposes of the simulation, these are deemed as a source of instability without a reasonable effect on the simulation, so they were neglected. The geometry can be examined in the *Attachments 9, 10, 11 and 12*.

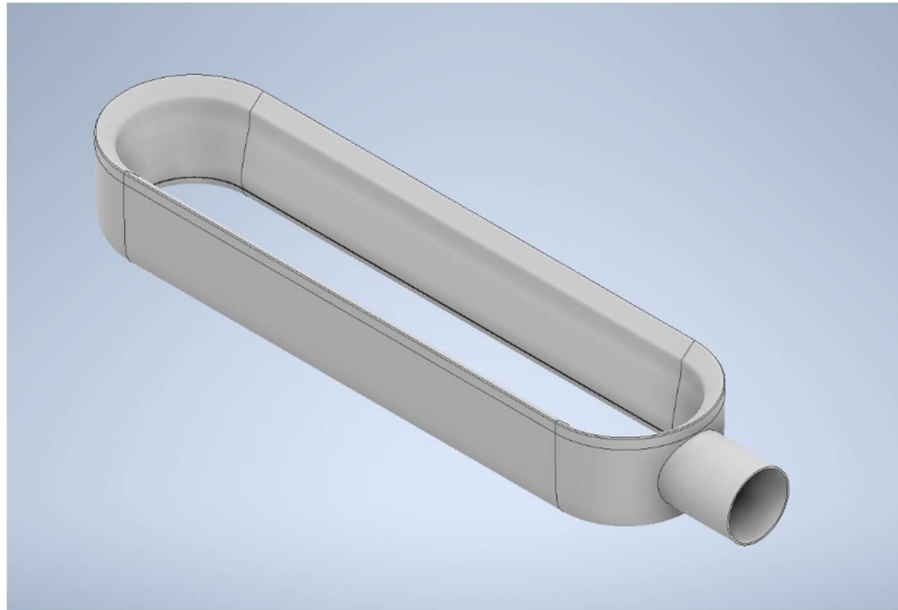


Figure 23. The resulting 3D model of test subject

6.1.4 MODEL PROPERTIES

These properties were generated in Autodesk Inventor environment.

Surface areas had been determined as follows:

$$\text{Intake} = 83\,456,606 \text{ mm}^2 = 0,083457 \text{ m}^2$$

$$\text{Outlet} = 128\,542,139 \text{ mm}^2 = 0,128542 \text{ m}^2$$

6.2 COMPUTATIONAL FLUID DYNAMICS

It was chosen to perform the calculation in ANSYS CFX software. It is widely respected as an industry standard for CFD analysis and offers a great documentation.

Ansys CFX works on a basis of numerically solving system of equations, which describe physical processes in a domain. Domain is a body of fluid – in this case air. The system of equations is based mainly around the Navier-Stokes equation, which describes the preservation of mass and momentum in the domain, supplemented by a chosen turbulence model.

To enable a solution to be calculated, the problem must be discretized. The discretization is achieved through meshing, which is a process, dividing the domain to a finite number of elements.

6.2.1 MESHING

Especially for application in CFD, the mesh must meet strict criteria. If these are not met, the simulation might have a convergence, stability, or inaccuracy problems. For problems of this type, these parameters are critical:

- Skewness – The skewness is defined as a difference between the shape of the element compared to a shape of equilateral element of the same volume. It can be calculated as a subtraction of cell size from the optimal cell size, divided by the optimal cell size. Skewness of 0 represents the best possible mesh, while a skewness of 1 represents unusable mesh. It is recommended to keep the average skewness under 0,33 and to eliminate having the worst element skewness over 0,95.
- Boundary layer – Since the flow in the vicinity of a solid tends to create a very thin cushion layer, that stays theoretically stationary relative to the solid without regards of the air flow speed, it is important to increase the resolution near these solids. The boundary layer specifies the thickness, amount and growth rate of the near-solid mesh elements. This provides sufficient resolution to capture the fluid-solid interactions.

The 3D model was imported into Ansys SpaceClaim software. It is important to note, that the imported model is a model of solids. CFX however needs a model of the domain.

Creation of the domain model is achieved by using Ansys SpaceClaim integrated feature of enclosure. It was decided to create an enclosure, reaching 500mm beyond the object in every direction. The decision was based on providing the simulation with enough spare room to observe phenomena around the object as well as keeping the number of elements reasonably low. High number of elements increases the time needed for calculation.

Lastly, the enclosure's edges were rounded to a radius of $R = 500$ mm to form an ellipsoid-like shape. Eliminating sharp edges from the model is beneficial to its convergence and calculation stability.

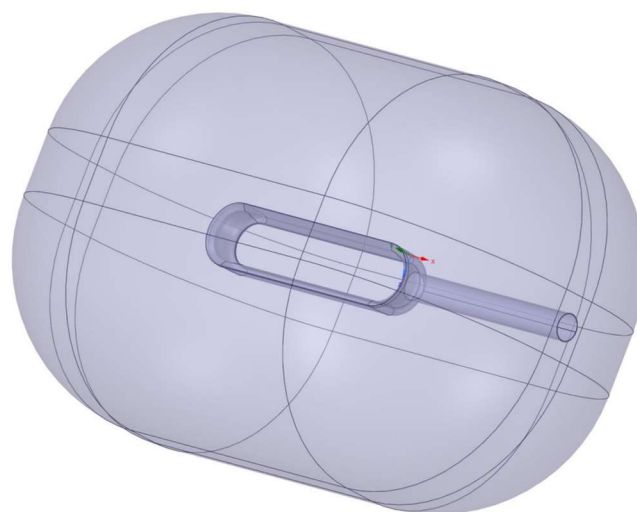


Figure 24. Domain geometry

MESH PARAMETERS

The mesh was prepared in the Ansys Meshing tool.

Main parameters were set as follows:

- Default element size = 0,05 m – maximum size of a single element
- Growth rate = 1,2 – this parameter defines a ratio between adjacent element edge sizes
- Capture curvature = 0,0003 m – curvature with smaller radius will be neglected
- Inflation – creates a set of layers on the surface of the object

As for the inflation, the model contains two groups of surfaces, where the correct setting of inflation is considered. The first consists of the cylindrical shape which serves as the air inlet. The second group consists of all the surfaces of the test subject's profile, that encounter flowing air. A decision was made to include all the test subject's surfaces in this group, even those, which do not receive any significant airflow around them, to help with a possibility of capturing unexpected events. To capture the interaction of fluid near the wall, it is important to have an increasingly smaller mesh sizing in the wall's close vicinity. This is achieved by the inflation, which creates the first layer of a given thickness at the edge of the domain, while increasing the thickness of the upcoming layers by the coefficient of growth rate. Both inflations were defined with 3 parameters:

- First layer thickness = 0,0002 m
- Number of layers = 10 and 15 respectively
- Growth rate = 1,2 – this parameter defines the relative thickness of two adjacent layers

FINAL MESH

The detailed view of critical mesh areas can be found in the *Attachments 13, 14, 15 and 16*.

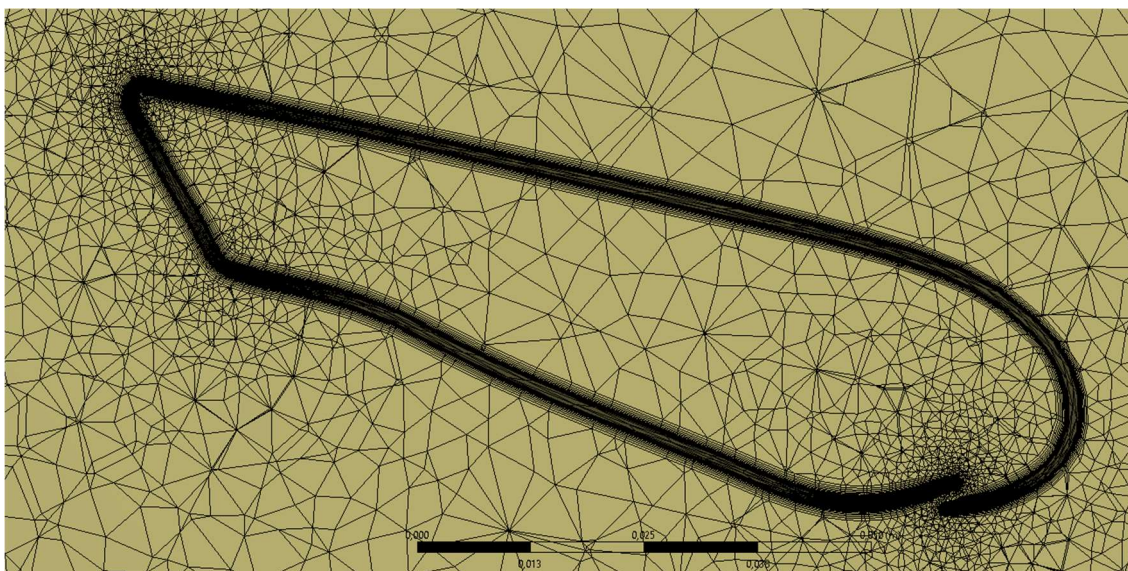


Figure 25. Cross sectional detail of the test subject's mesh

MESH QUALITY

Table 18. Mesh quality

Mesh Metric	Skewness
Minimum	6,9693 e-6
Maximum	0,9201
Average	0,30442
Standard deviation	0,16527

The elements with the worst skewness of 0,89 and worse were displayed on the model. Since they appear in the area, where no important airflow is expected, this mesh was deemed sufficient for this simulation. They can be observed in the *Attachment 17*. The final mesh featured 6 445 931 nodes and 16 838 082 elements.

6.2.2 SIMULATION PARAMETERS

To be able to simulate the problem, boundary conditions must be set.

The domain was defined as Air at a room temperature of 25 °C.

Reference pressure was set to 1 bar. This setting helps with simulation convergence since it dramatically decreases relative differences in pressure across the simulation. Since most fluid dynamics equations tend to be mathematically unstable, this is an important parameter.

Heat Transfer – the simulation is considered isothermal.

Turbulence model – Shear Stress Transport. This model combines $k - \varepsilon$ and $k - \omega$ models. $k - \varepsilon$ is a model, which is aimed at calculating turbulence in the open space. $k - \omega$ is a model, aimed at calculating turbulence near solid walls.

3 boundary conditions had been set:

- Opening – The border, where the mesh ends was set as an opening with 0 Pa relative pressure. This ensures, that air can pass in both directions through it with no resistance.
- Inlet – Here, the mass air flow was set according to a *Chapter 5* as $\dot{m} = 0,069204$ kg/s
- Walls – Every other surface of the mesh was set as a smooth wall.

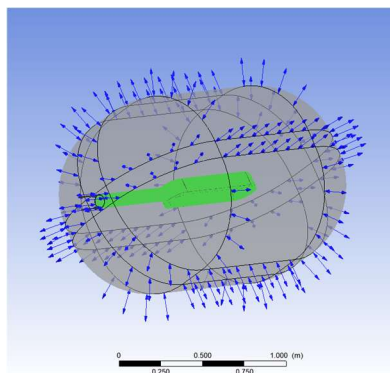


Figure 26. Test subject in the domain with boundary conditions set

6.2.3 SIMULATION CONVERGENCE

In the solution setting, it was defined that the RMS residual target is 10^{-4} . This value represents the default setting of the ansys CFX and according to manual is considered as a suitable balance between the calculation accuracy and convergence time. [20]

Since the calculation is iterative, it is a good practise to monitor a set of user defined parameters during the calculation, to determine if the simulation is converging as expected. On top of the default monitors, it was decided to monitor the pressure loss of the profile. This monitoring parameter was defined as a Total Pressure at the Inlet port. It can be noted that the curve is converging rather smoothly, which shows that the calculation is stable.

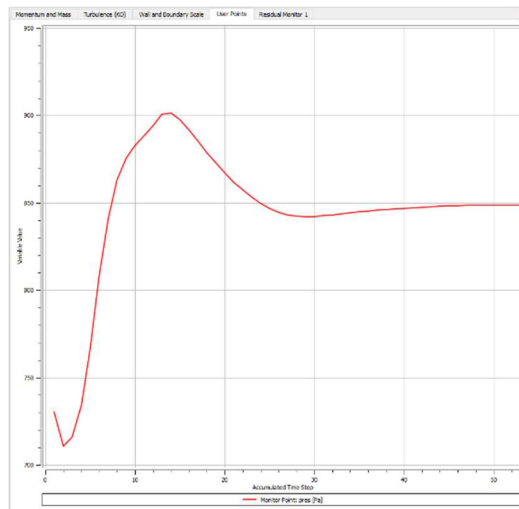


Figure 27. Total pressure at inlet convergency [Pa]

The simulation convergence and residuals can be observed in the *Attachments 18* and *19*.

6.3 RESULTS EVALUATION

In this chapter, results of the simulations are going to be evaluated against the physical measurements.

6.3.1 YPLUS

Since the whole concept heavily relies on the airflow in the vicinity of walls and their interactions with air and turbulence airflow, it is necessary to ensure suitable Yplus values. Yplus is a dimensionless number, which characterises the distance from the wall to the first node. [21]

It is recommended that Yplus is maintained as low as possible. In general, acceptable values are single digit numbers as close to 0 as possible – that would characterize perfect mesh from the perspective of near-wall turbulence evaluation.

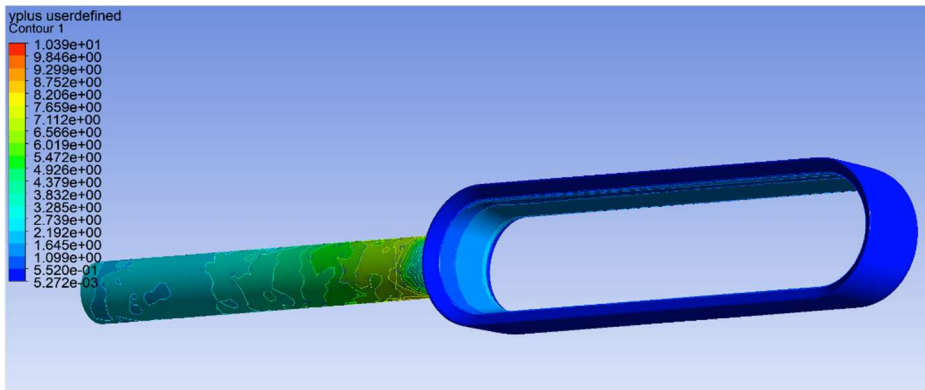


Figure 28. *Yplus*

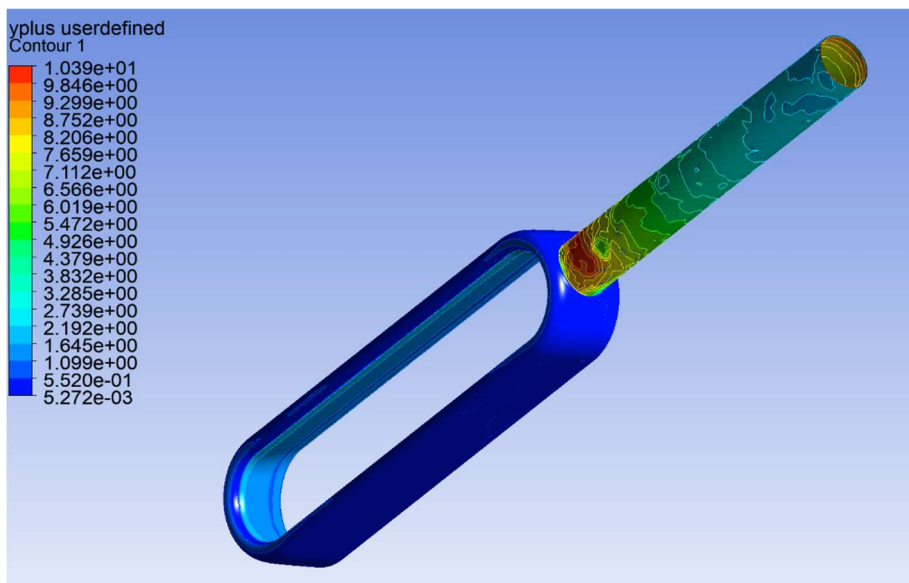


Figure 29. *Yplus max*

As it can be seen in *Figures 28* and *29*, the highest recorded *Yplus* value appeared at the point, where the air inlet interfaces the Dyson profile at a value of 10,4. Since the interaction of air flow in this part of the model is not evaluated, it is deemed unimportant.

The most important surfaces for the evaluated behaviour are the inner parts of the Dyson profile. They're *Yplus* values can be found in the range of 1 to 2 which can be considered as a suitable range, providing accurate simulation of near-wall interactions.

6.3.2 DATA COLLECTION

To provide a base measurement, it was decided to simulate the exact same testing methodology, as described in the *Chapter 4.1*. Multiple measurement points were created in the same layout as in the real experiments. To simulate the anemometer probe, control surfaces of its inner diameter of 18 mm were created.

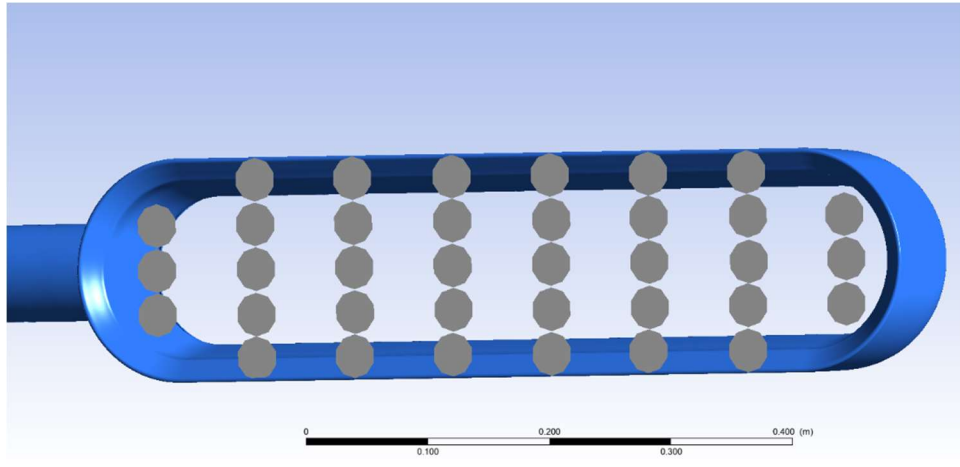


Figure 30. Measurement points on the simulated test subject

To obtain the values, it was assumed, that the Anemometer probe averages the air velocity, hitting its propeller in the direction coincident with its rotational axis. To simulate for this, a CFX expression was proposed in the following form: $\text{areaAve}(\text{Velocity } v)@ \text{measurepoint}(x)$

The value of this expression was captured for every control surface and reported to the table in the same format as from the real-world measurements.

OUTLET DATA ON SIMULATED MODEL

Table 19. Air speed outlet on simulated model [m/s]

Inlet	O/R	5,12	4,7	4,64	4,8	4,76	4,75	O/R
	2,15	2,36	2,33	2,34	2,4	2,45	2,55	4,46
	2,25	2,35	2,36	2,36	2,4	2,47	2,59	2,66
	2,16	2,36	2,34	2,34	2,39	2,45	2,55	4,45
	O/R	5,33	4,81	4,75	4,78	5,1	4,71	O/R

$$V_{out4csav} = 3,3269 \text{ m/s}$$

$$\dot{m}_{out4cs} = 0,5068 \text{ kg/s}$$

ABSOLUTE DEVIATION FROM THE REAL-WORLD MEASUREMENT

Table 20. Absolute deviation from the real-world measurement, velocity [m/s]

Inlet	0	0,24	-0,7	-2,03	-1,87	-1,82	0,54	0
	1,14	1,1	0,92	0,79	0,69	1,38	-0,28	2,74
	1,94	1,34	1,08	1,09	1,2	1,45	1,73	0,2
	1,83	1,77	1,15	1,21	1,39	1,56	1,42	2,47
	0	0,25	-0,74	-1,63	-2,25	-3,61	-3,52	0

$$\text{Average absolute velocity difference} = 0,3936 \text{ m/s}$$

$$\text{Average absolute mass flow difference} = 0,06 \text{ kg/s}$$

$$\text{Relative deviation from the measured values} = 13,4 \%$$

Results of this measurement shows that the distribution of the simulated air speed is similar to the distribution of measured air speed. It can be noted, that in the simulation, the highest recorded speeds were lower, while the speeds across the surface were higher. This might be a problem, caused by the methodology of measurement, described below in *Chapter 6.4*.

6.3.3 EVALUATION OF THE MEASUREMENT

This type of measurement was done to ensure the reliability of averaging the surfaces as opposed to measuring individual sub-surfaces.

To obtain the required values faster, using integrated tools, an Iso control surface was set to fill in the outlet region. Further, the expressions were set as follows:

Mass flow outlet: $\text{areaAve(Velocity)@Iso_Outlet}\cdot\text{area@Iso_Outlet}\cdot\text{AirDensity}$

Average outlet velocity: $\text{areaAve(Velocity)@Iso_Outlet}$

Upon measurement of the surface, using the integrated expression functions of Ansys CFX, these values have been observed:

$$V_{out4surfaceave} = 3,48497 \text{ m/s (Non-directional)}$$

$$V_{out4surfaceavedirectio} = 3,1051 \text{ m/s (In the normal direction)}$$

$$\dot{m}_{out4surfaceave} = 0,536 \text{ kg/s (Non-directional)}$$

$$\dot{m}_{out4surfaceavedirectional} = 0,477 \text{ kg/s (In the normal direction)}$$

Meaning the average deviation of V_{out} non-directional compared to the values achieved by individual control surfaces is equal to 4,75%.

The average deviation of Mass air flow non-directional compared to the values achieved by individual control surfaces is equal to 5,76%.

It is important to note that when trying to evaluate the outlet surface average speed and mass flow, it proved to be very difficult to create an ISO clip that would completely cover the outlet area, while not protruding outside the outlet area perimeter.

This discrepancy can have a negative impact on the measurement reliability. In the next designs this will be addressed with caution and a different approach to 3D modelling, that would allow for an exact definition. The root of this problem seems to be the sharp edge of the model.

Since evaluating the measurement by individual control surfaces is laborious and has a great possibility of error, it was decided that in the upcoming simulations, the expression function will be used to determine the speed and mass flow through the whole surfaces, while being supplemented with a contour, depicting the distribution of the parameter in visual form. his approach will also enable the model to use parametric optimisation in the future. Furthermore, the non-directional approach will be used.

INLET DATA ON SIMULATED MODEL

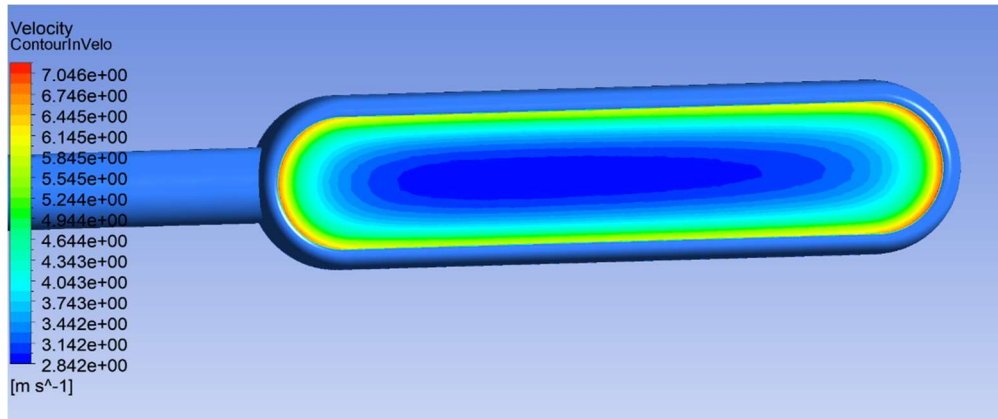


Figure 31. Air speed distribution on simulated inlet

$$V_{in4ave} = 3,95 \text{ m/s}$$

$$\dot{m}_{in4} = 0,44 \text{ kg/s}$$

OUTLET DATA ON SIMULATED MODEL

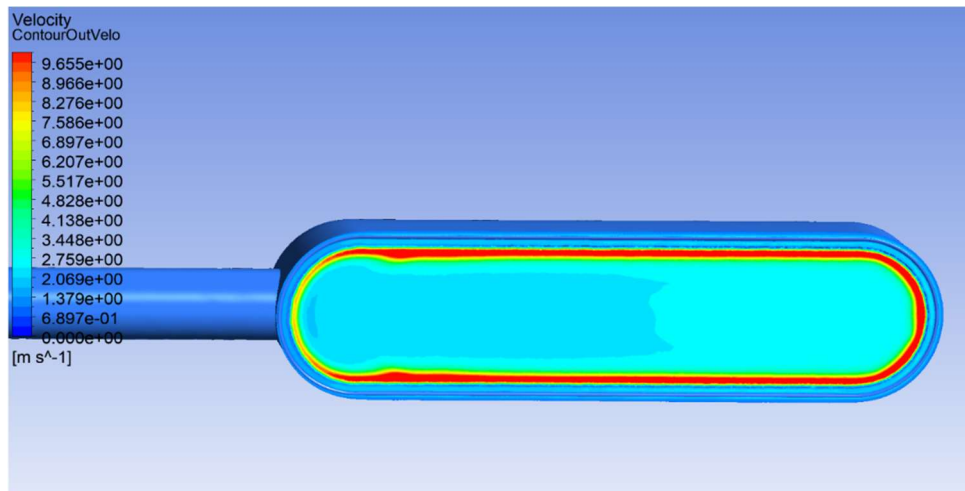


Figure 32. Air speed distribution on simulated outlet

$$V_{out4a} = 3,48497 \text{ m/s}$$

$$\dot{m}_{out4} = 0,536 \text{ kg/s}$$

6.4 SIMULATION ACCURACY

Table 21. Simulation accuracy

	Velocity intake [m/s]	Mass flow intake [kg/s]	Velocity outlet [m/s]	Mass flow outlet [kg/s]
Measured values	1,6241	0,1606	2,9333	0,4468
Simulated values	3,95	0,44	3,48497	0,536
Absolute deviation	2,3259	0,2794	0,55167	0,0892
Relative deviation	143,21%	173,97%	18,81%	19,96%

Disparity had been found between the intake side of the real-life measurement and intake side of the simulated body.

To clarify, where the measurement error might have occurred, it was decided to check the entire system integrity by verifying complete mass air flow. Mass flow intake subtracted from mass flow outlet should be equal to the mass flow at inlet. However, it was found that it is not.

For the real measurement, the inlet mass flow was calculated to be:

$$\dot{m}_{out1} - \dot{m}_{in} = 0,2862 \text{ kg/s} \quad (15)$$

For the simulation, the inlet mass flow was calculated to be:

$$\dot{m}_{out4} - \dot{m}_{in4} = 0,096 \text{ kg/s} \quad (16)$$

However, the measured mass flow, provided by the compressor is only:

$$\dot{m}_{mea} = 0,069204 \text{ kg/s}$$

It appears that the simulation is mostly correct, having only 0,0268 kg/s disparity accounting for only 5% of the total mass flow. This is further supported by the outlet iso surface problems, described in the *Chapter 6.3.3*.

Using the value for simulation outlet mass flow, which is calculated from individual control surfaces, in the *Chapter 6.3.2*.

$$\dot{m}_{out4cs} = 0,5068 \text{ kg/s}$$

The disparity comes down to only 0,0022 kg/s accounting for only 4,1% of total mass flow.

Upon closer inspection of the simulation air flow distribution, it seems as though the air is being sucked in tightly around the surface of the Dyson profile, which is an expected behaviour. This could indicate that the measurement method chosen for the intake side was sub-optimal. The anemometer is unable to measure the airflow, tightly attached to walls.

This can be observed in the *Figure 33* bellow.

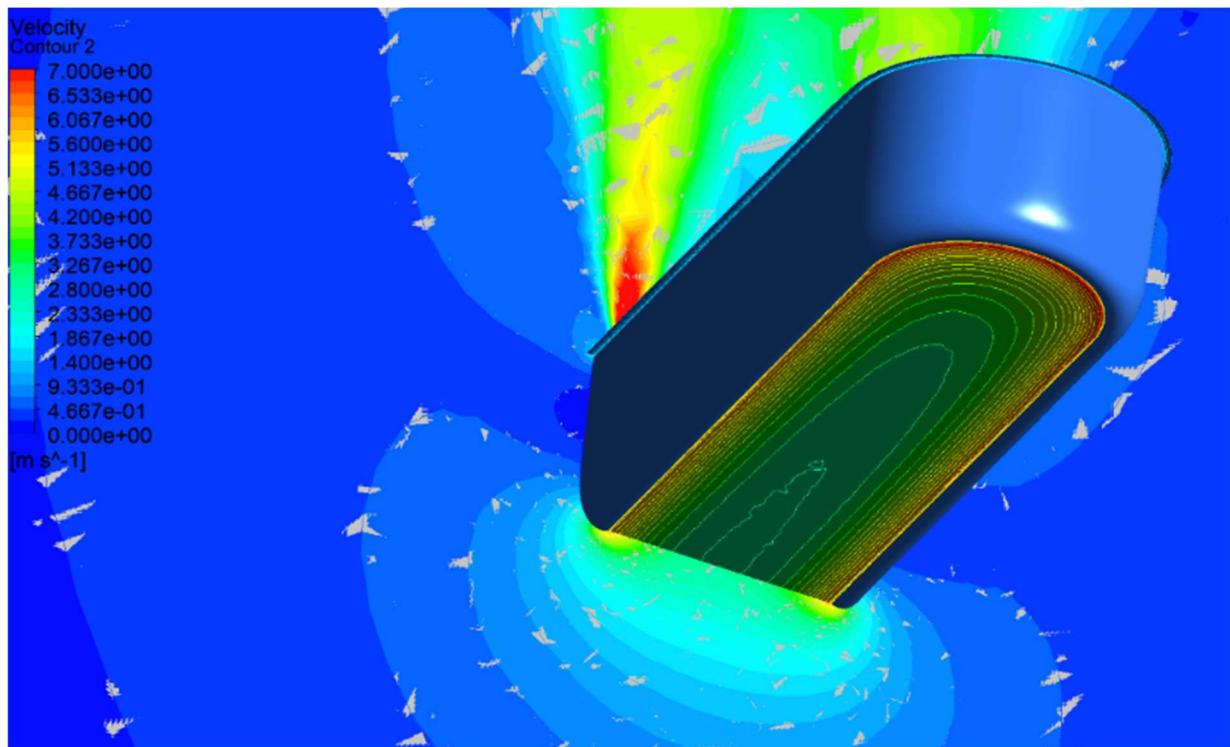


Figure 33. Air intake detail

To further backup this theory, it is interesting to have a second look at the measured intake air speed distribution, seen in *Table 5* in the *Chapter 4.6.1*. The air speed around the outer edges is lower, than the speed in the centre of the profile. This along with the total mass flow disparity suggests that the problem most likely occurred in the real-world measurement methods of the intake side.

It was concluded that the anemometer is incapable of measuring the air speed in the vicinity of the measured device edges. Given the accuracy of the measured outlet speeds, it was decided to consider the 3D model and initial simulation as sufficient, since the outlet speeds and mass flow do match the real-world measurements with a reasonably low deviation.

7 OPTIMALIZATION

Since it was evident, that a high number of calculations is going to be performed, it was decided to create a partial, parametric model of the simulation.

The main objective was to be able to change the model easily for every iteration and to reduce the calculation time, while retaining accuracy of the simulation.

7.1 PARAMETRIC MODEL

It was decided to create the model in Ansys Design Modeller application, which enables to define measurements as parameters.

The original cross section was imported into the Design Modeller and defined as a spline with a set of control points. The coordinates of these points were parametrized. This created a very flexible model, that can be modified easily by redefining the coordinates of individual control points.

To further simplify the model, it was decided not to sweep it along the whole curve, but instead, define only a 100 mm long, straight section. This will mainly dramatically decrease the time needed for computation of every iteration, while also being a better representation of the planned final design. Since a radiator is usually of a rectangular shape, having a curvature on the ends of the profile does not really seem optimal for the radiator coverage. It is expected that the final shape of the profile will be a set of multiple straight profiles.

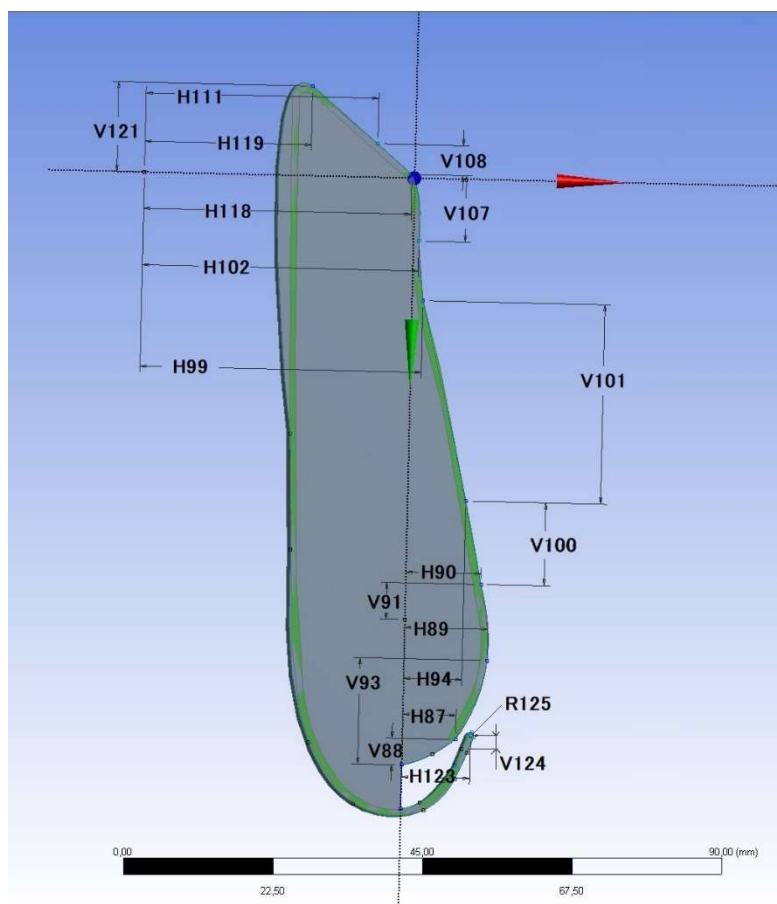


Figure 34. Default parametric model with control points

In the *Figure 34*, it can be observed that the model matches the original cross section (highlighted in green) well. There is a significant deviation on the left upper part, however on this surface, no airflow is present. Thus, this deviation is considered acceptable.

The boundary conditions for the parametric model will be set in accordance with the boundary conditions for the full model.

As specified in the *Chapter 6*, the mass flow is equal to $\dot{m} = 0,069204$ kg/s

This is true for the default profile, which has a circumference of 1 522 mm measured at the edge of the channel, where air is exiting the profile.

To correct for the shorter profile in the simulation, the new inlet mass flow is set to directly correlate with the length of the profile:

$$\dot{m}_{para} = 0,069204 \cdot \frac{100}{1522} = 0,0045469 \text{ kg/s.} \quad (17)$$

7.1.1 PARAMETRIC SINGLE-SIDE DEFAULT MODEL

From the experimentation with the cross-section in design modeller application, it turned out that when the profile was left hollow with a thin wall, it was prone to failures and showed an unstable behaviour upon parameters change. To combat this, another assumption was made, and the inlet was remodelled.

As it can be seen in the *Figure 34*, the cross section is now made of a full material with only a short hollow space, near the edge, where air escapes from the profile. The vertical surface of this hollow space will be used as the inlet in upcoming simulations. Influence of this simplification needs to be evaluated.

The model was meshed in accordance with the settings in the *Chapter 6.2.1* producing comparable mesh quality. The enclosure shape was replaced by a sphere since it better covers this design.

This mesh has a similar coefficient of the average skewness, yielding slightly better results than the original, while including roughly 30 times less elements.

- Average skewness = 0,27652
- Nodes = 193 207
- Elements = 630 104

To introduce some context, this partial model was able to converge 98% faster than the original full-size model.

BOUNDARY CONDITIONS

The boundary conditions reflect the boundary conditions set for the original simulation in the *chapter 6.2.2*.

- The edge of the enclosure is defined as an opening with 0 difference in pressure.
- Inlet mass flow is set to $\dot{m}_{para} = 0,0045469$ kg/s.
- All other surfaces are defined as walls.

SIMULATION RESULTS

The convergence of the simulation was similar to the convergence of the original design from the perspective of iterations number.

Yplus was found to be within 0 and 1,5 on most of the model, while peaking at 2,5. This can be considered a solid base for an accurate near-wall turbulence simulation. The distribution of the Yplus values can be found in the *Attachment 20*.

To illustrate the airflow, two streamlines were added for visualisation.

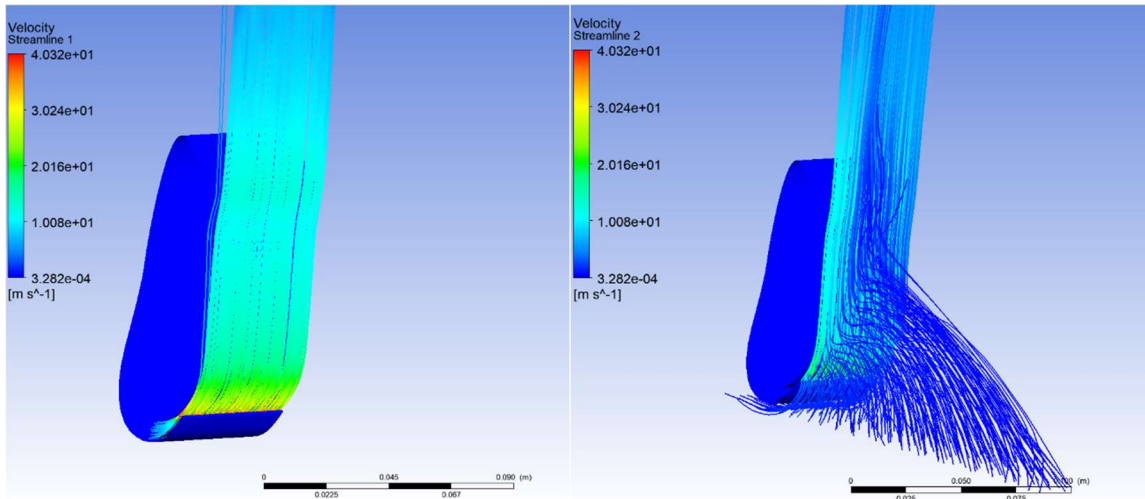


Figure 35. Single side parametric model streamline airflow visualisation

On the left side, only air, flowing from the inside of the profile is visualised. On the right side, only air, sucked in from the surrounding domain is represented. It can also be represented as air, sucked in through the intake part of the original profile.

An interesting phenomenon can be observed in the right-side of the *Figure 35*.

The air appears to be sucked in along the bottom curvature of the profile. This finding supports the thesis in the *Chapter 6.4*, where the possible sources of inaccuracy are discussed. This is explaining, why the anemometer probe was unable to detect this flow, when placed in front of the intake of the Dyson fan.

FLOW DATA EVALUATION

As it can be observed in the *Figure 35*, the airflow is being attached very closely to the profile. This is most likely caused by the lack of the second, opposing profile. There is no closed passthrough area, thus a creation of an area with low pressure is not possible. Only the results of Coanda effect can be observed, resulting in the attachment of the air flow to the wall.

In the *Figure 36* bellow, it can be observed that the air speed distribution is similar to the whole model simulation. However, a higher maximum velocity was achieved. In this case, a maximum of 11,13 m/s was measured, in the whole model simulation a maximum of 9,66 m/s was measured.

This deviation might be caused by the lack of the second profile, eliminating the possibility of creating enclosed area of lower pressure, resulting in a smaller loss for the flow, allowing it to reach higher speeds.

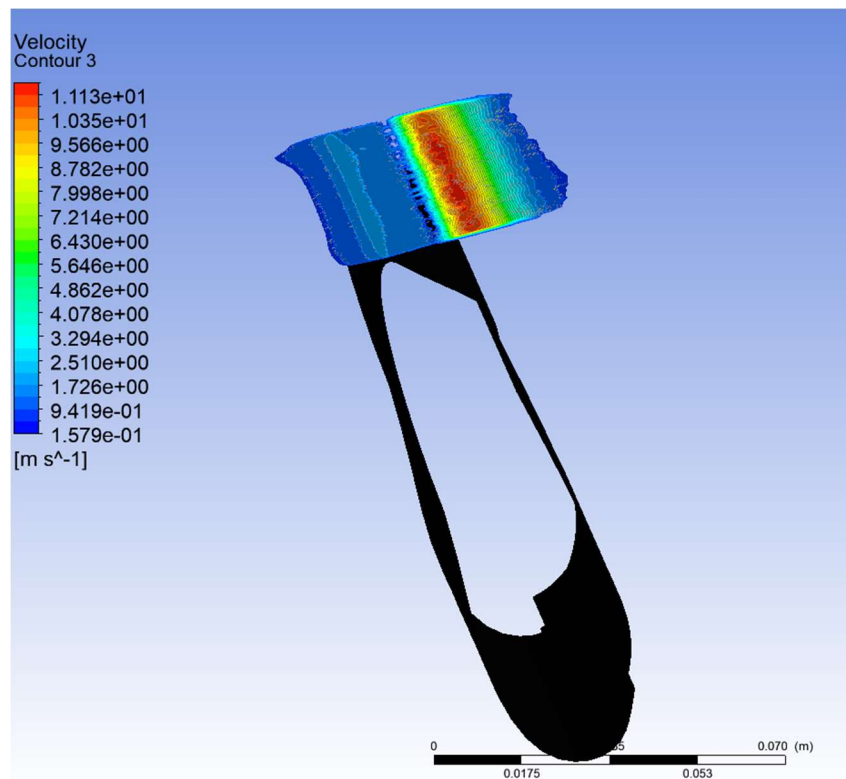


Figure 36. Outlet air speed

Also, to compare the change in the air inlet design, a pressure monitor was placed to the simulation. As mentioned in the *Figure 27* in the *Chapter 6.2.3*, the back pressure of the original profile was 849 Pa.

This parametrized model achieved a back pressure of 829 Pa, which represents a loss of 2,4%.

CONCLUSION

The main objective of this simulation was to prove that the parametrisation and simplification did not have any significant impact on the results. The pressure loss of 2,4% or 20 Pa can be attributed to the lack of intake tube and lack of flow through the hollow profile. The air speed contour does seem like it is proportional to the original design, but the measurement of the total mass flow in this model is problematic hence its open design. The next model should produce more valuable results and provide confirmation of the statements.

7.1.2 PARAMETRIC SYMMETRICAL DEFAULT MODEL

To address the deficiencies of the previous model, it was decided to include the other side of the profile as well. This will create an enclosed passthrough, where an area of negative pressure between the two profiles can be formed. To enclose the inner volume from the remaining two sides, it was decided to introduce a translational symmetry to the simulation. It is defined by a set of two planes, which enclose the profiles – the positioning of these planes can be seen in the *Figure 37* bellow as a hollow part in the contour.

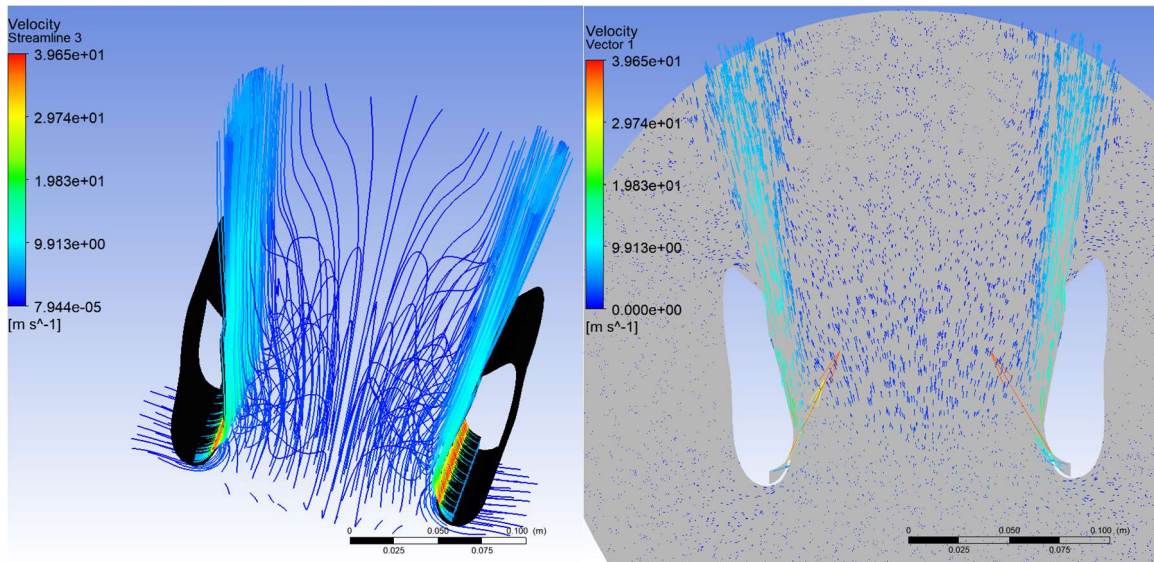


Figure 37. Dual side parametric profile airflow visualization

As it can be observed, the airflow follows the previously measured and simulated patterns.

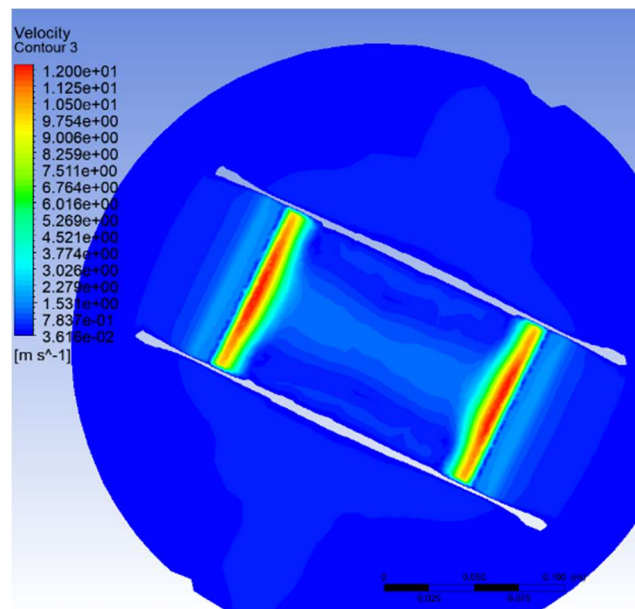


Figure 38. Air Speed distribution on the outlet

The total inlet pressure is basically identical to the previous single-side simulation at 830 Pa.

The air speed was measured across the surface according to the measuring methodises by individual measuring points similarly to the *Chapter 6.3.2*.

The 4th column from the original measurement and simulated model were used to make this comparison:

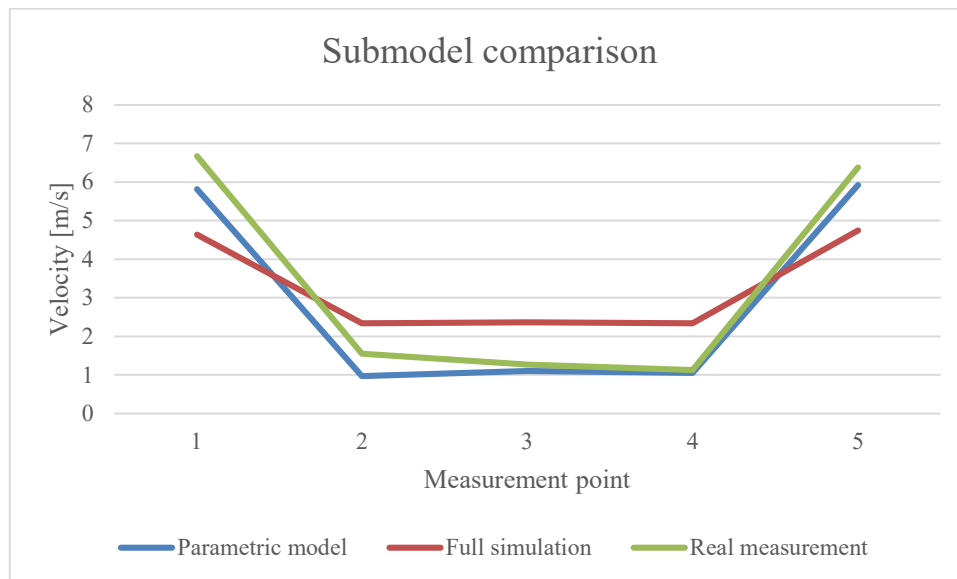


Figure 39. Measurement and simulation comparison

It can be noted that the parametric model does follow the real measured values accurately, while the full simulation model has a visible deviation of velocity distribution across the outlet. This is most likely caused by the internal part of the profile, that was neglected in the full simulation design.

7.2 RADIATOR PARAMETRISATION

7.2.1 DEFAULT STATE EVALUATION AND CONFIRMATION OF ESTABLISHED COEFFICIENTS

As of *Chapter 5.2*, radiator defining coefficients and conditions were calculated.

To evaluate the correct settings of the simulation, it was compared to the real-world measurement.

A Dyson fan with radiator and 300mm ducting was simulated. This concept was chosen for the purposes of calibrating the model. It would be highly impractical to implement in a real-world application, however the 300mm ducting provides a space for the air flow linearisation and turbulence settlement. This results in a relatively linear air flow, that is optimal for assessing the radiator properties. Since the real-world measurement was done on the radiator A, the porous zone was defined as follows:

$$\begin{aligned}
 &\text{Depth} = 0,0252 \text{ m} \\
 &\text{Volume porosity} = 0,75 \\
 &\text{Streamwise direction } x=1, y=0, z=0 \\
 &\text{Streamwise loss linear coefficient} = 500 \\
 &\text{Streamwise loss quadratic coefficient} = 220,534 \\
 &\text{Transverse loss streamwise coefficient multiplier} = 10
 \end{aligned}$$

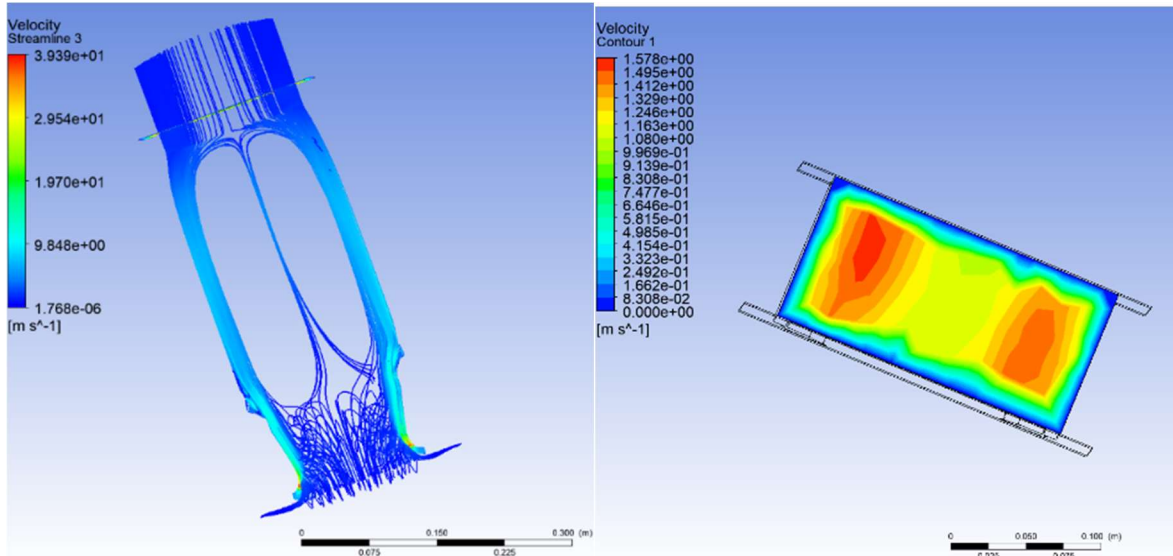


Figure 40. Radiator parameters evaluation

It can be observed, that when the air hits the radiator, significant turbulence appears as a result of the air deflection. This is caused by the air not hitting the radiator in a normal direction, which is crucial for efficiency. This effect was observed on the real-world model, as it can be seen in the *Chapter 4.6.3*.

An inlet back pressure was measured to be 851,5 Pa which matches the expectations. Since in this experiment, the air exits through an enclosed surface, it is easy to measure its mass by incorporating Ansys CFX expression in the form of: `MassFlow@Region`. It was established by the simulation that the mass flow through the radiator is equal to:

$$\dot{m}_{simrad1} = 0,03041 \text{ kg} \cdot \text{s}^{-1}$$

Establishing the original mass flow is challenging due to the uneven distribution across the surface of the radiator caused by the insufficient design of the original Dyson Fan. Outlet speed data from the *chapter 4.6.3* were used.

It was chosen to apply multiple averaging algorithms to obtain the average velocity. The mass flow is then calculated as explained in the *Chapter 4.6* while establishing the surface area as the surface area of the simulated, partial model.

$$S_{partial} = 0,1 \cdot 0,182 = 0,0182 \text{ m}^2$$

Table 22. Velocity of the real-world outlet measurement adjusted for airflow through surface of the simulated size

Method	Velocity [m/s]	Mass flow adjusted for partial surface [kg/s]	Deviation [%]
Average	1,192	0,02543	19,6
Average cut off	1,367	0,02915	4,3
Average column 5	1,42	0,03029	0,4
RMS average	1,241	0,02647	14,9

Average deviation	9,8
-------------------	-----

- Average represents an arithmetic average.
- Average cut off implements arithmetic average, however all values of $v < 1$ m/s were neglected, resulting in neglecting the 1st and 2nd columns.
- Average column 5 represents an arithmetic average of only column 5.
- RMS – root mean squared – in another words - effective value.

This radiator parametrisation was deemed sufficient since the deviation averages to 9,8%. Furthermore, when considering only spaces, not influenced by the deficiency of original Dyson design, practically perfect match is achieved.

MQB RADIATOR EVALUATION

For the MQB radiator, the definition of porous zone was left identical, only the Streamwise loss quadratic coefficient was set to 230,587 as defined in the *Chapter 5.2*.

Resulting mass flow was

$$\dot{m}_{simMQBrad} = 0,029784 \text{ kg} \cdot \text{s}^{-1}$$

This accounts for a deviation of 2,1% compared to the narrow radiator. For any further simulations, the streamwise loss quadratic coefficient will be set to 230,587 to simulate the MQB radiator, which will be used to measure the final design.

7.2.2 INCORPORATING THE RADIATOR INTO THE PARAMETRIC MODEL

To reflect space, that is available for the radiator installation in a traditional vehicle, the dimensions of the device had to be drastically reduced. It was decided to mount the profiles directly in front of the radiator, neglecting the 300 mm ducting from previous simulation and experiment.

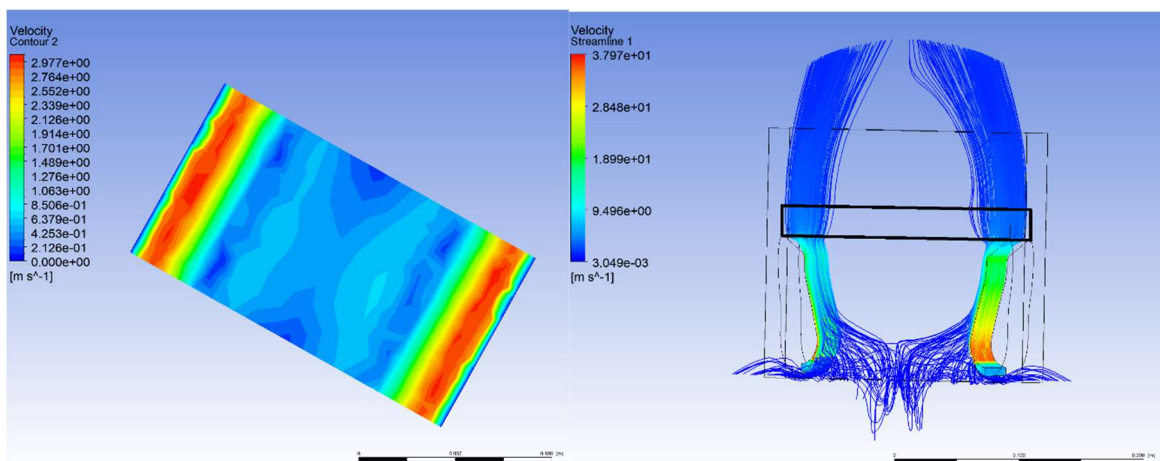


Figure 41. Parametric dual side model with radiator directly attached to the profiles (highlighted in higher wireframe thickness)

The obtained mass flow through the radiator from the simulation is

$$\dot{m}_{simpararad} = 0,017416 \text{ kg} \cdot \text{s}^{-1}$$

The drop in mass airflow is expected, since the turbulent air, not hitting the radiator in normal direction is deflected back, creating a very noticeable turbulence. It also must be noted that the inlet pressure was measured at 750 Pa, which is a 13,2% drop from the original value. It is most likely caused by the turbulence near the inlet channel, where the air exits the profile.

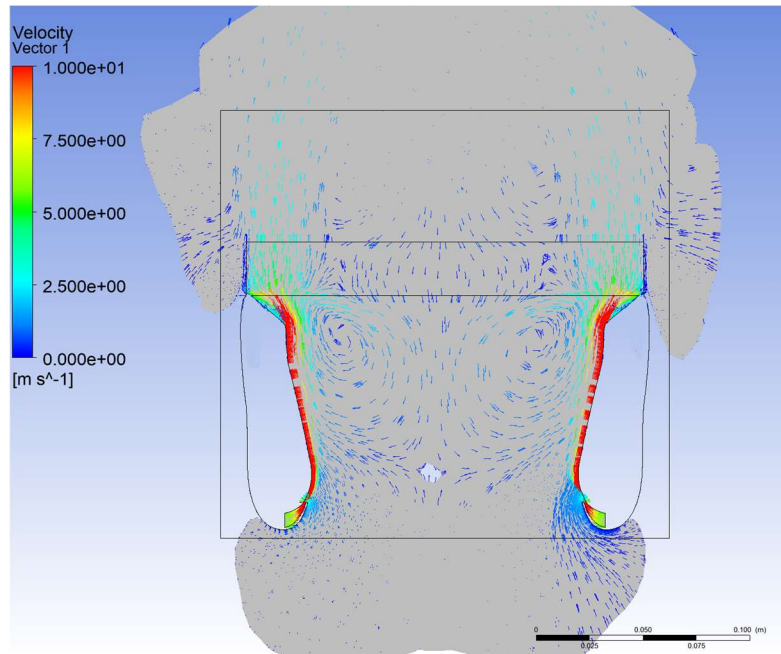


Figure 42. Parametric dual side model with radiator directly attached to the profiles, turbulence evaluation

A vector map was generated to better describe the vortices. It can be noted that in the middle of the radiator a backwards flow appears on a non-negligible area. The speed in this area is however close to 0 m/s so it might be interpreted as an area with no flow whatsoever.

7.3 CHARACTERISTIC MODEL ELEMENTS

This chapter is aimed at experimenting with individual elements of the original design and seeing their impact on the flow behaviour. Each surface will be tested, some in multiple ways, to observe the effects of given changes.

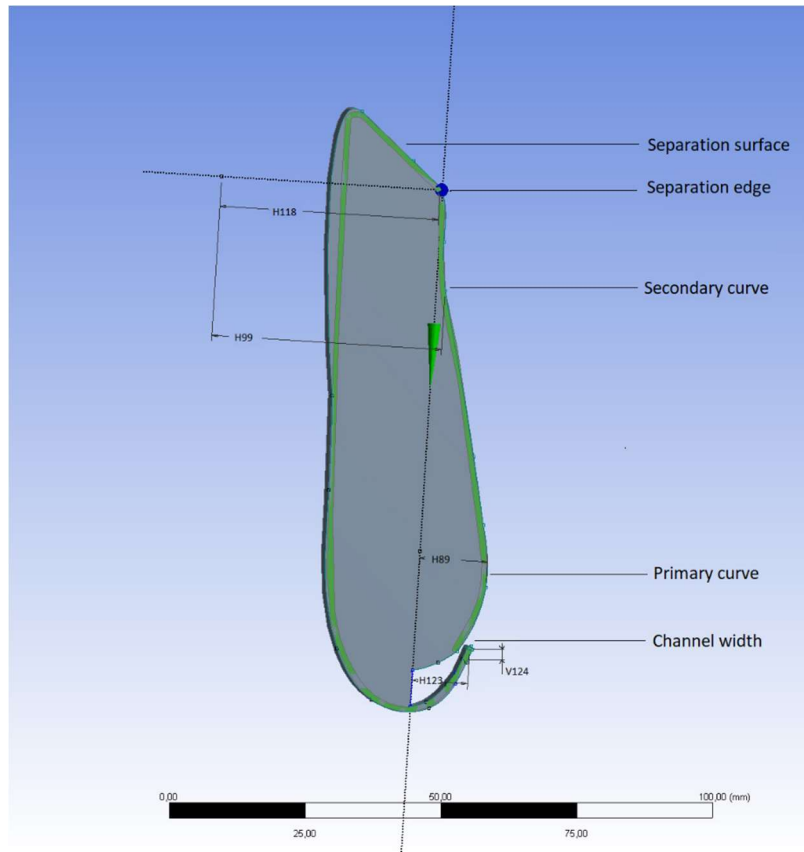


Figure 43. Profile elements

7.3.1 SEPARATION SURFACE DELETE

The edge was filled up to create a straight ending to the profile.

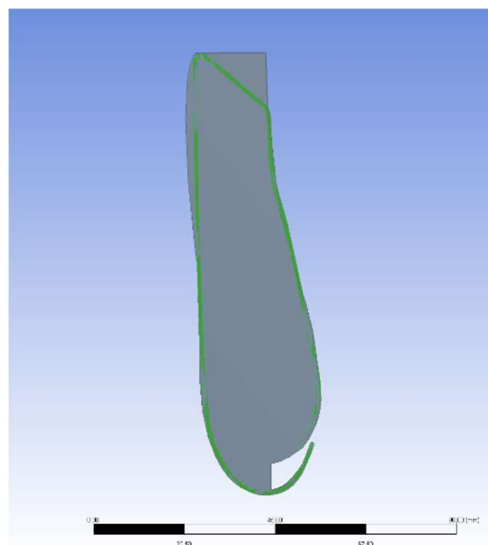


Figure 44. Separation surface delete

In the previous simulation, in the *Chapter 7.2.2*, it can be observed that the space, that is now filled up, was used for the air to decrease its speed, and normalize its direction with the radiator mesh.

In this simulation, it will be tested, how the model behaves, when the air is directed to the direction normal to the radiator.

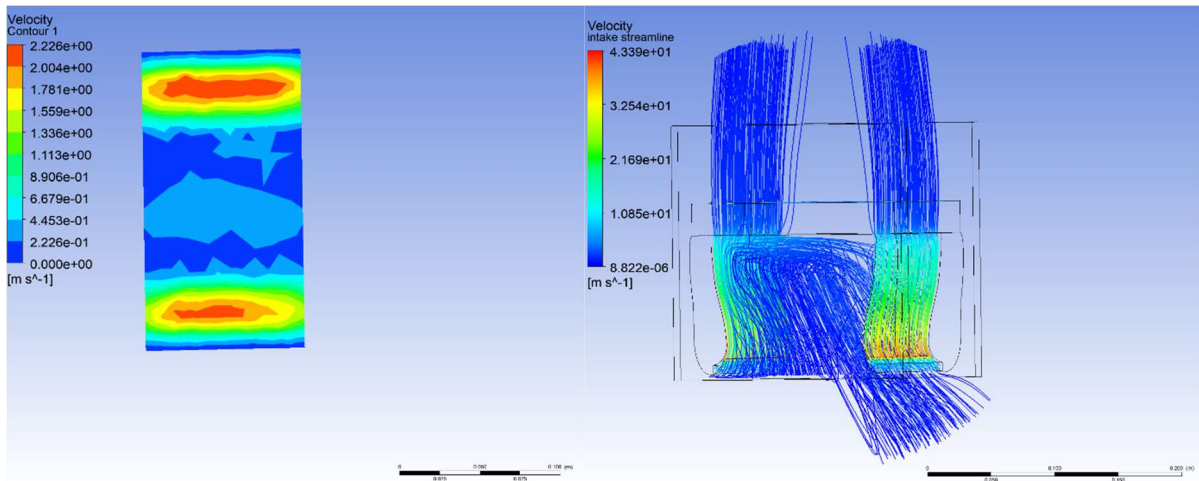


Figure 45. Separation surface delete outlet speeds and streamlines

It can be observed that the flow does form a strong current, resulting into backwards flow of air expelled out of the intake.

$$\dot{m}_{\text{surfacedelete}} = 0,015264 \text{ kg} \cdot \text{s}^{-1}$$

The decrease of mass flow through the radiator is therefore expected.

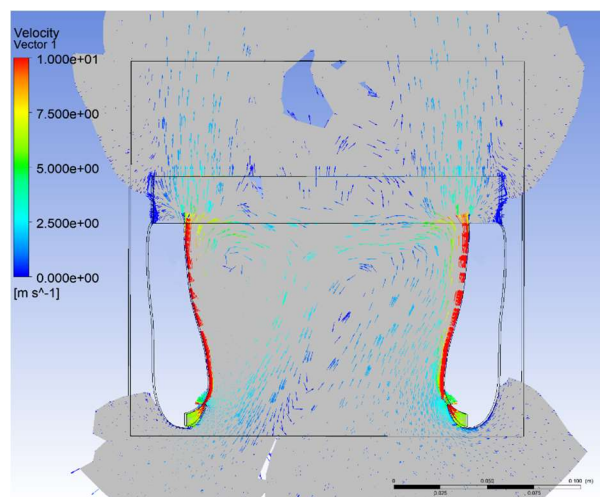


Figure 46. Separation surface delete turbulence evaluation

It can be noted that the backwards flow through the radiator is reduced, however as the air does not normalize its direction and does not spread across the surface of the radiator, it is being expelled via a pattern, described in the previous paragraph.

The conclusion of this change is that the distance between the final shape and the radiator will most likely play a big role in the resulting mass flow. The shape of the ending must be designed in a way that allows the air to approach the radiator in its normal direction.

The inlet pressure for this simulation was measured at 918 Pa.

7.3.2 PRIMARY CURVATURE

The change of the curvature was redefined by a change of parameter H89 from the original 12,5 mm to points in range of 11,25 and 13,75 mm.

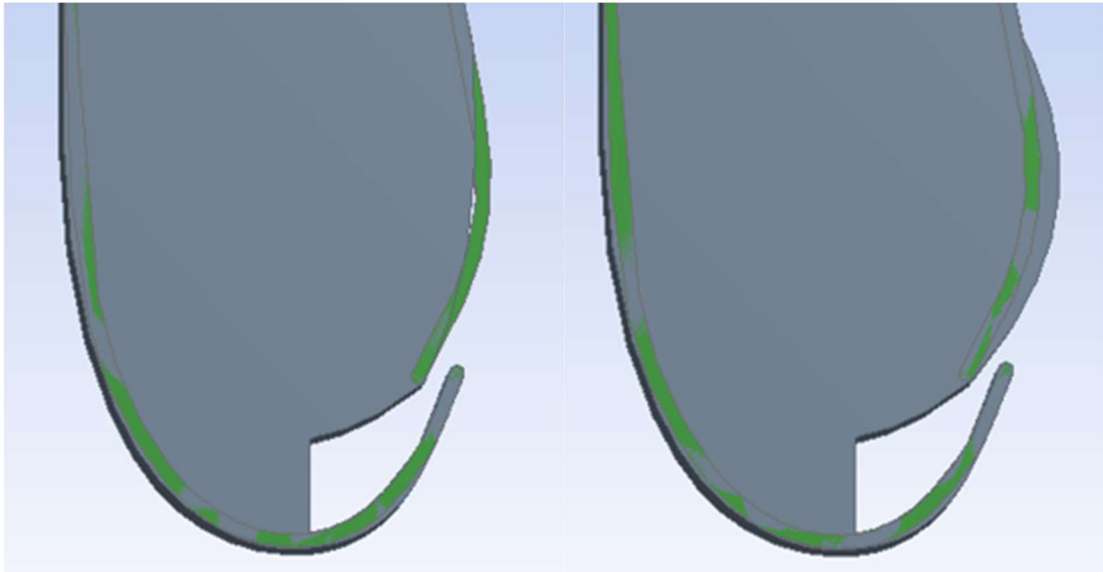


Figure 47. The primary curvature

It was observed that H89 parameter change led to a change in the channel width. This effect has a significant impact on the result and will be further inspected in the *Chapter 7.3.3*.

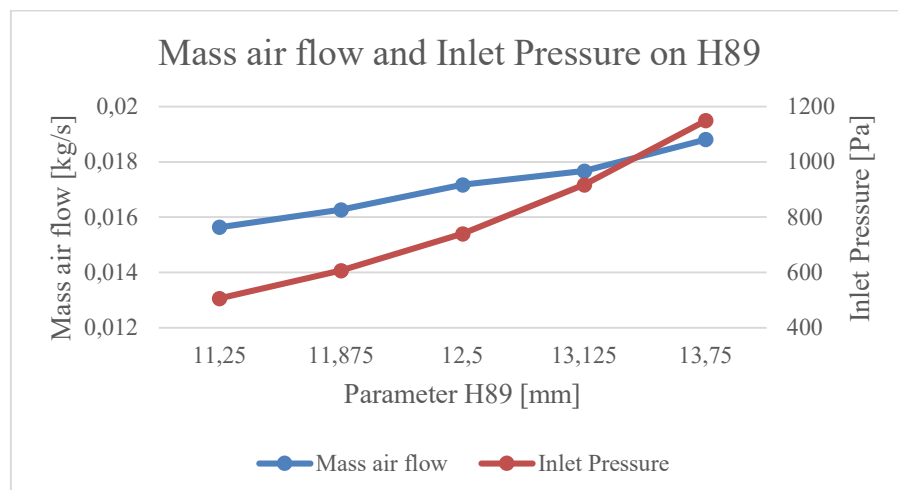


Figure 48. Mass air flow and inlet pressure dependency on parameter H89

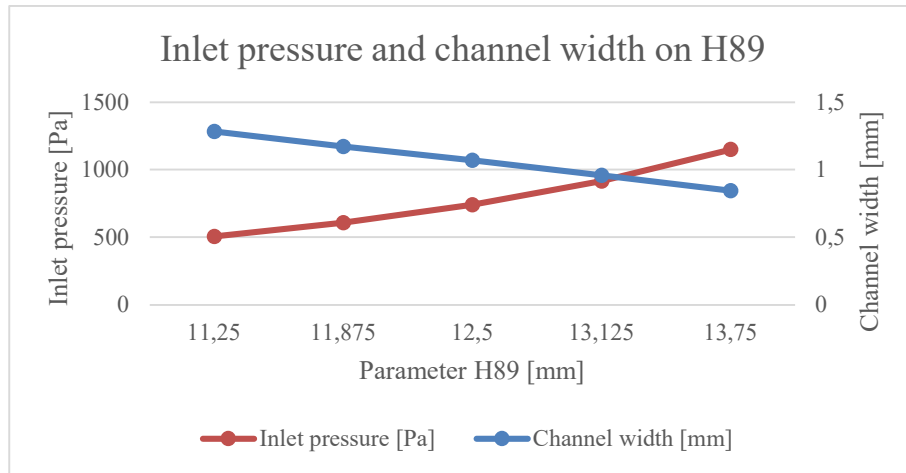


Figure 49. Inlet pressure and channel width dependency on parameter H89

The raw dataset is available in the *Attachment 21*.

As it might be identified in the *Figure 49*, the channel width correlates directly with the parameter H89. Accounting for this fact, it seems as though the primary curvature does not influence the overall mass flow through the radiator, when kept in reasonable approach angle with the inlet channel. However too sharp of an approach angle may cause the airflow to detach from the surface, hindering the Coanda effect. This is evident from the *Figure 48* at the value of $H89 = 13,125$ mm. It might also be noted that the values at 12,5 mm should match the values in the *Chapter 7.2.2*, where the same scenario is simulated. A divergency of 1,35 % for the pressure and 1,43 % for the mass air flow had been recorded.

This goes to show that identical simulation might not provide the same results due to convergency differences caused primarily by the allowed level of residual values.

In this thesis, the level of residual values was set to 10^{-4} which represents a baseline for the fastest reliably accurate calculations convergence. Had the residual target been set to lower level, this divergency would not have occurred and if yes, it would appear on a lower scale. This would however dramatically increase the calculation time, which was a concern when establishing given parameter.

7.3.3 THE CHANNEL WIDTH

The channel width had proven to have a strong correlation with the total mass airflow through radiator. It is evident from previous experiments that by narrowing the channel down, the backpressure at inlet increases rapidly. This would however put an excessive load on the inlet compressor. The power requirements for alike compressor would rise to maintain the defined mass air flow, which would dramatically increase the power draw, while increasing the overall flow only negligibly.

The channel width is modulated by the position of the centre for the ending of the channel guide. The coordinates are given by the H123 and V124 dimensions, which were assigned ranges as follows:

Table 23. Channel width parameters

	H123 [mm]	V124 [mm]
min	9,225	1
default	10,25	2
max	12	5

Using the Ansys Design of experiments tool, it was determined to calculate 17 iterations, combining both parameters alteration. The results are presented in the *Figures 50* and *51*. Iterations 7, 12, 15 and 16 resulted with a failed state caused by the gap being closed and not allowing any air flow. Therefore, results of these iterations are marked as N/A and are neglected in the graphs. The vertical red line represents the values of the real-world test subject.

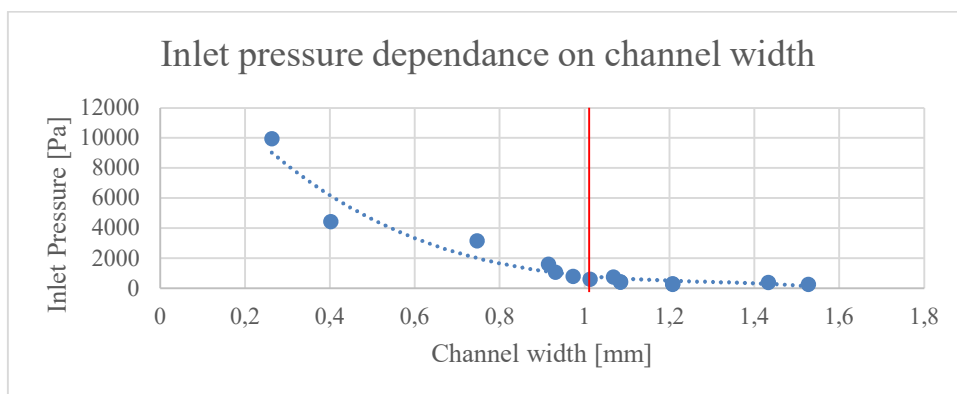


Figure 50. Inlet pressure dependence on channel width

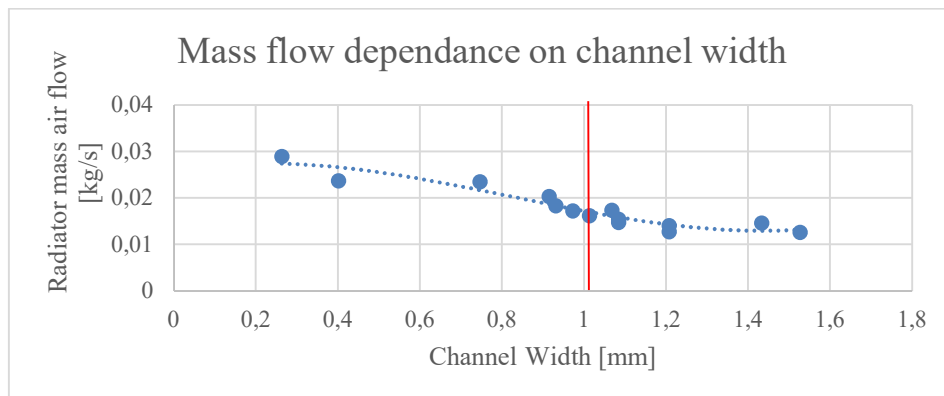


Figure 51. Mass flow dependence on channel width

It can be observed that the original channel width of 1,07 mm represents a great balance between the total mass air flow and the inlet backpressure. The optimum might however change according to a p/v (pressure/velocity) characteristic of a chosen compressor.

The detailed data for each simulation can be found in the *Attachment 22*.

7.3.4 THE SECONDARY CURVE

To variate the secondary curvature, the parameter H99 was tuned.

The default value for the parameter is 42,3 mm, while the bottom and upper boundaries were set to 38 mm and 46,5 mm respectively.

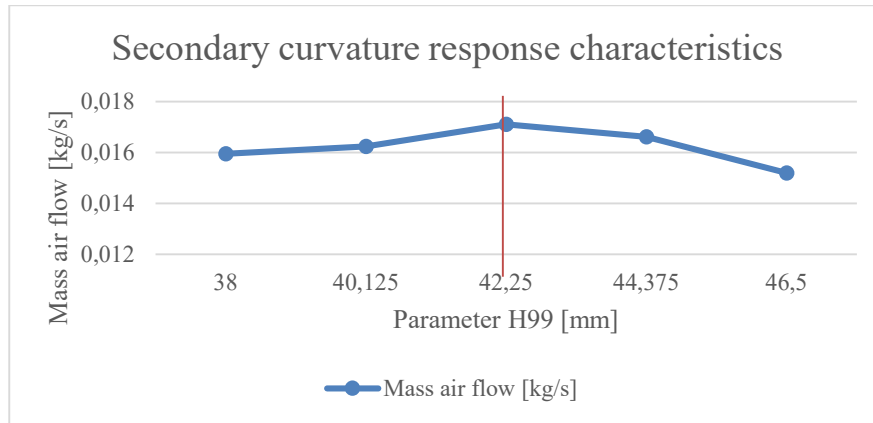


Figure 52. Secondary curvature characteristics

As it is demonstrated in the *Figure 52*, the curvature has a measurable effect on the total mass airflow, while having no effect on the inlet back pressure at all, which is expected and beneficial, since it provides a design point, which without any change in the compressor load has an impact on the total mass air flow. The default value of 42,3 mm, represented by a red vertical line, had however proven to be the optimal design, further showing that the default design of the real-world test subject had been thoroughly thought through. The detailed data for each test point can be found in the *Attachment 23*.

7.3.5 THE SEPARATION EDGE

It seems that the original separation edge is shaped in a way, that is not optimal for the use with radiator. It appears that getting rid of the relatively sharp transition improves the overall airflow through the radiator, without any impact on the inlet pressure.

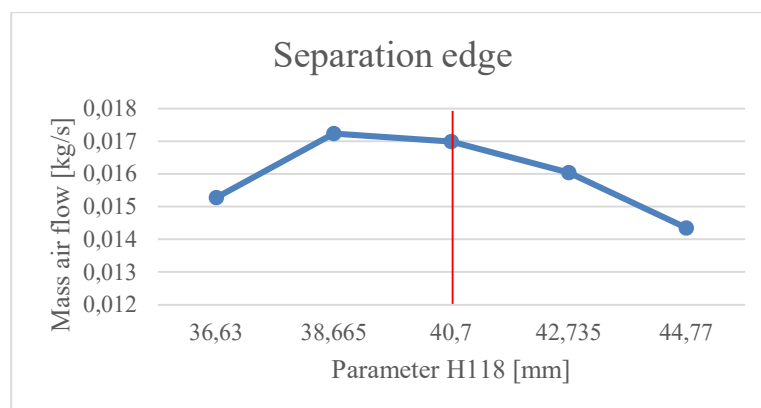


Figure 53. Separation edge characteristics

The default design is marked with a red vertical line, similarly to the previous graphs. The best mass air flow through the radiator was achieved at the parameter value of 38,665 mm.

The detailed data for each test point can be found in the *Attachment 24*.

7.3.6 PROFILE LENGTH OPTIMISATION

Based on the previous findings, the model was reconstructed to only feature the primary curve. All the other elements had been neglected. The model was gradually shortened to obtain the correlation between the profile length and mass air flow.

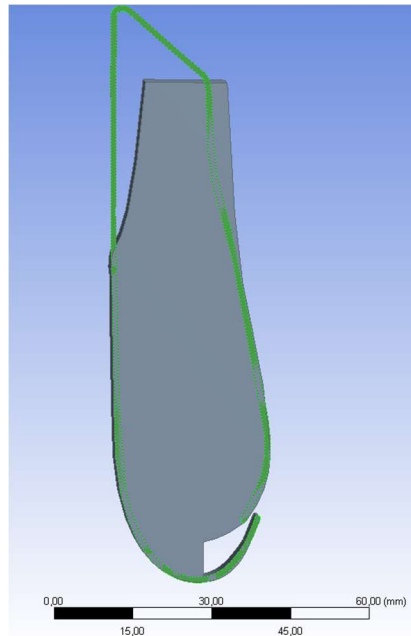


Figure 54. Shortened profile

It was observed that the mass air flow drops gradually with the profile length. This parameter must be considered in combination with the distance of the profile from the radiator, when considering the dimensions of the whole cooler module. The default value is marked with the red vertical line as in the previous cases.

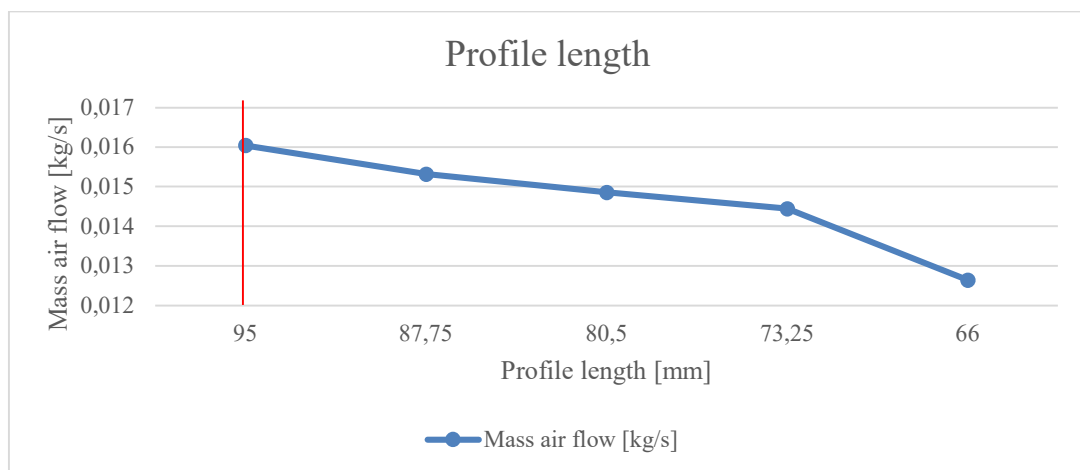


Figure 55. Profile length characteristics

The detailed data for each test point can be found in the *Attachment 25*.

7.3.7 CHAPTER CONCLUSION

Concluding findings of this chapter, aimed at individual model elements, it can be stated that:

- The distance between the radiator and the profile will most likely have an impact on the overall efficiency.
- The primary curvature does influence the width of the inlet channel in this case. It seems that the curvature itself does not play a big role in the overall efficiency, however there must not be any sudden changes of curvature present to prevent air separation from the wall.
- The channel width must be designed with the compressor's p/v characteristics in mind. However, a width slightly excessive of 1mm seems to be an optimal for the given parameters.
- The separation edge must be designed in a way, which allows the flow to direct itself in the direction of the radiator passages. If it fails to deliver this functionality, the blow-by, or in another words, air returning from the intake, will be detrimental to the overall efficiency.
- The profile length hinders the efficiency significantly when decreased bellow 73 mm. It seems that this parameter is very important, which can be demonstrated on revisiting *Chapter 7.2* – here a profile with an overall length of 408 mm provided a mass air flow through the radiator of $\dot{m}_{simMQBrad} = 0,029784 \text{ kg} \cdot \text{s}^{-1}$. Comparing it to the mass flow of a profile with a length of 73mm $\dot{m}_{sim73mm} = 0,014446 \text{ kg} \cdot \text{s}^{-1}$ a loss of 51,5% is present. Nevertheless, in the real-world application in a road going vehicle, there are not many radiator installations that would allow for a 400mm long ducting to exist. The final dimension than must be chosen wisely within given installation dimensions.

To better illustrate the concluded results, following table is provided. For every parameter, its maximum and minimum mass flow values were compared. Dividing the mass flow outlet by the mass flow inlet results in the efficiency percentage. The maximum and minimum efficiency percentage for each parameter is subtracted to create the delta. Finally, the parameter weight is calculated as the parameter delta divided by the highest delta overall.

It can be noted that radiator distance and channel width had the biggest impact on the overall performance, however these parameters are highly dependent on the installation conditions and compressor characteristics respectively.

Table 24. Individual parameter weight factor on the total efficiency

Parameter	Parameter weight	Original [mm]	Min [mm]	Max [mm]	Original eff [%]	Min eff [%]	Max eff [%]	Delta [%]
Radiator distance	0,76	N/A	0	300	191	191	327	136
Separation surface	0,13	N/A	yes	no	191	191	167	24
Primary curvature H89	0,19	13	11,3	14	191	172	206	34
Channel width	1,00	1,1	0,26	1,5	191	318	138	180
Secondary curvature H99	0,05	42	38	47	191	175	167	8
Separation edge H118	0,18	41	36,6	44	191	157	189	32
Profile length	0,29	95	66	95	191	139	191	52

7.4 PROPOSING THE OPTIMISED DESIGN

The conclusions from the previous chapter were used to propose a design, that will be further tuned. This design will be altered to simulate the real-world application of this principle. To achieve the best possible efficiency, both sides of the profile will be used as active flow surfaces.

For the purposes of this simulation, since it serves two inlet channels, inlet mass air flow was doubled to:

$$m_{dualside} = 0,0090938 \text{ kg/s}$$

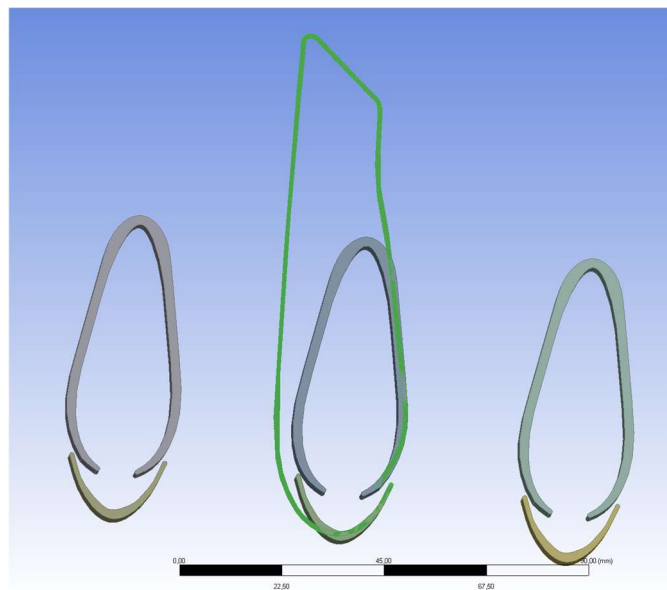


Figure 56. The optimised design proposition

The design was derived from the original shape, since it showed that it is indeed very efficient in its current form. However, the upper part was neglected altogether to form a teardrop-like shape. The primary curve and inlet characteristics were preserved.

7.4.1 DISTANCE TO THE RADIATOR

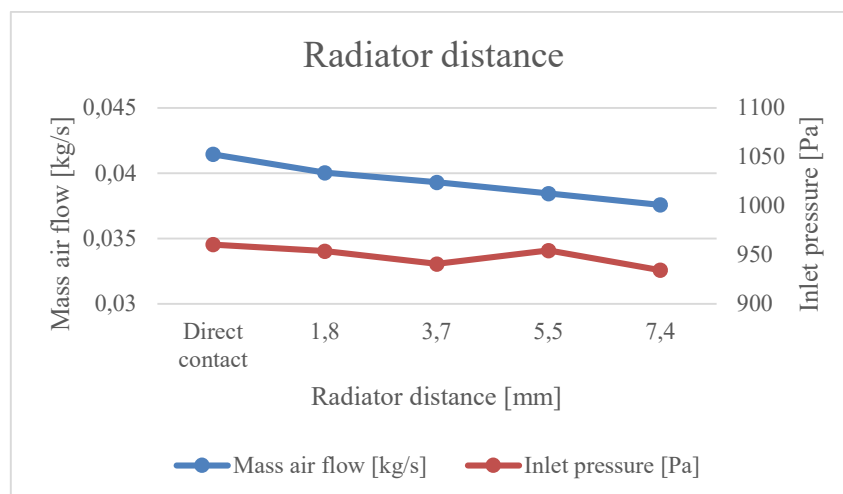


Figure 57. Radiator distance characteristics

Contrary to the single-side model conclusion, it appears that with this shape, the optimal flow is achieved upon directly contacting the profile with the radiator.

It can be observed in the *Figure 58*, that a part of the flow tends to follow the profile's edge and collides with the overflow from the other side. Probably this turbulence is the source of the efficiency decrease with bigger gap between the profile and the radiator and explains, why this effect had not been detected in single-sided model.

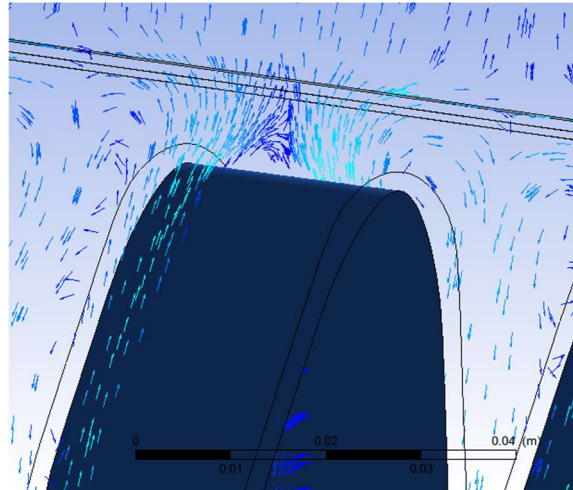


Figure 58. Profile ending detailed with velocity vectors

The detailed data for each test point can be reviewed in the *Attachment 26*.

7.4.2 THE LENGTH OF THE PROFILE

The length of the profile was varied between the values of 66,5 mm and 76,5 mm.

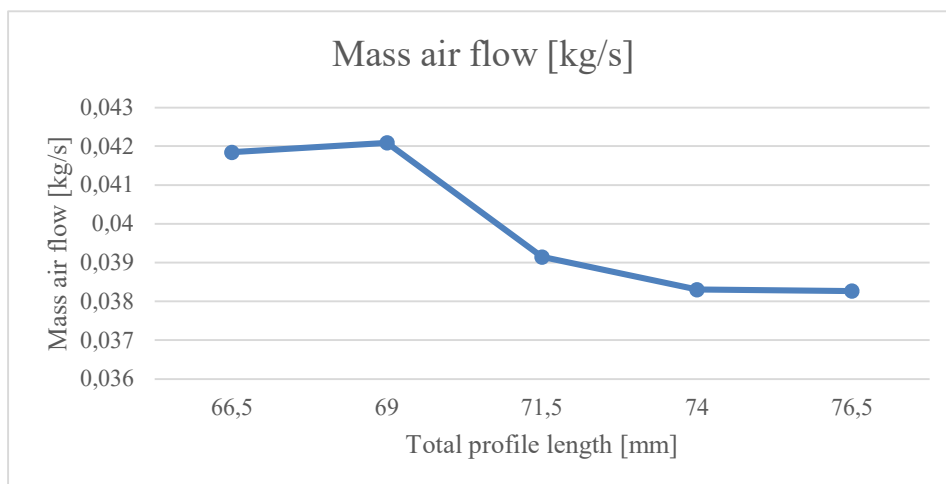


Figure 59. Mass air flow characteristics

Contrary to the original single-sided design, lengthening of the profile led to a decrease in the mass air flow, while the optimal length proved to be at 69 mm.

The detailed data for each test point can be reviewed in the *Attachment 27*.

7.4.3 THE SEPARATION CURVE AND RELATIVE DISTANCE

The curvature of separation edge proved to play an important role in ensuring the most optimal approach angle of air flow to the radiator.

Since the separation edge curvature and the relative distance of the individual profiles might strongly correlate with each other, it was decided to test them concurrently. A series of simulations was proposed to test both – wider and narrower ending of the profile, while also varying the distance between the multiple profiles.

The mirror parameter P27 is defined as the distance of midpoint axis of two neighbouring profiles. The edge curvature parameter H253 is defined as the distance of outer shell point from the profile axis in the fixed distance from the top of the profile.

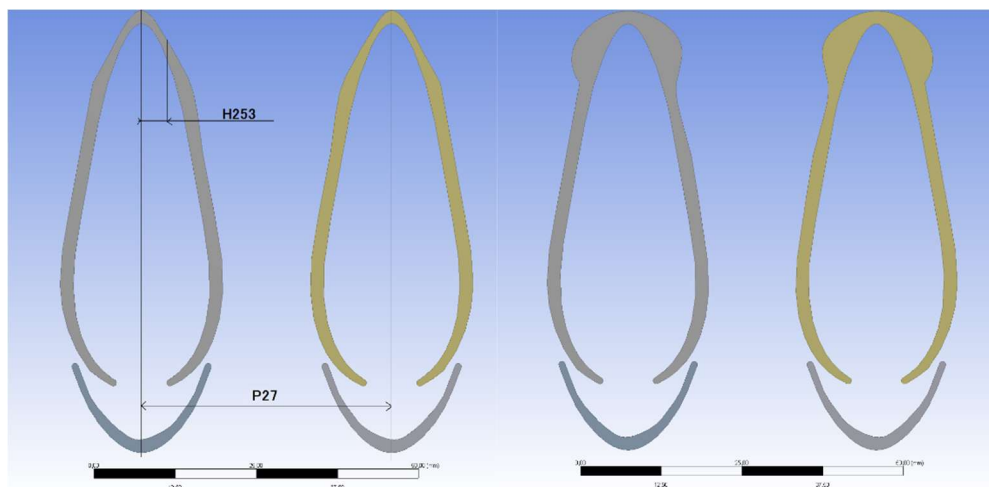


Figure 60. Edge curvature extremes for the parameter value of 4 and 8 mm respectively

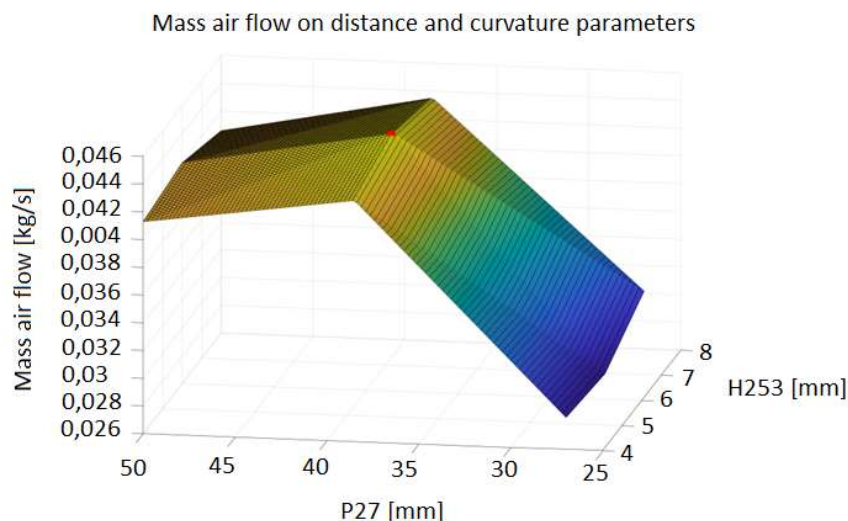


Figure 61. Separation edge curvature and profile distance impact on mass flow

The optimal operating point is marked by the red dot in the graph. It represents the value of $P27 = 38,5$ mm and $H253 = 6$ mm.

The detailed data for each test point can be reviewed in the *Attachment 28*.

FURTHER REFINEMENT OF THE SEPARATION CURVE

The previous simulation aimed at providing general awareness of the optimal operating point location. It will be further refined by simulating multiple new test points with higher resolution in its vicinity. The optimal separation curve parameter was discovered to be $H_{253} = 5,4$ mm.

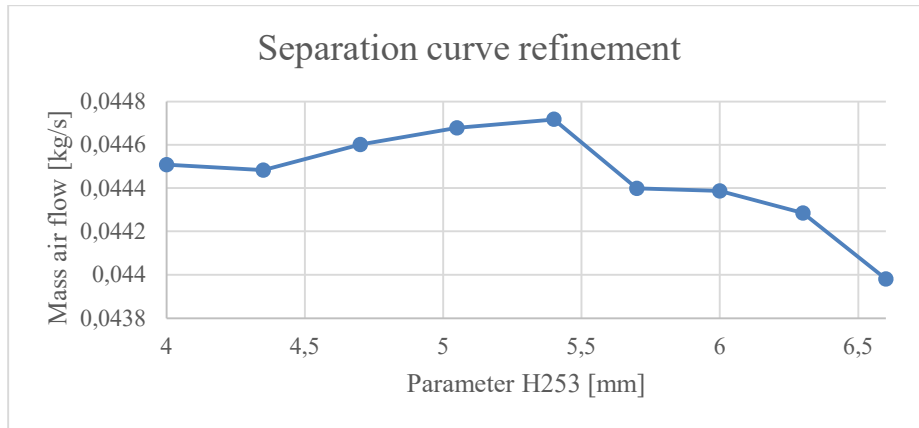


Figure 62. Separation curve refinement

Upon closer inspection, it can be concluded that the separation edge will be non-existent. It was assumed that directing the airflow to better match the radiator's passages direction would be beneficial, however it was concluded by multiple simulation results, that the profile itself serves this purpose sufficiently and introducing any other separation edges will result in decreased efficiency and thus lower mass air flow through the radiator. Also, this modification would most likely be a source of increased back pressure of the final assembly, which will be tested in the next chapter for a condition of moving vehicle.

The detailed data for each test point can be reviewed in the *Attachment 29*.

FURTHER REFINEMENT OF THE RELATIVE DISTANCE

Refinement of the relative distance was done in a similar fashion as in the previous paragraph. The default distance of 38,5 mm was extended to a range of 34,65 mm and 42,35 mm.

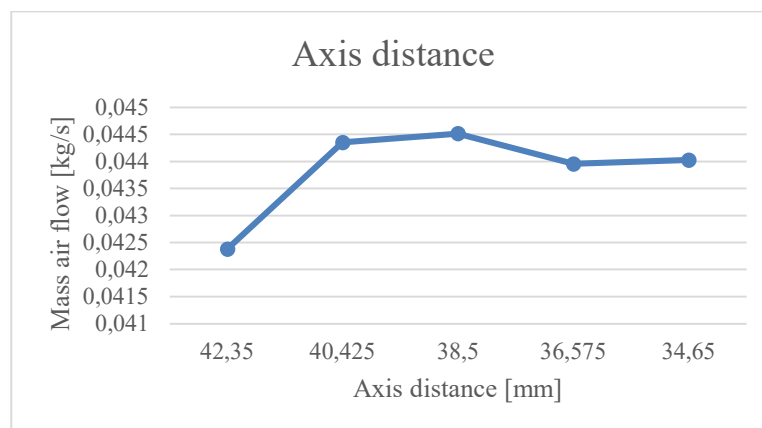


Figure 63. Axis distance refinement

It can be concluded that the optimal distance of individual profile axis is 38,5 mm.

The detailed data for each test point can be reviewed in the *Attachment 30*.

7.4.4 Conclusion and the final design presentation.

Multiple simulations were performed with a set of different inlet mass flows. The mass flow through the radiator, inlet pressure on the inner surface of the profile and total flow efficiency was monitored. The flow efficiency is defined as the mass flow from output percentage relative to the mass flow from inlet.

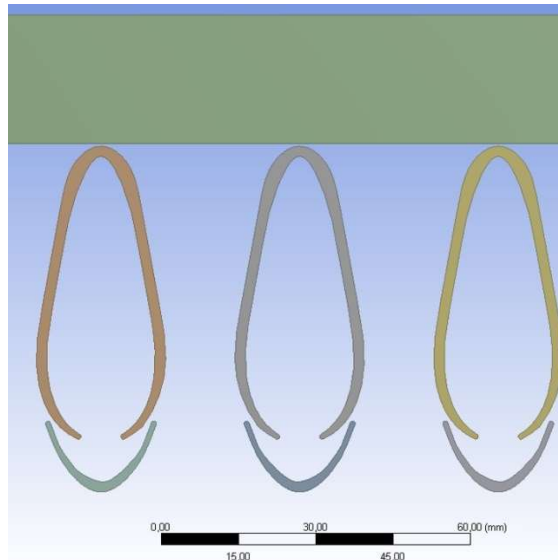


Figure 64. Final design presentation

It can be stated that the multiplication ratio tends to drop off with the increasing flow, however, is the greatest at the operational point of 1226 Pa, slightly higher, than the original 935 Pa. This can be most likely attributed to a calculation error since the efficiency trend is otherwise apparently slightly declining with the increase of mass air flow. The efficiency can be rounded to 160% across the whole spectrum— meaning that if 100 unit of mass of air is forced into the inlet under a pressure, 60 unit of mass of air is sucked in through the intake. In total, 160 units of mass of air exit the assembly through the radiator (outlet). The detailed data can be reviewed in the *Attachment 31*.

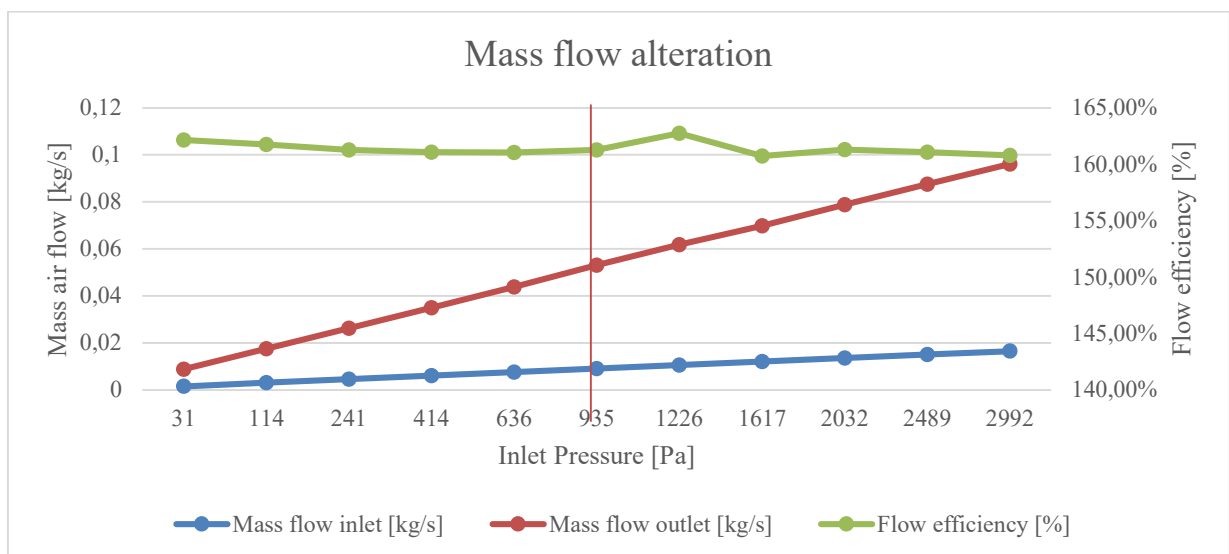


Figure 65. The final profile characteristics at steady state

8 OPERATIONAL CHARACTERISTICS

8.1 USAGE OF THE OPTIMISED PROFILE IN A MOVING VEHICLE

To assess the behaviour at a typical vehicle installation, it was decided to run a series of simulations with different conditions. The final assembly was placed into a rectangular domain. The front side of this domain was defined as an inlet at normal speed, while the opposite side of the domain was defined as an opening with 0 Pa pressure difference.

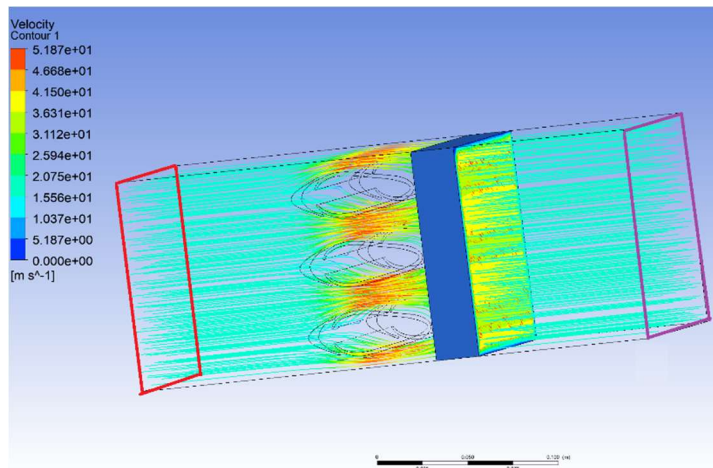


Figure 66. The final assembly in the moving vehicle test tunnel

8.1.1 MASS FLOW AT SPEED

BLADELESS FAN

The assembly was placed into a moving air at the speeds of 0 to 150 km/h to simulate the real-world driving conditions. This was achieved by inserting the assembly into a rectangular tunnel. The front side of this tunnel was set as inlet, through which the air at the defined speed is entering in normal direction to this surface. The back side was set as an opening, letting the air freely escape outside of the assembly. The contours of these boundary conditions are highlighted in the *Figure 66* by red and purple respectively.

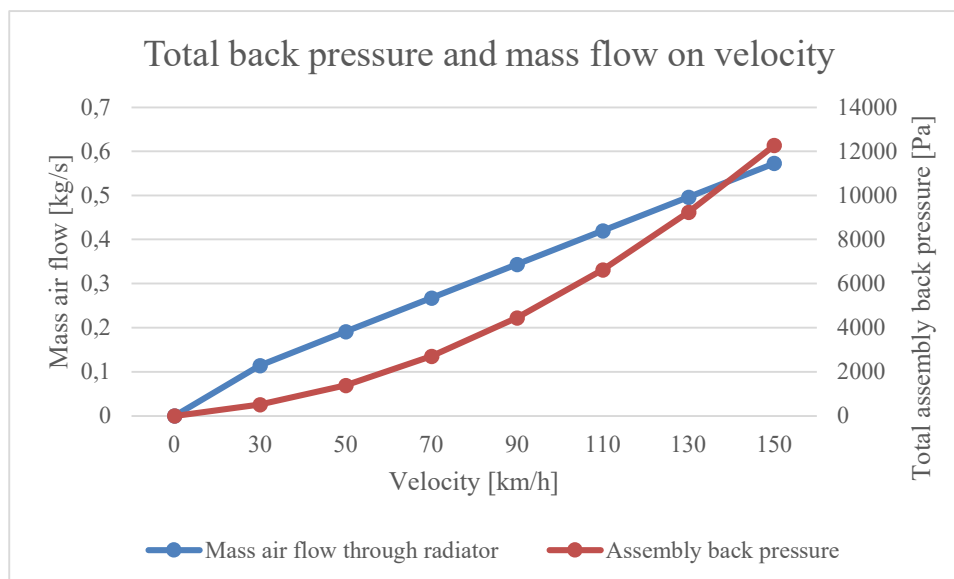


Figure 67. Assembly back pressure and mass air flow through radiator characteristics

8.1.2 MASS FLOW AT SPEED WITH INLET MASS FLOW

The assembly was tested for multiple scenarios, combining each of the vehicle speeds from the *Chapter 8.1.1* with 3 states of inlet mass air flow $\dot{m} = 0,003; 0,0090938; 0,0165$ kg/s, simulating the injection of the air into the profiles by the compressor.

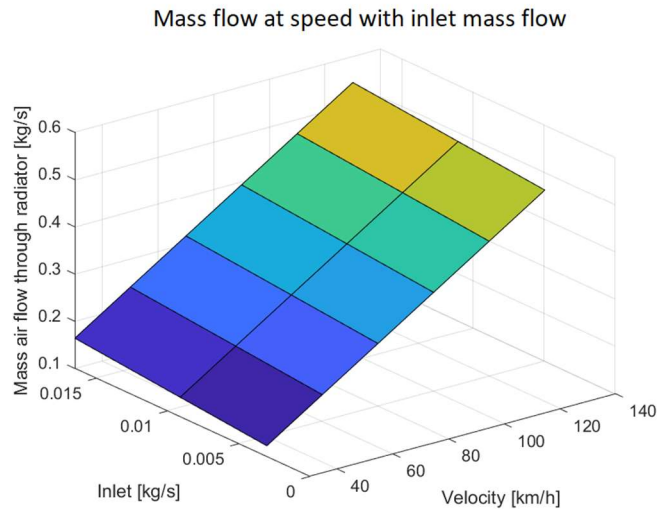


Figure 68. Mass air flow through radiator with the inlet compressor running

As it might be observed, the mass air flow along with the average velocity at radiator outlet scale proportionally with the increase of vehicle's velocity and inlet mass flow.

The obtained values from simulations can be found in the *Attachments 32* and *33*.

8.2 PRESSURE DROP EVALUATION

To obtain a comparison of the pressure behaviour of the optimised profile and the MQB assembly, it was decided to run multiple tests. The main measured parameter is pressure drop across the measurement assembly.



Figure 69. Simplified model of the MQB cooling module shroud

This assembly consists of a test tunnel, measuring 670 x 450 x 220 mm, in which the measured objects are placed. All the objects are placed in a planned position of use. The optimised profile is placed in front of the radiator, while when assessing the performance of the standard MQB assembly, the layout of fan on the back side of the radiator is used.

The MQB assembly was approximated by a very simple model, which replicated the shroud as depicted in the *Figure 69*. The fan blades and flaps in the rectangular passthroughs were neglected. Due to this simplification, the real-life back pressure will be even higher for the MQB assembly than in this evaluation.

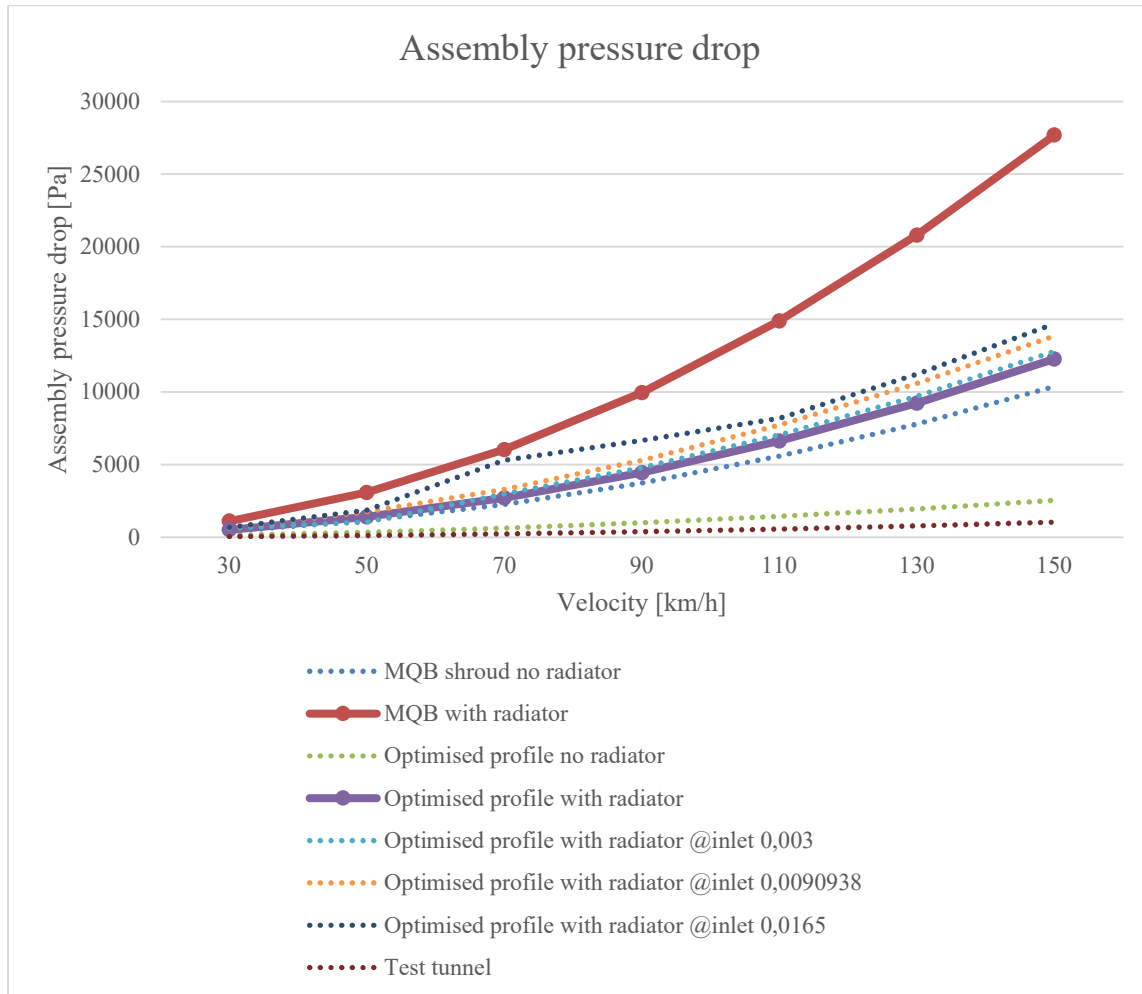


Figure 70. Assembly pressure drop for multiple devices

9 VERIFICATION

To further confirm the simulation results, it was decided to conduct a series of experiments with the final design.

The final profile as well as the original profile were remanufactured using SLS 3D printing. SLS stands for selective laser sintering. This method can produce a very smooth surfaces in contrast to traditional FDM (Fused Deposition Modelling).

To provide the needed air flow, it was decided to use a distribution system of central pressurised air at the measuring facility.

9.1 TESTING METHODOLOGY

Since the optimised shape will be manufactured with the SLS 3D printing technology, it was deemed important to also re-test the default profile. Even though, the SLS 3D printing produces relatively smooth surfaces, an evident texture is present on the manufactured surface. This texture might have a negative impact on the operational characteristics of a model, manufactured in this way.

A construction was proposed that allows attachment of the Radiator B to the manufactured profiles and provides variability of the profile placement in longitudinal axis to vary the distance between the individual profiles.

To measure the pressure in the system and regulate the volumetric flow, a valve with pressure gauge SMC IR2020-F02 was used.

To measure the volumetric flow, a flow-meter CS Instruments VA520 was used.

For both experiments a relative inlet pressure was set to:

$$p_{in} = 0,2 \text{ MPa}$$

This resulted in a volumetric flow at inlet of:

$$\dot{V} = 800 \text{ l/min} = 0,8 \text{ m}^3/\text{min} = 0,01333 \text{ m}^3/\text{s}$$

Since the air is found in multiple pressure states with possibly different humidity, as the inlet is supplied from a compressor, located in another part of the building, while the intake can suck the air from the room of experiment, it was decided not to evaluate the mass air flow. Instead, it was decided to calculate a volumetric coefficient, comparing the inlet and outlet measured volumetric flow. The individual experiments are corrected by varying the inlet pressure to provide the same volumetric flow of 800 l/min.

$$C = \frac{\dot{V}_{outlet}}{\dot{V}_{inlet}} \cdot 100 \quad (18)$$

This coefficient depicts the overall efficiency of the bladeless fan. If a value greater than 100 % is achieved, some air is sucked in through the intake which is considered beneficial. This coefficient is also directly proportional if calculated using mass air flow from the simulations.

9.2 DEFAULT SHAPE REMANUFACTURED MEASUREMENT

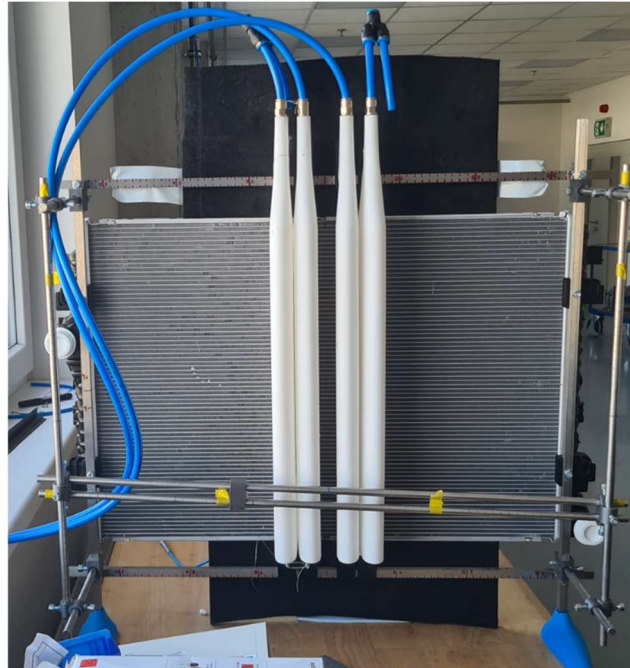


Figure 71. Remanufactured base profile testing apparatus

To connect the default profile to the pressurised air system, it was decided to build-in a cone at the end of the profile, which would allow for installation of a fitting. The measuring apparatus is depicted in the *Figure 71*. This figure serves as a reference, the final measurement was done on two profiles with the same distance as the stock implementation – 160 mm. The intake tubes were wired from the bottom.

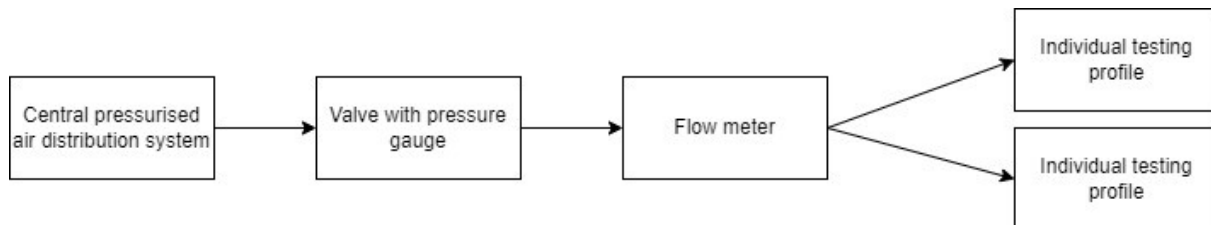


Figure 72. Air distribution chart

As it can be seen in the *Table 25* below, the pressure drop throughout the length of the profile is extreme and brings a lot of distortion to the results. The inner design of the profile to evenly distribute the air across its length needs to be improved for the next measurement.

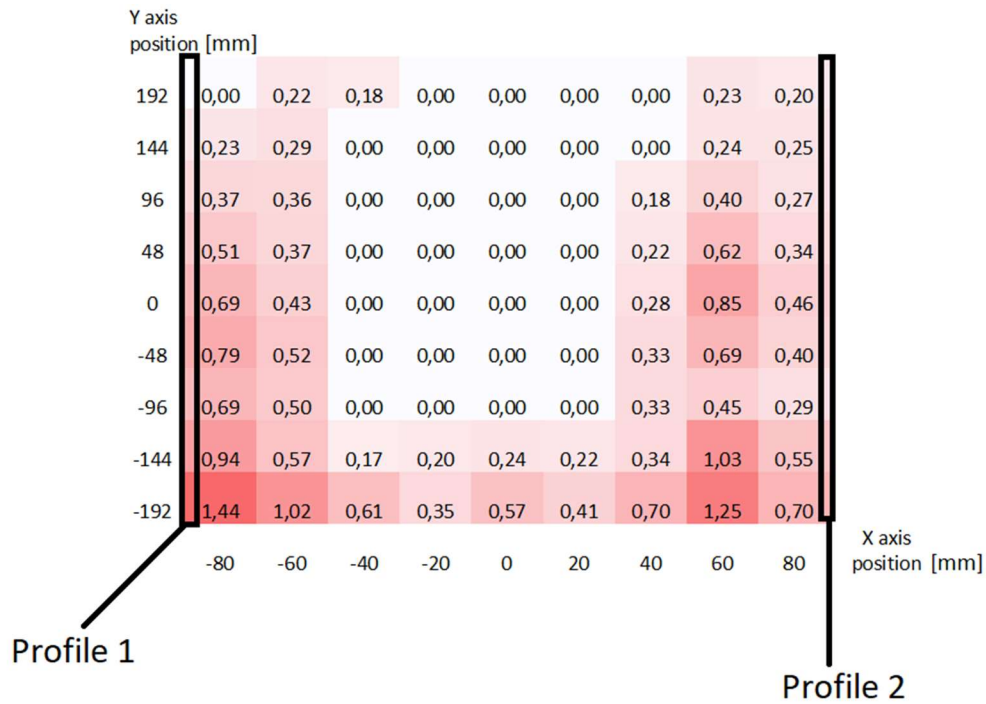
The total volumetric flow can be determined as:

$$V_{\text{def_reman}} = 0,018551 \text{ m}^3/\text{s}$$

Using the equation described in previous chapter a coefficient of efficiency is calculated as:

$$c_{\text{def_reman}} = 139,5\%$$

Table 25. Remanufactured original profile measurement on MQB radiator, velocity [m/s]



It was decided to conduct the same experiment with the original device. The device was mounted to the radiator in the same way and was measured as follows:

Table 26. Original test subject on the MQB radiator, velocity [m/s]



Here, the original base was used, providing a volumetric flow of:

$$V_{\text{original_base_in}} = 0,058434 \text{ m}^3/\text{s}$$

The outlet volumetric flow was measured as:

$$V_{\text{original_device}} = 0,126485 \text{ m}^3/\text{s}$$

The surface area was used as referenced in the Chapter 6.1.4.

The coefficient of efficiency can be calculated as:

$$C_{\text{original_device}} = 216,5\%$$

Comparing the two coefficients $C_{\text{original_device}} = 216,5 \%$ and $C_{\text{def_reman}} = 139,5 \%$, it is evident that the testing apparatus is incapable of providing the same efficiency. The main cause can be determined by comparing the inlet pressures. While the original device was measured in the simulation to have a back pressure of 850 Pa, on the remanufactured profile a pressure orders of magnitude higher is applied to the tubing to sustain the required volumetric flow.

The low-diameter tubing, that is used to deliver the air from the pressurised air distribution system to the profiles is highly restrictive at this high flow rate level. Also, the distribution of the air flow across the length of the profile is extremely poor.

It ought to be noted that another two deficiencies of this design were spotted during testing. The channel where air leaves the profile was left completely hollow, which led to a vibration, since the material was not as rigid as expected. This was mostly solved by inserting multiple drops of hot glue into the channel along the length of the profile acting as a support.

Another deficiency was a noise profile of the whole device. It proved to be unbearably noisy and requiring hearing protection during testing. It is believed that the source of this noise is the air expanding from the low-diameter tubing upon entering the profile, however the final assembly will be subject to a noise evaluation test in the next chapter to confirm this theory.

Unfortunately, remanufacturing of the profile is not financially viable, since SLS 3D printing on this scale has a high cost of production, the gained knowledge will however be used in designing and manufacturing the final optimised design.

9.3 OPTIMISED SHAPE MEASUREMENT

To evaluate the optimised design, the knowledge gained in the previous chapter was applied. It was decided to only optimise the internal design with a goal of homogenising the air flow across the length of the profile. The rest of the testing apparatus remained the same to provide at least some possibility of comparing the results.

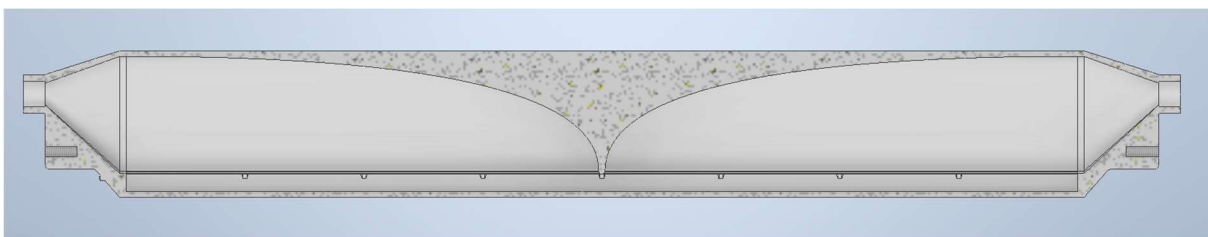


Figure 73. The optimised shape inner chamber shape

As depicted in the *Figure 73* above, the profile was separated into two compartments. Each of these compartments has its own inlet to minimise the distance, the air must travel inside the profile. Simultaneously a gradual taper was incorporated into the compartment's design to further help with the air flow distribution. Finally, multiple supports were added to compensate for the lack of the material rigidity and avoid vibrations.

It was decided to manufacture 3 identical profiles that will respect the optimised design. The two outer profiles will have one of their channels – facing outwards – blocked by a tape. To distribute the air evenly, it was decided to use the following setup of the measuring apparatus.

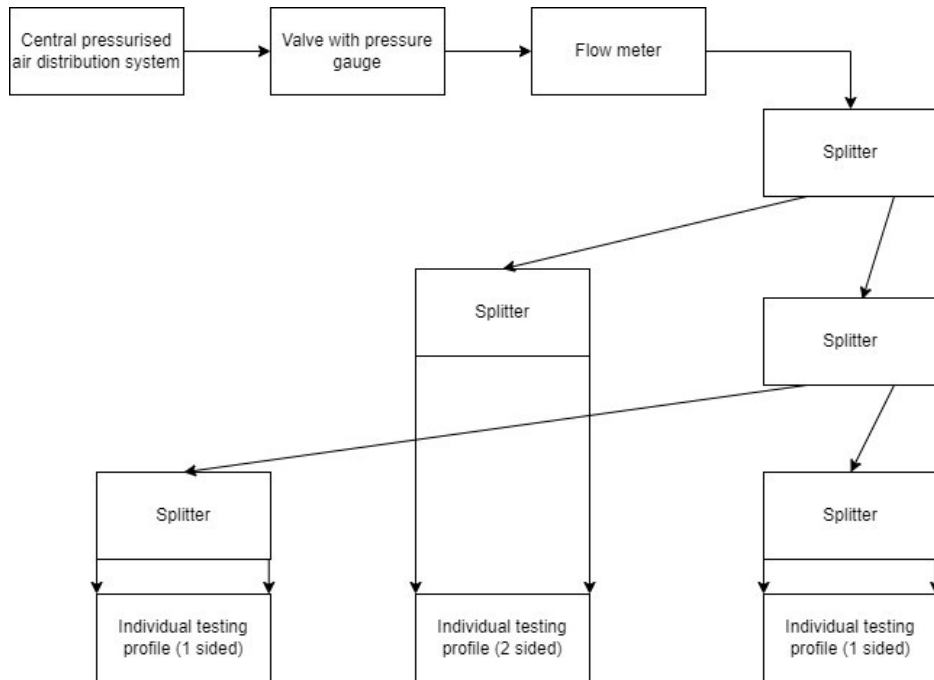


Figure 74. Air distribution chart

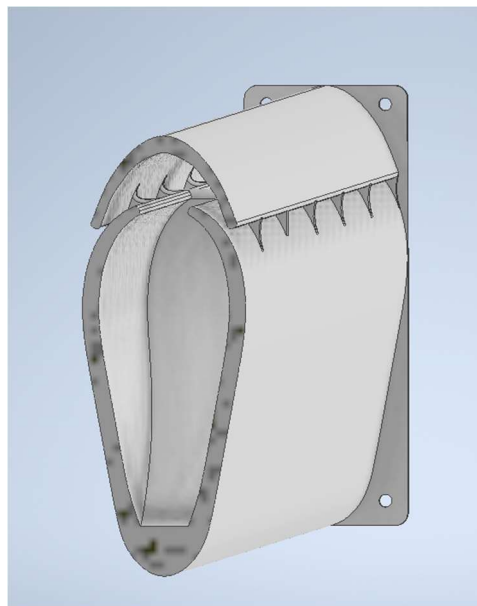


Figure 75. Profile cross section

The profiles were positioned in a way that their midpoints would be 38,5 mm distant to achieve optimal results as described in the final optimised design.

The experiment was divided into 4 parts. Since the source of air pressure did not enable for high enough airflow to test higher speeds, it was decided that after the first base-line measurement a part of the channel will be covered with a tape to decrease the total length of the profile, which will lead to an increase in the air speed, while retaining the same volumetric flow.

Table 27. Individual measurements data

Y position	Mea1						
3	1,07	0,97	1,28	0,85	1,01	Length [mm]	440
2	0,93	0,91	1,05	0,77	1,04	Inlet volumetric flow [m ³ /s]	0,013333
1	1,04	0,93	0,89	0,87	0,99	Outlet volumetric flow [m ³ /s]	0,031263
	1	2	3	4	5	Average velocity through rad [m/s]	0,973333
	Mea2						
3	2,91	2,92	2,37	2,81	2,86	Length [mm]	133
2	2,55	2,45	2,01	2,51	2,39	Inlet volumetric flow [m ³ /s]	0,013333
1	2,85	2,67	1,83	2,31	2,41	Outlet volumetric flow [m ³ /s]	0,024867
	1	2	3	4	5	Average velocity through rad [m/s]	2,523333
	Mea3						
3	3,71	3,65	3,91			Length [mm]	88
2	3,17	2,96	3,07			Inlet volumetric flow [m ³ /s]	0,013333
1	3,24	3,31	3,09			Outlet volumetric flow [m ³ /s]	0,021492
	1	2	3			Average velocity through rad [m/s]	3,345556
	Mea4						
1		5,59				Length [mm]	52
2		4,24				Inlet volumetric flow [m ³ /s]	0,013333
3		4,47				Outlet volumetric flow [m ³ /s]	0,018094
X position	1	2	3			Average velocity through rad [m/s]	4,766667

- The red horizontal line represents the simulation results.
- The vertical, red line represents the operating point in accordance with the original design.

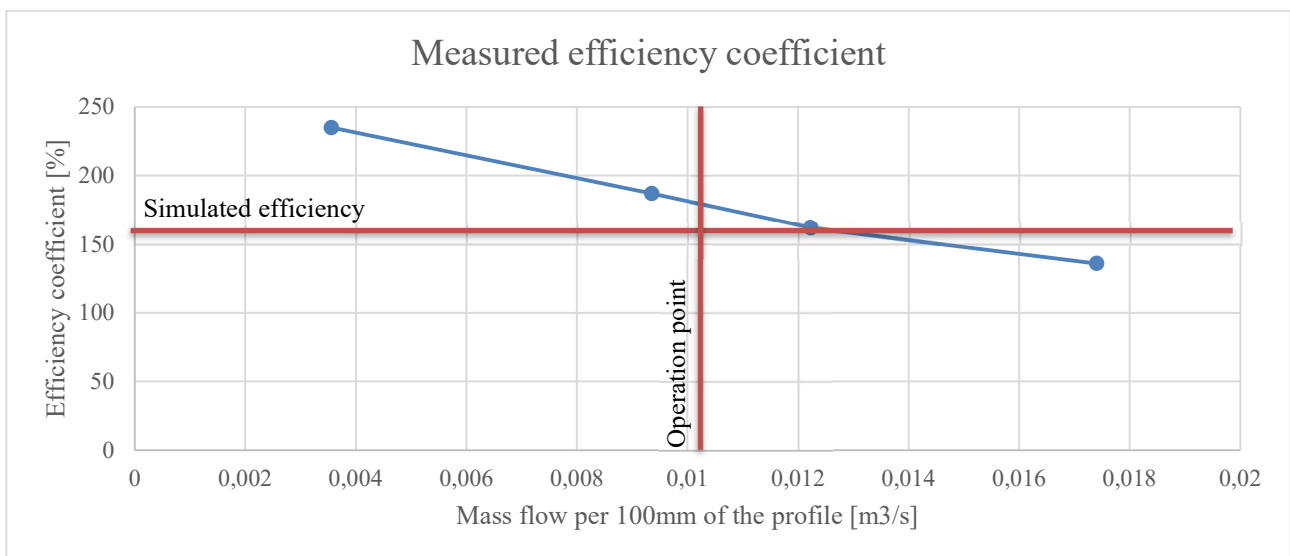


Figure 76. The efficiency coefficient

Picture of the testing apparatus along with the raw measurement data can be found in the Attachments 34 and 35.

It can be observed that the overall efficiency is close to the simulation results. Even though, the simulation projected very linear efficiency with growing mass flow and speeds. Here it can be observed that the efficiency drops with higher mass flow and speed, however is greater than expected in the lower parts of the operating range. The average measured value is:

$$C_{\text{opti_measured}} = 180 \%$$

While the average simulated value is:

$$C_{\text{opti_simulated}} = 161\%$$

Thus only 11,8 % divergence was achieved, which means, the measurement can be considered accurate.

9.4 NOISE CHARACTERISTICS

To analyse the sources and the potential level of noise of the profile an additional simulation was carried out in the Ansys Fluent application, which is more suitable for noise analysis than Ansys CFX. The analysis was performed via the Williams and Hawkings model.

The problem was simplified into a 2D cross-section of the profile, while the sound pressure level was measured by two probes, positioned as depicted in the *Figure 77* in the distance of 1 m from the middle of the test subject.

It was chosen to perform this simulation for the highest considered mass air flow through the profile of:

$$\dot{m}_{\text{max}} = 0,0165 \text{ kg/s}$$

per 100 mm length of the profile. For the purpose of the 2D model, this had to be entered as a pressure source of 3000 Pa, which coincides with the pressure at inlet inside the 3D situation for this massflow.

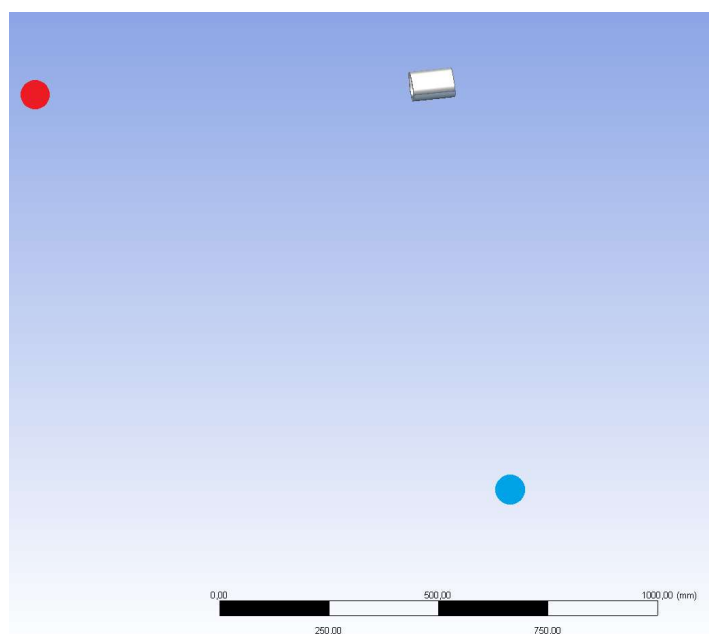


Figure 77. Illustrative positioning of the noise sensing probes

The simulation was performed as transient, to cover any fluctuation in the flow. The measurement spectrum was set in accordance with the frequency spectrum, that can possibly be perceived by a human being, which is commonly referred to have a range of 20 Hz to 20kHz.

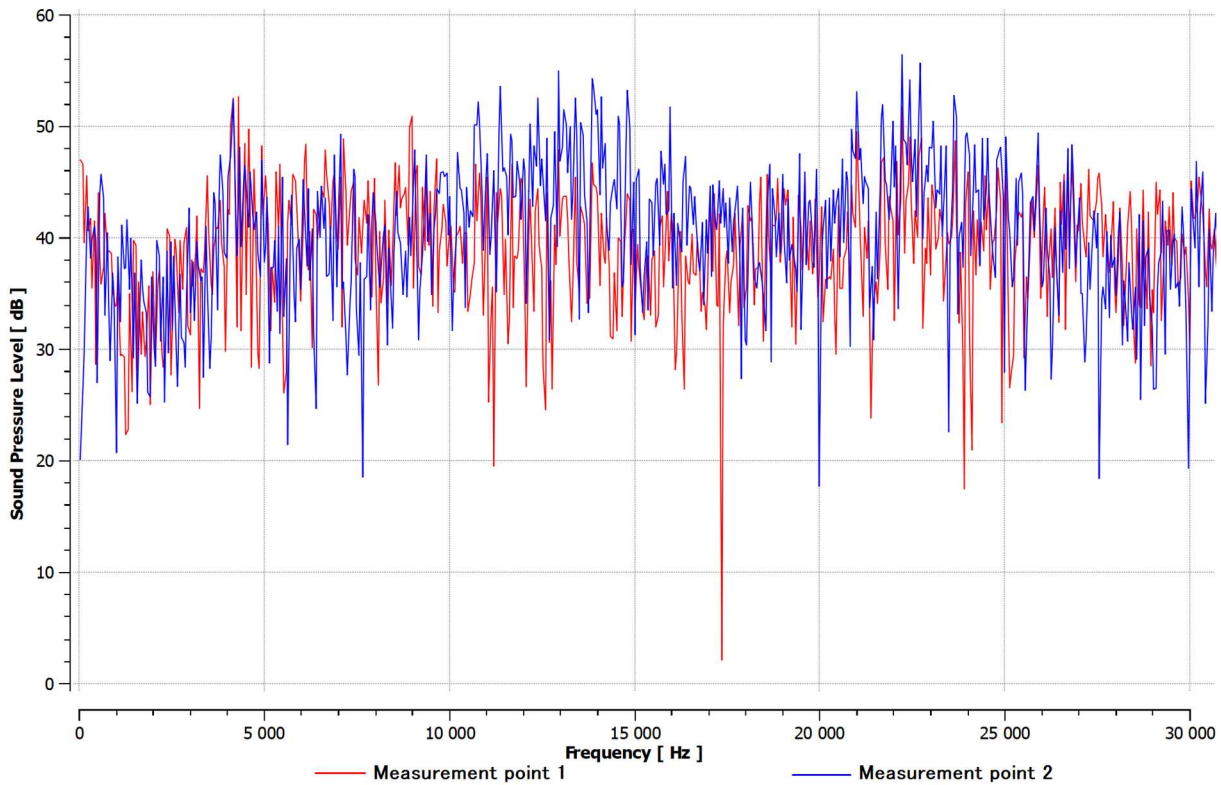


Figure 78. Sound Pressure Level at measurement points

The maximum amplitude can be found at 55 dB, which is an acceptable value. Unfortunately, the main body of this amplitude can be found within the range between 10 and 15 kHz, which is a high-pitch noise, that can be found irritating. Also, the blue measurement point in front of the profile is showing higher amplitude, than the red measurement point, placed next to the profile – which is expected.

In conclusion than, it can be stated, that the source of the extreme noise when testing the profiles was most likely the air, expanding upon exiting the narrow tubing.

10 CONCLUSION

This thesis aimed at exploring the possibilities of bladeless fan designs use on a traditional air-coolant heat exchanger. The Dyson AM-07 device was chosen as the baseline and was measured to provide approximately 645% air flow efficiency, meaning that when a mass flow of air at 0,0692 kg/s was provided at a pressure of 850 Pa into its inlet, mass flow of 0,4468 kg/s exited from its outlet.

When however, the radiator was installed on the fan along with a 300mm ducting, the efficiency dropped significantly.

The device was than scanned by a scanner to obtain a 3D model, while its compressor was measured for mass air flow, to establish boundary conditions for the simulation.

This model along with boundary conditions was tested in the Ansys CFX application and used as a calibration of the virtual environment to correspond to the real world. During this calibration, it was found that the intake side of the fan experiences notable air-wall interactions, which make the real-world measurement of the intake side impossible with the available measuring equipment - anemometer. However, given the multiple datapoints acquired from measuring the base and outlet, it was possible to establish a conclusive explanation and prove that the model is accurate within a 13% deviation from the real-world measurements.

In a similar way, the parametrisation of the heat exchanger was performed. It was chosen to use an existing assembly for the MQB platform as a baseline for all simulations. The radiator was defined by setting up its loss coefficient, directionality, and transverse losses. It was found that the model is accurate with approximately 10 % deviation from the real-world measurements in the speeds, that are relevant for the application.

The original 3D model was expressed by a parametric model in Ansys design modeller, that was then used to examine the effects of individual characteristic elements of the profile on its behaviour. It was found out that the width of the channel, through which the air exits the profile is a very important parameter, that must be optimised for a p/v characteristic of a chosen compressor. It plays a big role in determining the overall pressure loss, while also contributing to the Coanda effect efficiency. Other than that, the distance between the end of the profile and the radiator along with the profiles length also play a big role in the overall efficiency. These are however limited by the available installation dimensions, which are quite limited for a use in a passenger vehicle. Based on these findings, the optimised profile was proposed.

The optimised profile was designed to respect the installation dimensions of the MQB fan and radiator assembly. Thus, it was shortened from 110 mm of the original profile to only a 66 mm in height. The result was than examined in a similar way to define its behaviour based on its shape. It was found out, that the original profile was shaped in an efficient way, and there seems to not be much room for further improvements of the shape itself. The basics however stay the same - the main point of optimisation will be the exit channel width in accordance with the compressor characteristics.

To back the findings up, it was decided to prove the simulation results against a real-world experiment once more. For these purposes, the optimised as well as the original profile were remanufactured, to account for any inaccuracies, that may come from the manufacturing process, as for example the surface smoothness and texture.

In case of the remanufacturing of the original profile, it was found that the proposed model for the remanufacturing had a lot of oversights, such as poor internal air distribution layout, no bracing to ensure the stability of the channel thickness etc. These resulted in an inferior performance, however even with these problems, the device still managed to provide 140% efficiency, meaning the outlet mass air flow is 40 % higher, than the air flow that is provided into the inlet. It was then decided to use the default AM-07 device on the same testing apparatus to provide a measurement, not distorted by a poor design, which resulted in an efficiency of 217 %. For context, the Ansys CFX simulation of this setup resulted to 192 % efficiency.

When designing and manufacturing the optimised profile, the findings from the remanufacturing of the original profile shape were taken into consideration and were improved upon. The resulting profile was then tested in the same way and proved to have an excellent air distribution across its length. For the operational point at which all the simulations were performed – mass flow across one side of the profile for a length of 100 mm equals 0,0045469 kg/s – the real-world measurement of the optimised profile resulted in an efficiency of 180 %, while the simulated efficiency was 161 %. It can be concluded then, that the simulation was accurate with a deviation of 12-13 %.

During the real-world testing and measurements, it was found that the assembly is extremely noisy. So noisy in fact, that hearing protection had to be used when performing the measurements. The hypothesis for the origin of this noise was the point at which the air is rapidly expanding inside the profile upon exiting a narrow hose, used for air supply. This was proven by a simulation in Ansys Fluent, which researched the noise characteristics of the profile itself. It was found that at the maximum mass air flows, researched in this thesis – 0,00825 kg/s per 100 mm of the profile per one side – the sound pressure level at 1 m distance from the profile peaked at 55 dB. Unfortunately, the peak can be found in the frequency range of 10 to 15 kHz, which can be considered an unpleasant frequency for a human being.

To provide some scope of the requirements for the compressor/fan, that can be used as a source of the air pressure for the final assembly, it was decided to use the p/v curve of the MQB platform axial fan and calculate its suitability for this design, even though in reality, it would be highly impractical due to its size. The axial fan was able to provide a flow of 0,05 kg/s at a pressure of 641 Pa with an electric power of 1000W. This would provide sufficient flow for 5,5 sections of 100mm profile – so in total for a 0,55 m of the double-sided profile at an expected average speed through radiator at 1,7 m/s. To cover the whole MQB platform radiator, 8,6 meters of the profile is needed. This design is then unusable for the final assembly and the use of radial compressor as a source of pressurised air is recommended.

The optimal compressor that would be able to closely match the original MQB assembly performance would be required to provide 0,774 kg/s of mass flow at a pressure of 950 Pa. This however does not account for any losses that will occur in the distribution ducting, that will deliver the air from the compressor to the individual profiles. Its design was however not a subject of investigation of this thesis.

In conclusion, the use of the bladeless cooling module seems to be possible and is considered a viable option to improve the aerodynamics of the engine bay as well as to incorporate heat exchangers into atypically shaped compartments, it however does not come without its own problems such as noise, design complexity and most likely the production cost.

SOURCES

- [1] Skoda official configurator, [online]. [Accessed 10 December 2022]. Retrieved from: <https://cc.skoda-auto.com/cze/cs-CZ/summary-scenic?activePage=summary&color=K4K4&configurationId=C8ZTU1WH&extraEquipments=&id=CZE%3Bskoda%3B2023%3BNX32N5%3B1%3BGW6UW6U%5CGYOKYOK%3Bmda20230406012132%3BcsCZ%3B%3B63005%3B63025&interior=BG&modifiedPages=trimlines%7CEngines&snapshotVersion=8d025fdb-22b4-454f-a51b-16b8228899b4&trimline=NX2%7CActive6302563005&visitedPages=trimlines%7CEngines>
- [2] Model 3 Owner's Manual, *Tesla.com* [online]. [Accessed 10 December 2022]. Retrieved from: https://www.tesla.com/ownersmanual/model3/en_cn/GUID-56562137-FC31-4110-A13C-9A9FC6657BF0.html
- [3] VLK, František, 2000. *Dynamika motorových vozidel: jízdní odpory : hnací charakteristika : brzdění : odpruženost : říditelnost, ovladatelnost : stabilita*. Brno: VLK. ISBN 80-238-5273-6.
- [4] Skoda Octavia Design, [online]. [Accessed 7 December 2022]. Retrieved from: <https://www.skoda.ie/models/octavia/octavia/octavia-design>
- [5] The Tesla Model 3, reviewed (finally), *Arstechnica* [online]. [Accessed 12 December 2022]. Retrieved from: <https://arstechnica.com/cars/2019/03/the-tesla-model-3-reviewed-finally/>
- [6] Rozměry Škoda Octavia, *Octaviaclub.cz* [online]. [Accessed 11 December 2022]. Retrieved from: <https://octaviaclub.cz/octavia-4/rozmery-objem-kufru/#prettyPhoto/1/>
- [7] The Most Efficient 4-Wheel Car Ever Made — Part 2, *Cleantechnica* [online]. [Accessed 13 December 2022]. Retrieved from: <https://cleantechnica.com/2023/01/23/the-most-efficient-4-wheel-car-ever-made-part-2/>
- [8] Cooling systems, *Bhecc.com* [online]. [Accessed 14 December 2022]. Retrieved from: <https://bhecc.com.au/cooling-systems/>
- [9] ROMAGNOLI, Alessandro, RICARDO, Martinez-Botas, PESYRIDIS, Apostolos, RAJOO, Srithar, COPELAND, Colin and IHSAN BIN MAMAT, Aman Mohd, 2014. *Automotive Exhaust Waste Heat Recovery Technologies*. NOVA Science Publishers. ISBN 978-1-63321-493-4.

- [10] Product Specifications Document No: 50/352, [online]. [Accessed 20 December 2022]. Retrieved from: <https://robu.in/wp-content/uploads/2022/09/AMS-NMC-21700-5000mAh-3c-Lithium-Ion-Battery.pdf>
- [11] How Fast Does A 2021 Tesla Model 3 Charge? We Find Out, *Insideevs.com* [online]. [Accessed 7 January 2023]. Retrieved from: <https://insideevs.com/news/506520/tesla-model-3-supercharger-test/>
- [12] ROBINS, Benjamin, 1742. *New Principles of Gunnery*. [Accessed 10 January 2023]. Retrieved from: https://books.google.cz/books?id=3j8FAAAAMAAJ&hl=cs&source=gb_s_navlinks_s
- [13] YOUNG, Thomas, 1800. VII. *Outlines of experiments and inquiries respecting sound and light. By Thomas Young, M. D. F. R. S. In a letter to Edward Whitaker Gray, M. D. Sec. R. S.*
- [14] NATHAN, Alan M., 2008. The effect of spin on the flight of a baseball. *American Journal of Physics* [online]. 2008. Vol. 76, no. 2p. 119-124. [Accessed 10 January 2023]. DOI 10.1119/1.2805242. Retrieved from: <https://pubs.aip.org/aapt/ajp/article/76/2/119-124/1057105>
- [15] *Dyson.cz* [online]. [Accessed 13 January 2023]. Retrieved from: <https://www.dyson.cz/dyson-cool-tower-fan-in-white-silverFigure>
- [16] *Ventilatory-shop.cz* [online]. [Accessed 20 January 2023]. Retrieved from: <https://www.ventilatory-shop.cz/produkt/sloupovy-ventilator-dyson-am07>
- [17] *Ansys CFX-Pre User's Guide: page 197*, July 2021. Release 2021 R2. ANSYS, Inc.
- [18] PEYGHAMBARZADEH, S.M., NARAKI, M. and VERMAHMOUDI, Y. Experimental study of overall heat transfer coefficient in the application of dilute nanofluids in the car radiator. [online]. [Accessed 25 January 2023]. Retrieved from: <https://www.sciencedirect.com/science/article/pii/S1359431112007260>
- [19] QIJUN, Yu, THOMPSON, Brian E. and STRAATMAN, Anthony G. Carbon-foam finned tubes in air-water heat exchangers. [online]. [Accessed 10 February 2023]. Retrieved from: <https://www.sciencedirect.com/science/article/pii/S1359431105001869>
- [20] *Ansys CFX-Solver Modeling Guide*, July 2021. Release 2021 R2. ANSYS, Inc.

[21] STUBLEY, Gordon D., 2008. *Computational Fluid Dynamics for Fluids Engineering Design: ANSYS CFX STUDENT USER MANUAL Version 11*. University of Waterloo.

LIST OF ABBREVIATIONS AND SYMBOLS

\dot{V}	[m ³ /s]	Volumetric air flow
\dot{m}	[kg/s]	Mass air flow
A	[m ²]	Frontal surface area
A_{surf}	[m ²]	Surface area
B	[-]	Coefficient of the quadratic term
c_1	[-]	Linear coefficient for defining the radiator in ansys CFX
c_2	[-]	Quadratic coefficient for defining the radiator in Ansys CFX
$C_{asphalt}$	[-]	Rolling resistance coefficient of asphalt road
C_d	[-]	Aerodynamic resistance coefficient
$C_{defreman}$	[%]	Coefficient of efficiency of default remanufactured profile
CFD		Computational fluid dynamics
CFX		Ansys CFX fluid dynamics software
$C_{opti_measured}$	[%]	Coefficient of efficiency measured on test platform
$C_{opti_simulated}$	[%]	Coefficient of efficiency simulated
C_r	[-]	Rolling resistance coefficient
F	[N]	Force
F_{ar}	[N]	Aerodynamic resistance force
F_g	[N]	Normal (gravitational) force
F_{rr}	[N]	Rolling resistance force
F_{rrBEV}	[N]	Rolling resistance force of battery electric vehicle
F_{rrcomb}	[N]	Rolling resistance force of combustion vehicle
$H118$	[mm]	Model parameter
$H123$	[mm]	Model parameter
$H89$	[mm]	Model parameter
$H99$	[mm]	Model parameter
m_{BEV}	[kg]	Weight of the chosen battery electric vehicle
m_{comb}	[kg]	Weight of the chosen combustion vehicle
m_{in1}	[kg/s]	Mass air flow at intake on the default device with no accessories
m_{in2}	[kg/s]	Mass air flow at intake on the default device with ducting
m_{in3}	[kg/s]	Mass air flow at intake on the default device with ducting and radiator

m_{in4}	[kg/s]	Simulated mass air flow at intake on the default device with no accessories
m_{out1}	[kg]	Mass air flow at outlet on the default device with no accessories
m_{out2}	[kg/s]	Mass air flow at outlet on the default device with ducting
m_{out3}	[kg/s]	Mass air flow at outlet on the default device with ducting and radiator
m_{out4}	[kg/s]	Simulated mass air flow at outlet on the default device with no accessories
m_{out4cs}	[kg/s]	Simulated mass flow on default device with no accessories through control surfaces
$m_{out4surfaceave}$	[kg/s]	Simulated average mass flow non-directional on default device with no accessories
$m_{out4surfaceavedirectional}$	[kg/s]	simulated average mass flow directional on default device with no accessories
m_{para}	[kg/s]	Mass flow adjusted for parametric simulation
MQB		Automotive design platform
$m_{simMQBrad}$	[kg/s]	Mass flow through radiator with MQB properties
$m_{simpararad}$	[kg/s]	Mass flow, radiator directly touching the profiles
$m_{simrad1}$	[kg/s]	Mass flow through radiator at simulation with radiator and ducting
$m_{surfacedelete}$	[kg/s]	Mass flow, separation surface deleted
P	[W]	Power
p_{in}	[Pa]	Pressure inlet experiment
Q	[W]	Heat energy
s	[m]	Distance
S	[m ²]	Cross sectional area
S_{model3}	[m ²]	Frontal area of Tesla model 3
$S_{octavia}$	[m ²]	Frontal area of Skoda Octavia 4 th gen
$S_{partial1}$	[m ²]	Surface area of the parametric simulation radiator
t	[s]	Time
v	[m/s]	Relative speed of object and domain
$V124$	[mm]	Model parameter
V_{def_reman}	[m ³ /s]	Volumetric flow of default remanufactured profile
v_{in1ave}	[m/s]	Average velocity of air at intake on the default device with no accessories
v_{in2ave}	[m/s]	Average velocity of air at intake on the default device with ducting
v_{in3ave}	[m/s]	Average velocity of air at intake on the default device with ducting and radiato

v_{in4ave}	[m/s]	Simulated average velocity of air at intake on the default device with no accessories
$V_{original_base_in}$	[m ³ /s]	Volumetric flow of original test subject on MQB test platform inlet
$V_{original_device}$	[m ³ /s]	Volumetric flow of original test subject on MQB test platform outlet
$v_{out1ave}$	[m/s]	Average velocity of air at outlet on the default device with no accessories
$v_{out2ave}$	[m/s]	Average velocity of air at outlet on the default device with ducting
$v_{out3ave}$	[m/s]	Average velocity of air at outlet on the default device with ducting and radiator
$v_{out4ave}$	[m/s]	Simulated average velocity of air at outlet on the default device with no accessories
$v_{out4csave}$	[m/s]	Simulated velocity on default device with no accessories through control surfaces
$v_{out4surfaceave}$	[m/s]	Simulated average outlet velocity non-directional on default device with no accessories
$v_{out4surfaceavedi}$ <i>rectional</i>	[m/s]	Simulated outlet velocity directional on default device with no accessories
$VW\ AG$		Volkswagen group
α_k	[W · m ⁻² · K ⁻¹]	Heat transfer coefficient
Δt	[K]	Temperature difference
Δx	[mm]	Depth of the porous material
ρ	[kg/m ³]	Domain density

ATTACHMENTS LIST

- Attachment 1. Calibration protocol
- Attachment 2. MQB assembly air speed distribution, low power
- Attachment 3. MQB assembly air speed distribution, medium power
- Attachment 4. Mass flow measurement raw data
- Attachment 5. Velocity at 215 mm height for the test subject turbine base
- Attachment 6. Velocity at 395 mm height for the test subject turbine base
- Attachment 7. Velocity at 595 mm height for the test subject turbine base
- Attachment 8. Velocity at 595mm height for the test subject turbine base with variable measurement device position relative to the base
- Attachment 9. Geometry of the test subject
- Attachment 10. Cross section detail of the test subject
- Attachment 11. Inlet detail of the test subject
- Attachment 12. The cross section swept along the base curve
- Attachment 13. Full mesh of the test subject
- Attachment 14. Inlet detail on the test subject's mesh
- Attachment 15. Channel detail on the test subject's mesh
- Attachment 16. Cross sectional detail on the test subject's mesh
- Attachment 17. Mesh elements with the worst metrics
- Attachment 18. Test subject full size simulation convergency
- Attachment 19. Test subject full size simulation residuals
- Attachment 20. Yplus distribution on the single side parametric model
- Attachment 21. Individual measurements for the primary curvature adaptation
- Attachment 22. Individual measurements for channel adaptation
- Attachment 23. Individual measurements for secondary curvature adaptation
- Attachment 24. Individual measurements for the separation edge adaptation
- Attachment 25. Individual measurements for the profile length adaptation
- Attachment 26. Radiator distance adaptation
- Attachment 27. Profile length adaptation
- Attachment 28. Separation edge curvature and profile distance adaptation
- Attachment 29. Separation edge refinement
- Attachment 30. Axis distance refinement
- Attachment 31. Mass flow efficiency
- Attachment 32. Back pressure and mass air flow through the radiator at speed
- Attachment 33. Mass air flow through radiator with the inlet compressor running at speed
- Attachment 34. Optimised design manufactured test
- Attachment 35. Remanufactured optimised profile testing apparatus

	Český metrologický institut Okružní 31, 638 00 Brno tel. +420 545 555 111 www.cmi.cz		
Kalibrační laboratoř č. 2202 akreditovaná Českým institutem pro akreditaci, o.p.s. podle ČSN EN ISO/IEC 17025:2018			
Pracoviště:	Oblastní inspektorát Brno, Okružní 31, 638 00 Brno Oddělení primární etalonáže průtoku kapalin, rychlosti proudění a tepla tel. +420 545 555 111, fax. +420 545 555 183		
<h2>KALIBRAČNÍ LIST</h2>			
<h3>6015-KL-P0911-22</h3>			
Datum vystavení:	9. prosince 2022	List 1 ze 2 listů	
Zákazník:	Hanon Systems Autopal Services s.r.o. Lužická 984/14 741 01 Nový Jičín		
Uživatel:	-		
Měřidlo:	Anemometr vrtulkový		
Výrobce:	Ahlborn		
Typ:	FV A915-S120		
Výrobní číslo:	S35135		
Ostatní údaje:	Vyhodnocovací jednotka Ahlborn, Almemo 28909, výr.č. H16030047		
Výsledky kalibrace byly získány za podmínek a s použitím postupů uvedených v tomto kalibračním listě a vztahují se pouze ke kalibrovanému měřidlu a k době a místu provedení kalibrace.			
Datum kalibrace:	9. prosince 2022		
Kalibraci provedl:	Vedoucí oddělení:		
Ing. Jan Sluše, Ph.D.		Mgr. Jindřich Bílek, Ph.D.	
<i>Tento dokument nesmí být bez písemného souhlasu provádějící laboratoře rozmnožován jinak než v celkovém počtu listů.</i>			

Attachment 1. Calibration protocol page 1/2

KALIBRAČNÍ LIST

6015-KL-P0911-22

List 2 ze 2 listů

Metrologická návaznost: Laserový dopplerovský anemometr ILA fp50f-us, ser. č. 738, kalibrováno PTB, kalibrační certifikát PTB-1.41-4098449;

Měření jsou metrologicky návazná na (mezi)národní etalony.

Kalibrační postup: Metoda dle pracovního postupu č. 615-MP-C147 za použití aerodynamického tunelu Westenberg Engineering typ WK 845050-G.

Místo kalibrace: ČMI Ol Brno, Okružní 31, 638 00 Brno

Podmínky prostředí: Teplota vzduchu ($20,0 \pm 0,5$) °C; RV vzduchu (41 ± 1) %; tlak vzduchu (967 ± 2) hPa

Podmínky kalibrace: Teplota vzduchu v tunelu ($20,0 \pm 0,5$) °C; RV vzduchu v tunelu (41 ± 1) %

Výsledky kalibrace:

v_E	v_M	E	U(E)
m/s	m/s	m/s	m/s
2,011	2,069	0,058	0,016
6,053	5,981	-0,072	0,030
12,065	11,698	-0,367	0,060
18,086	17,277	-0,810	0,090
20,10	19,14	-0,95	0,10

v_E ... rychlost měřená etalonem

v_M ... rychlost měřená měřidlem

E ... chyba měřidla

U(E) ... kombinovaná rozšířená nejistota chyby měřidla

Standardní nejistota měření byla určena v souladu s dokumentem EA-4/02 M:2022. Uvedená rozšířená nejistota měření je součinem standardní nejistoty měření a koeficientu k , který odpovídá pravděpodobnosti pokrytí přibližně 95 %, což pro normální rozdělení odpovídá koeficientu rozšíření $k = 2$.

Konec kalibračního listu.

Český metrologický institut
Oblastní inspektorát Brno
Okružní 31
638 00 Brno
-18-

Tento dokument nesmí být bez písemného souhlasu provádějící laboratoře rozmnožován jinak než v celkové počtu listů.

		<u>Position X [mm]</u>													
		2,5	5	10	15	20	25	30	35	40	45	50	55	60	62
<u>Position Y [mm]</u>	44	0,18	0,19	0,4	0,54	0,7	0,86	0,96	1,02	1,05	0,97	0,89	0,73	0,59	0,58
	40	0,34	0,34	0,43	0,69	0,83	1,02	1,11	1,15	1,16	1,08	0,94	0,8	0,62	0,6
	35	0,41	0,46	0,61	0,84	1,02	1,15	1,12	1,08	1,08	1,04	1,03	0,91	0,76	0,71
	30	0,42	0,4	0,45	0,77	0,99	1,05	1,03	1	0,95	1,07	1,13	1	0,69	0,61
	25	0,38	0,4	0,61	0,77	0,99	1,01	1,04	0,91	0,91	1,07	0,99	0,99	0,75	0,69
	20	0,39	0,47	0,58	0,88	1,03	1,09	0,97	0,85	0,91	1,02	1,02	0,98	0,79	0,76
	15	0,4	0,41	0,59	0,81	0,96	1,07	1	0,97	0,96	1,08	1,02	0,91	0,76	0,73
	10	0,1	0,32	0,47	0,64	0,9	0,99	1,06	1,08	1,08	1,06	0,98	0,85	0,66	0,64
	5	0	0	0,33	0,52	0,76	0,86	1,01	1,05	1,07	0,93	0,83	0,69	0,5	0,5
	2,5	0	0	0,36	0,5	0,67	0,8	0,9	1,03	0,96	0,84	0,78	0,57	0,47	0,39

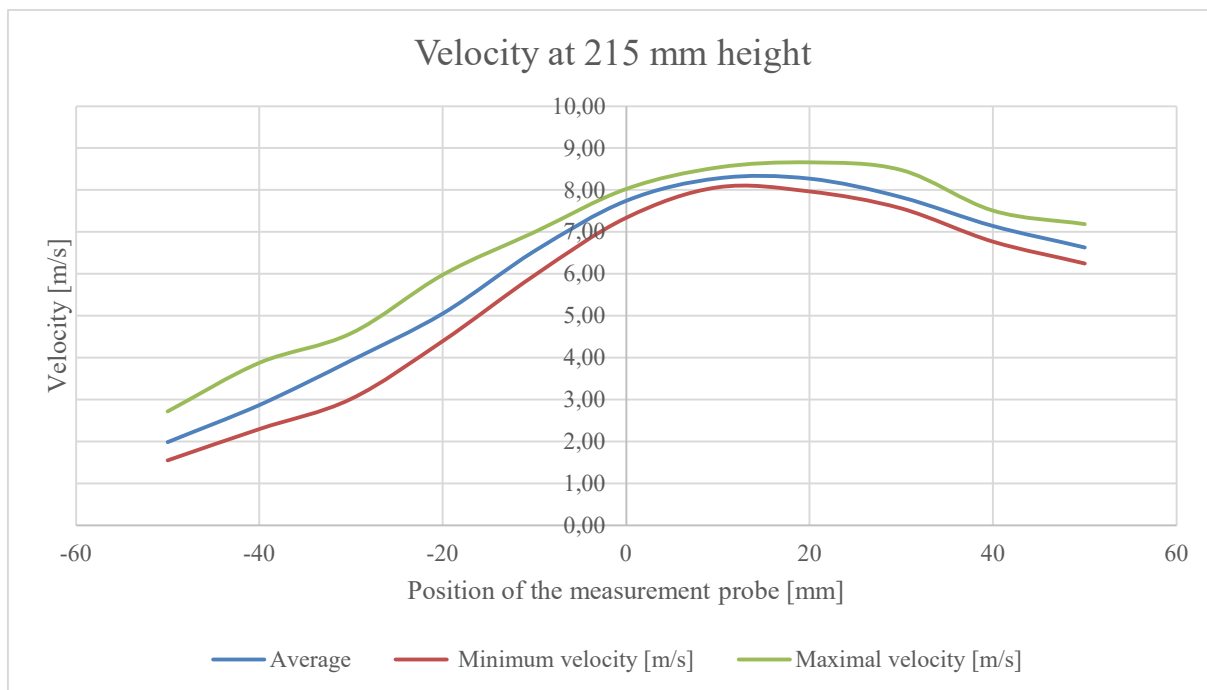
Attachment 2. MQB assembly air speed distribution, low power

		<u>Position X [mm]</u>													
		2,5	5	10	15	20	25	30	35	40	45	50	55	60	62
<u>Position Y [mm]</u>	44	0,69	0,79	1,15	1,68	2,44	3,28	4,03	4,57	4,71	4,14	3,21	2,36	1,91	1,89
	40	0,71	0,83	1,26	2,08	2,95	3,89	4,55	4,74	4,82	4,41	3,79	2,85	2,08	2,01
	35	0,79	0,94	1,6	2,44	3,62	4,36	4,53	4,64	4,6	4,55	4,31	3,46	2,54	2,44
	30	1,05	1,08	1,71	2,88	4,18	4,45	4,33	3,91	3,88	4,34	4,39	4,08	2,87	2,78
	25	0,96	1,09	1,88	3,07	4,19	4,35	3,84	2,78	2,85	4,07	4,34	4,22	2,99	2,87
	20	0,91	1,18	1,87	3,05	4,16	4,37	4,11	2,99	3,2	4,07	4,43	4,24	3,02	2,86
	15	0,88	1	1,65	2,73	4,04	4,53	4,46	4,26	4,39	4,54	4,47	3,89	2,74	2,61
	10	0,72	0,81	1,38	2,2	3,34	4,29	4,58	4,67	4,74	4,63	4,24	3,24	2,37	2,25
	5	0,66	0,77	1,13	1,78	2,66	3,55	4,5	4,75	4,66	4,03	3,4	2,51	1,72	1,66
	2,5	0,57	0,65	1,07	1,5	2,39	3,16	3,78	3,98	3,6	3,4	2,78	2,07	1,55	1,34

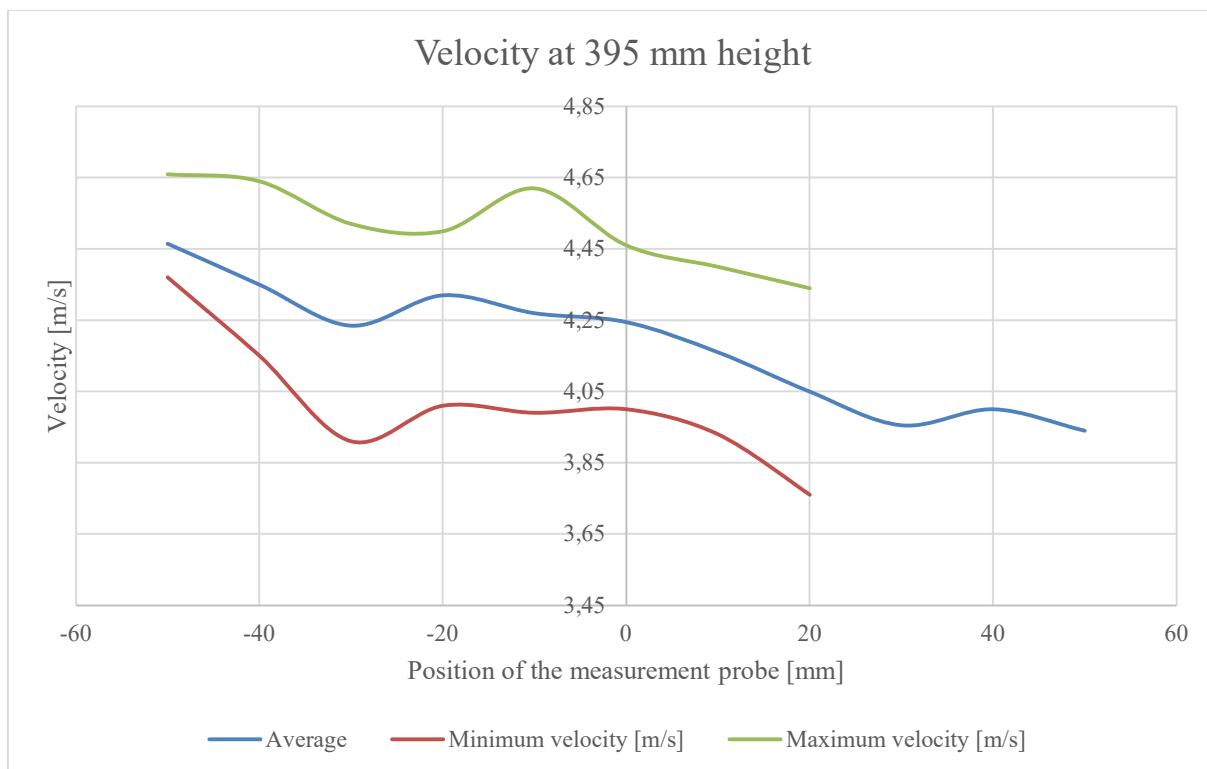
Attachment 3. MQB assembly air speed distribution, medium power

Hieght [mm]	Angle Z [°]	Excentricity [mm]	Anemometer angle [°]	minimum [m/s]	Maximum [m/s]	average [m/s]
395	0	50	1,145762838	3,85	4,03	3,94
395	0	40	0,600219542	3,99	4,01	4
395	0	30	0,245551837	3,92	3,99	3,955
395	0	20	0,572938698	3,76	4,34	4,05
395	0	10	0,709340075	3,93	4,4	4,16
395	0	0	0,545657593	4	4,46	4,245
395	0	-10	0,436530826	3,99	4,62	4,27
395	0	-20	1,091216225	4,01	4,5	4,32
395	0	-30	0,518376242	3,91	4,52	4,235
395	0	-40	0,572938698	4,15	4,64	4,35
395	0	-50	0,736619435	4,37	4,66	4,465
215	0	-50	0,736619435	1,55	2,72	1,99
215	0	-40	0,572938698	2,3	3,88	2,875
215	0	-30	0,054567393	3,02	4,58	3,935
215	0	-20	0,436530826	4,4	5,98	5,06
215	0	-10	0,463812846	5,97	7	6,545
215	0	0	0,600219542	7,34	8,03	7,75
215	0	10	0,054567393	8,07	8,54	8,285
215	0	20	0,763898461	7,97	8,66	8,275
215	0	30	0,818455462	7,56	8,48	7,83
215	0	40	0,381966205	6,77	7,51	7,145
215	0	50	0,381966205	6,25	7,19	6,635
595	0	50	0,381966205	3,12	3,61	3,375
595	0	40	0,081851058	3,23	3,63	3,385
595	0	30	0,736619435	3,28	3,69	3,535
595	0	20	0,190985224	3,69	3,97	3,805
595	0	10	1,282120067	3,95	4,03	4,14
595	0	0	0,054567393	4,3	4,6	4,42
595	0	-10	0,982117163	4,37	4,84	4,64
595	0	-20	0,600219542	4,61	5	4,79
595	0	-30	1,254849734	4,74	5,08	4,895
595	0	-40	0,136418265	4,81	5,26	4,995
595	0	-50	0,245551837	4,56	5,28	4,985
595	90	-50	1,173035372	4,3	5,06	4,705
595	90	-40	0,081851058	4,27	4,96	4,63
595	90	-30	0,491094655	4,33	4,98	4,65
595	90	-20	0,354683628	4,32	4,83	4,515
595	90	-10	0,21826858	4,19	4,57	4,375
595	90	0	0,409248608	4,15	4,44	4,29
595	90	10	0,436530826	4,01	4,28	4,1
595	90	20	0,190985224	3,85	4,3	4,035
595	90	30	0,027283702	3,75	4,23	3,995
595	90	40	0,791177141	3,77	4,25	3,95
595	90	50	0,436530826	3,79	4,2	3,975
595	45	50	0,027283702	3,68	4,14	3,8
595	45	40	0,081851058	3,59	4,22	3,86
595	45	30	0,136418265	3,86	4,28	4
595	45	20	0,436530826	3,99	4,52	4,21
595	45	10	0,272834983	4,22	4,5	4,38
595	45	0	0,136418265	4,23	4,61	4,43
595	45	-10	0,381966205	4,33	4,65	4,475
595	45	-20	0,518376242	4,41	4,79	4,575
595	45	-30	0,21826858	4,33	4,73	4,535
595	45	-40	0,163701782	4,41	4,83	4,615
595	45	-50	0,463812846	4,46	4,86	4,645

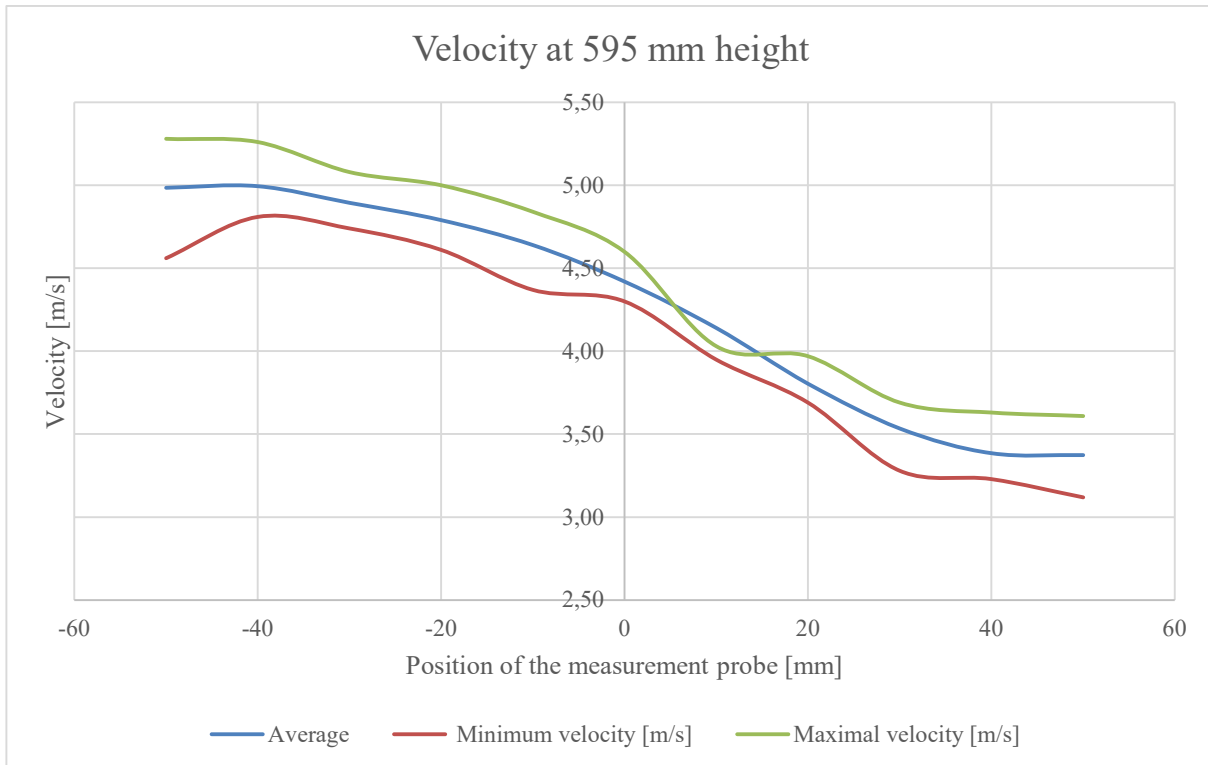
Attachment 4. Mass flow measurement raw data



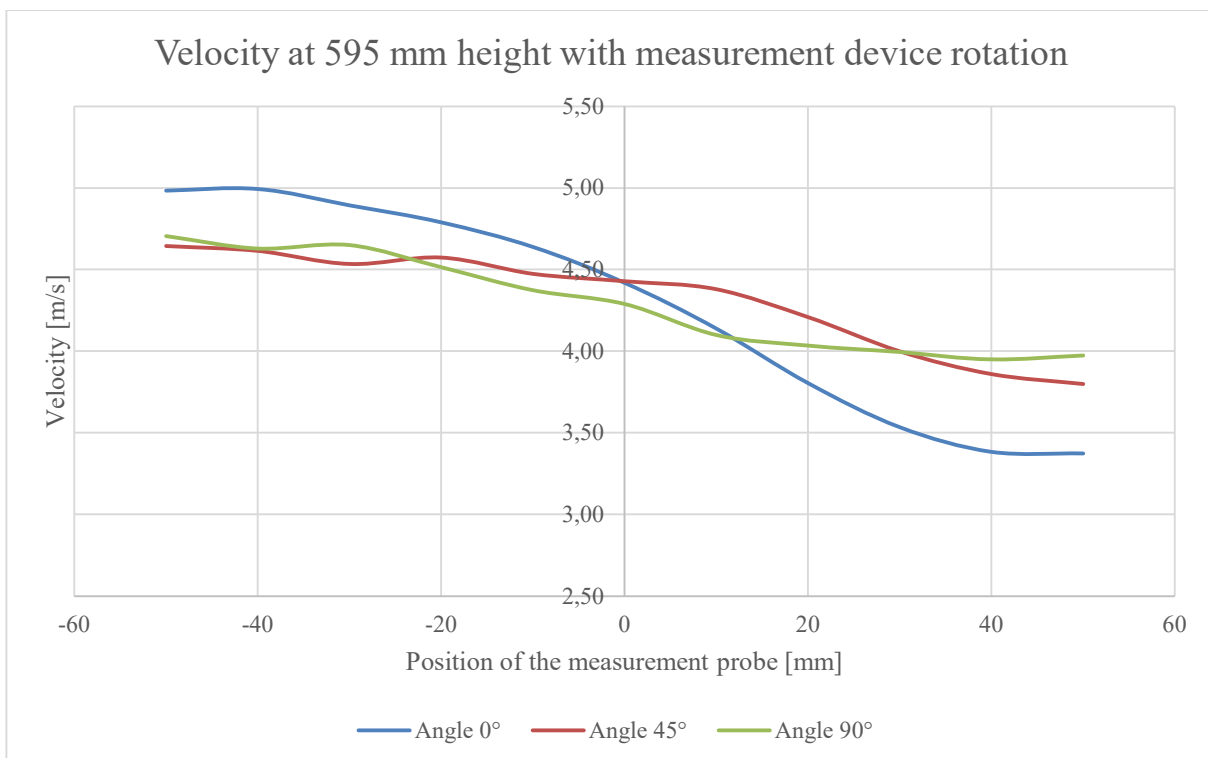
Attachment 5. Velocity at 215 mm height for the test subject turbine base



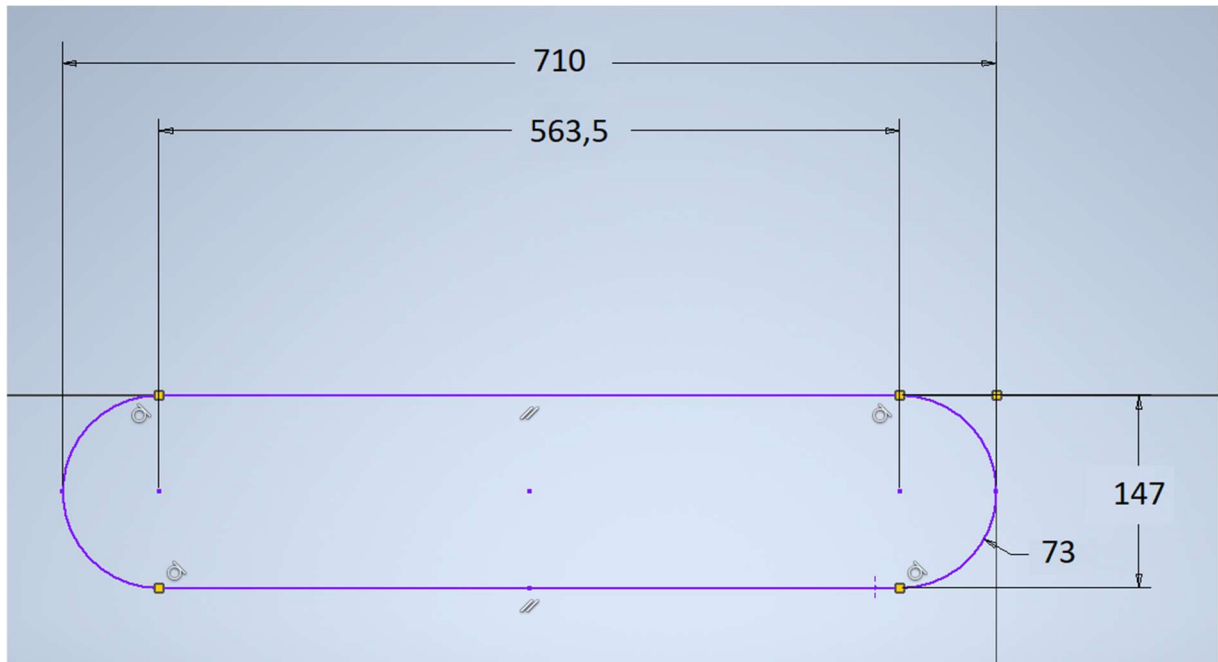
Attachment 6. Velocity at 395 mm height for the test subject turbine base



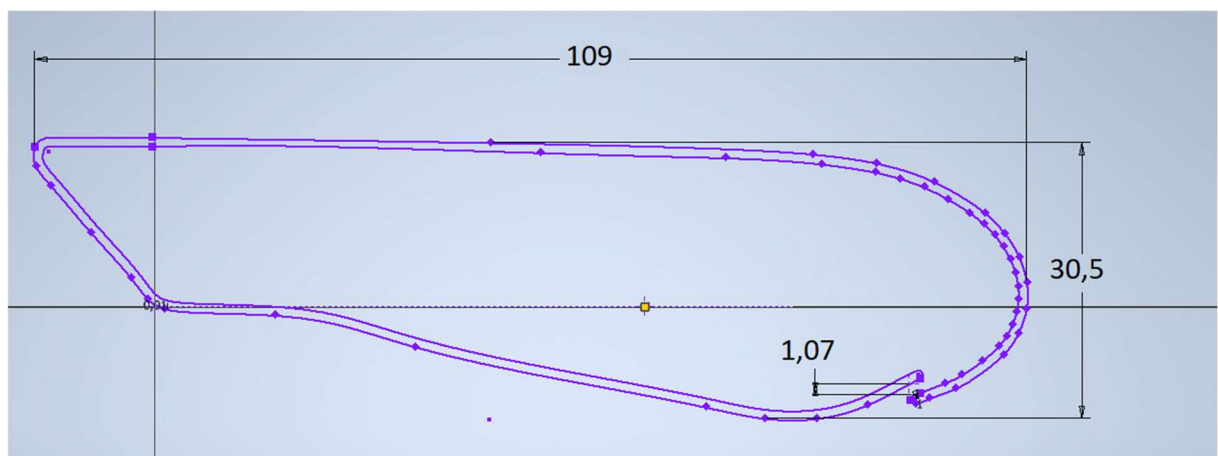
Attachment 7. Velocity at 595 mm height for the test subject turbine base



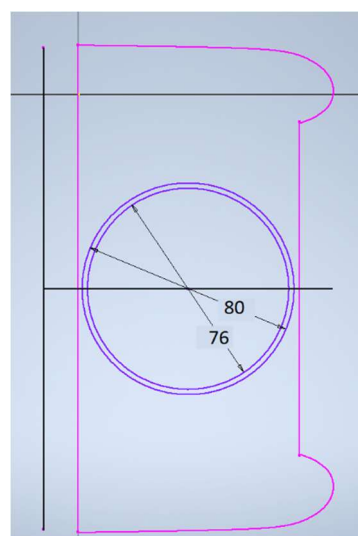
Attachment 8. Velocity at 595mm height for the test subject turbine base with variable measurement device position relative to the base



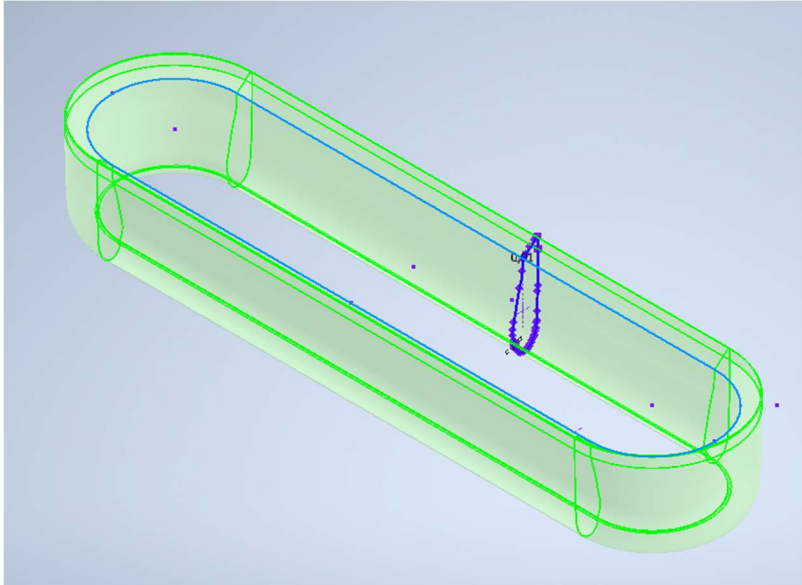
Attachment 9. Geometry of the test subject



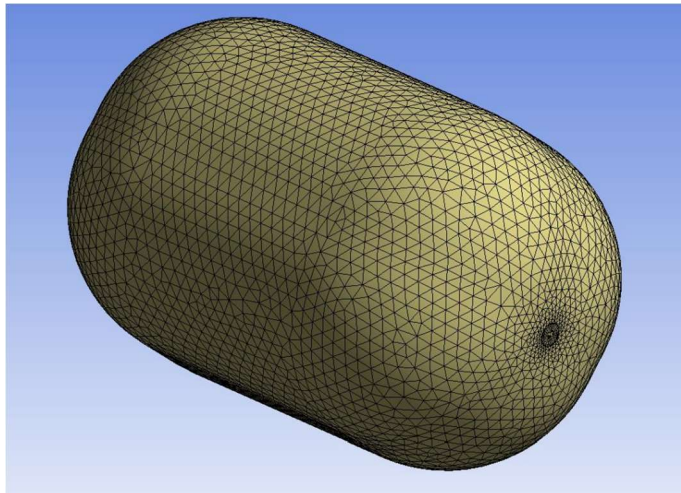
Attachment 10. Cross section detail of the test subject



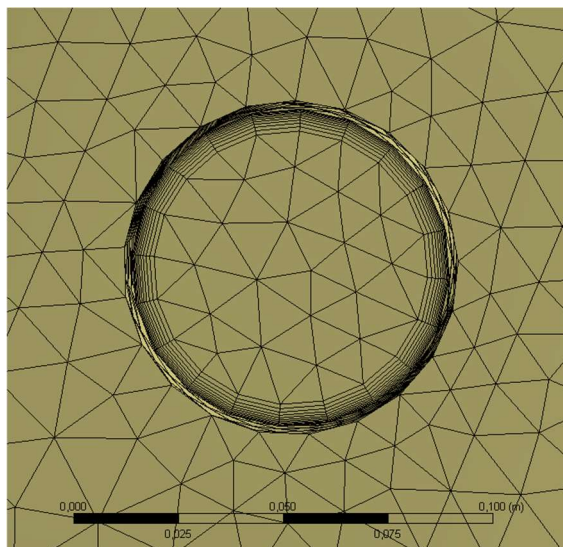
Attachment 11. Inlet detail of the test subject



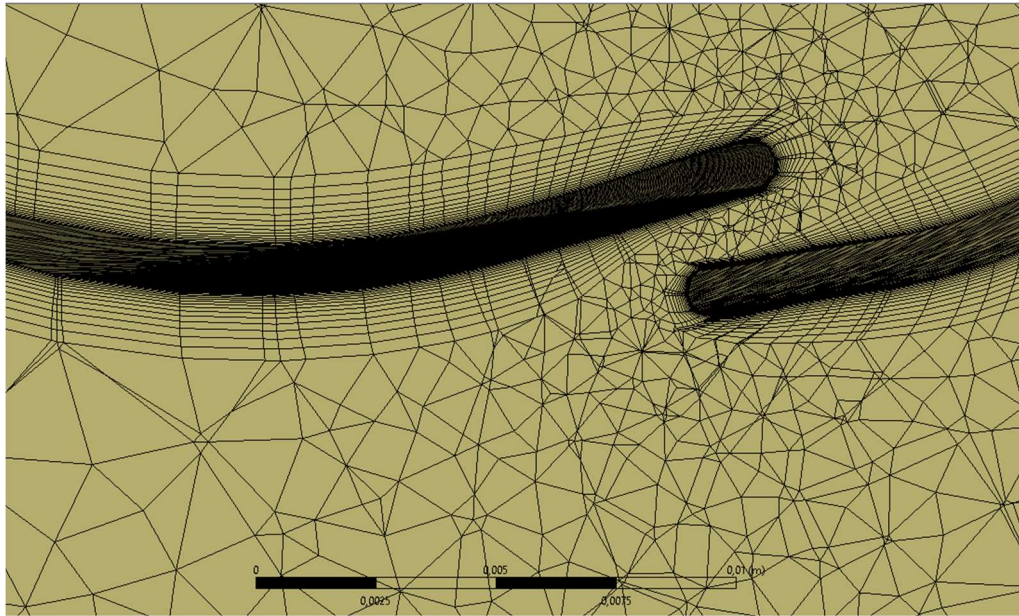
Attachment 12. The cross section swept along the base curve



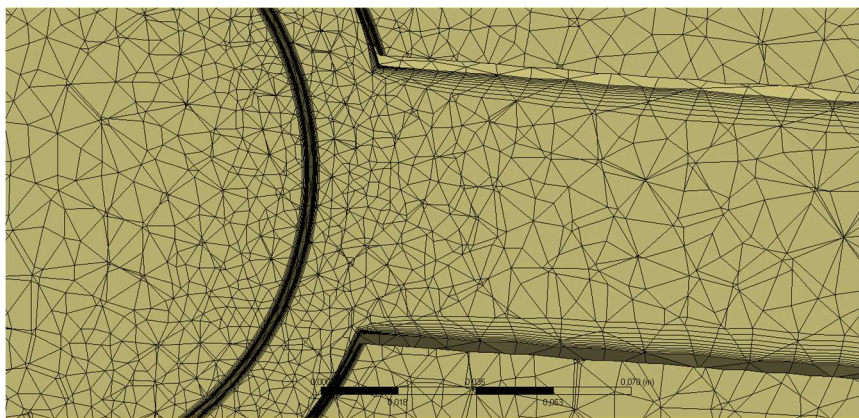
Attachment 13. Full mesh of the test subject



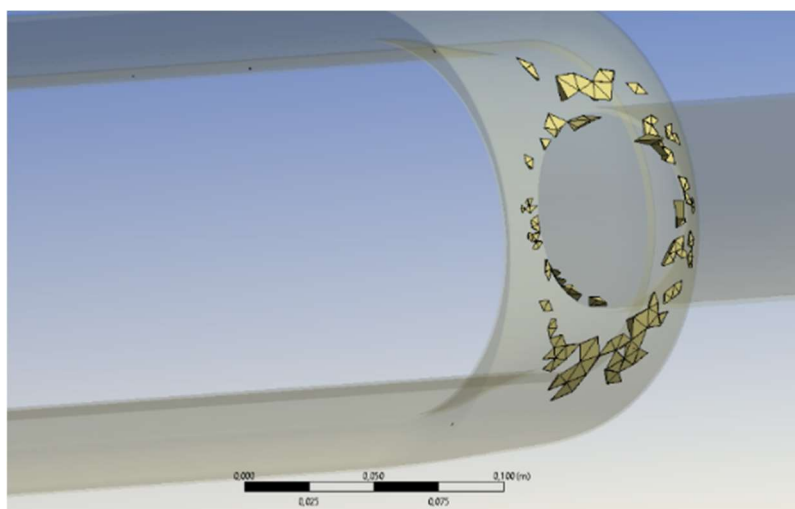
Attachment 14. Inlet detail on the test subject's mesh



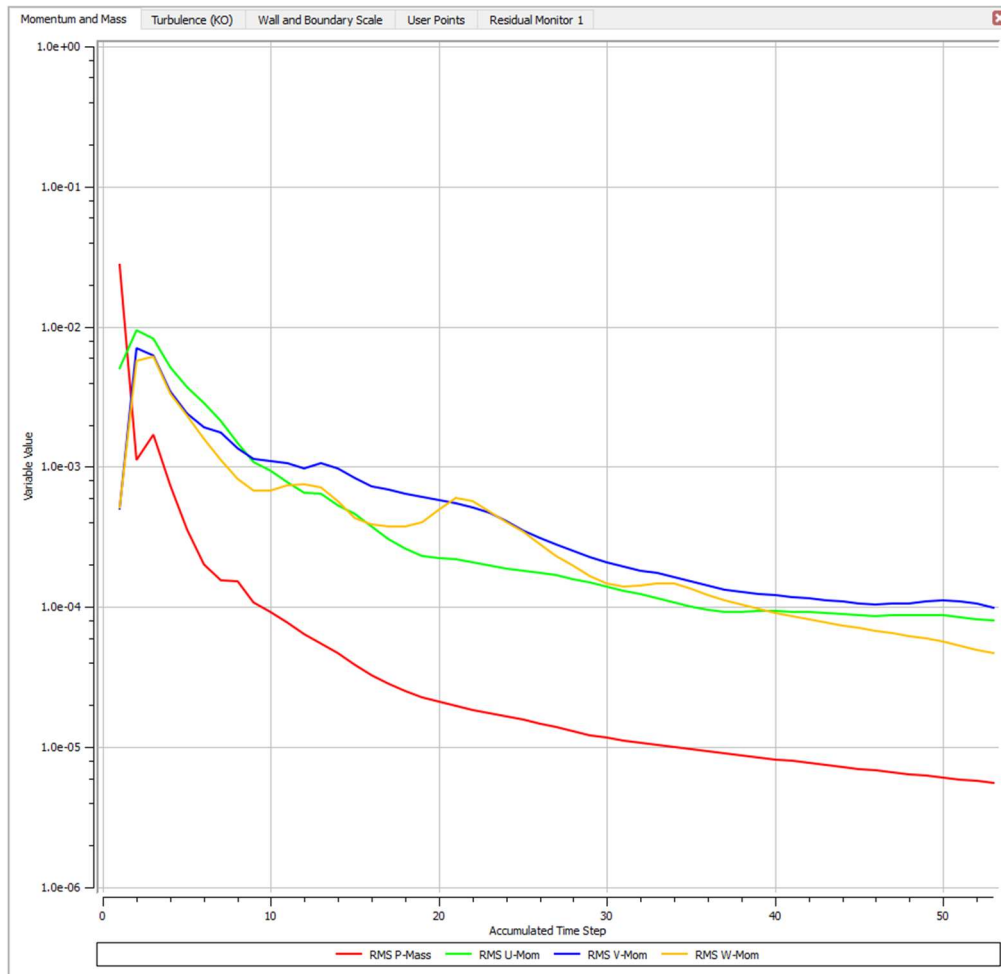
Attachment 15. Channel detail on the test subject's mesh



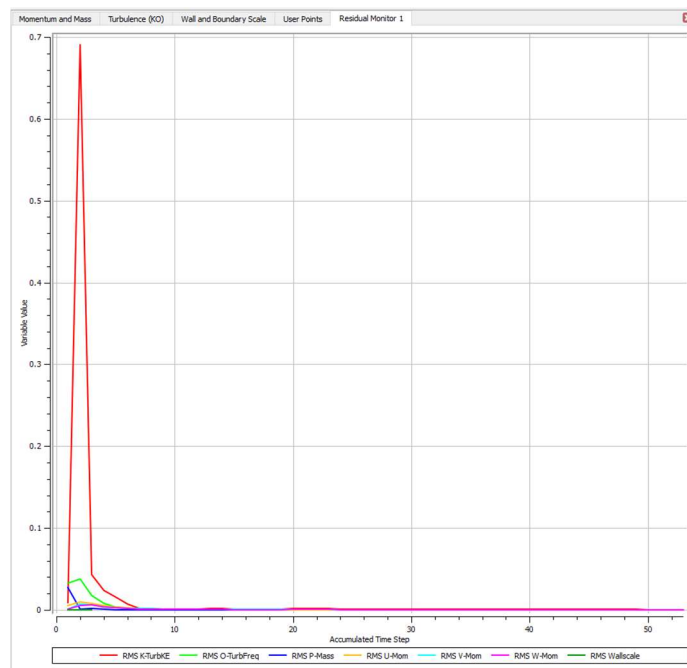
Attachment 16. Cross sectional detail on the test subject's mesh



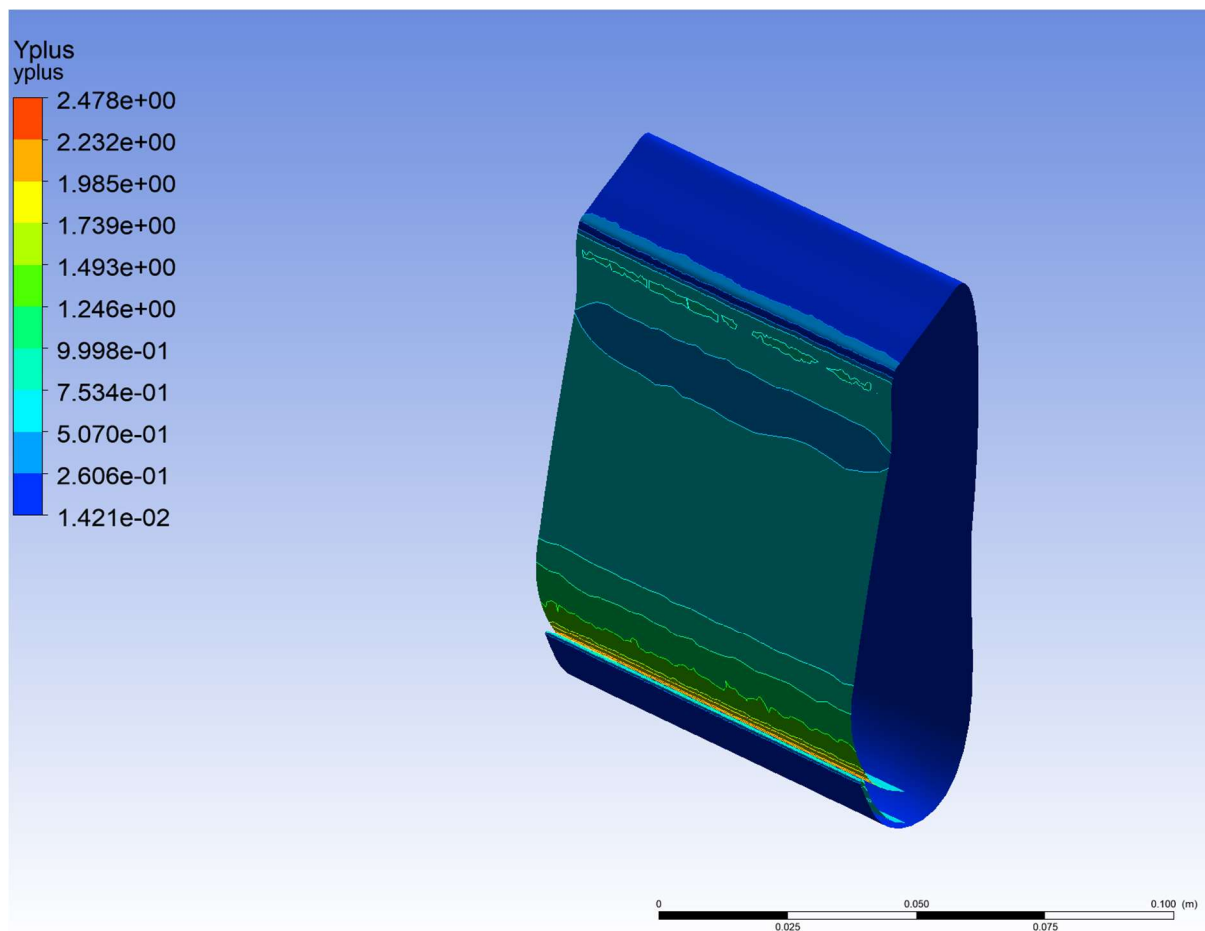
Attachment 17. Mesh elements with the worst metrics



Attachment 18. Test subject full size simulation convergency



Attachment 19. Test subject full size simulation residuals



Attachment 20. Yplus distribution on the single side parametric model

H89 [mm]	Mass air flow [kg/s]	Inlet pressure [Pa]	Channel width [mm]
11,25	0,01565	507	1,28
11,875	0,01627	607	1,17
12,5	0,01717	740	1,07
13,125	0,01767	917	0,96
13,75	0,01882	1150	0,84

Attachment 21. Individual measurements for the primary curvature adaptation

Iteration	H123 [mm]	V124 [mm]	Channel width [mm]	Inlet Pressure [Pa]	Massflow radiator [kg/s]
0 - default	10,25	2	1,07	750	0,01742
1	9,225	1	0,75	3153	0,02347
2	10,6125	1	1,43	387	0,01461
3	12	1	1,53	260	0,01262
4	9,91875	2	0,91	1605	0,02034
5	10,6125	2	1,0	438	0,01543
6	11,30625	2	1,21	259	0,01280
7	9,225	3	0	N/A	N/A
8	9,91875	3	0,26	9956	0,02893
9	10,6125	3	0,93	1064	0,01835
10	11,30625	3	1,08	413	0,01474
11	12	3	1,21	311	0,01405
12	9,91875	4	0	N/A	N/A
13	10,6125	4	0,40	4441	0,02368
14	11,30625	4	0,97	800	0,01728
15	9,225	5	0	N/A	N/A
16	10,6125	5	0	N/A	N/A
17	12	5	1,01	602	0,01621

Attachment 22. Individual measurements for channel adaptation

H99 [mm]	Mass air flow [kg/s]	Inlet Pressure [Pa]
38	0,015951	740,1
40,125	0,016236	739,65
42,25	0,017104	740,06
44,375	0,016607	740,03
46,5	0,015195	741,6

Attachment 23. Individual measurements for secondary curvature adaptation

H118 [mm]	Inlet pressure [Pa]	Mass air flow [kg/s]
36,63	741,12	0,015274
38,665	740,78	0,017233
40,7	739,68	0,016982
42,735	737,92	0,016039
44,77	739,6	0,014347

Attachment 24. Individual measurements for the separation edge adaptation

Parameter V141 [mm]	Inlet pressure [Pa]	Mass air flow [kg/s]	Actual profile length [mm]
1	880	0,0160434	95
8,25	877	0,0153174	87,75
15,5	875	0,0148575	80,5
22,75	875	0,014446	73,25
30	870	0,0126447	66

Attachment 25. Individual measurements for the profile length adaptation

Radiator distance [mm]	Mass air flow [kg/s]	Inlet pressure [Pa]
Direct contact	0,0414637	960,689
1,8	0,0400516	953,812
3,7	0,0393195	940,788
5,5	0,0384513	954,504
7,4	0,0375846	934,483

Attachment 26. Radiator distance adaptation

Profile length [mm]	Mass air flow [kg/s]	Inlet Pressure [Pa]
66,5	0,0418468	952,296
69	0,0420941	954,479
71,5	0,039152	944,384
74	0,0383076	949,106
76,5	0,0382736	934,934

Attachment 27. Profile length adaptation

Parameter H253 [mm]	Mirror parameter P27 [mm]	Mass air flow [kg/s]	Inlet Pressure [Pa]
6	38,5	0,0445804	946,762
4	38,5	0,0433816	948,709
8	38,5	0,043512	958,832
6	27	0,0278443	940,694
6	50	0,0418983	965,606
4	27	0,0283036	938,471
8	27	0,0301575	951,046
4	50	0,0412796	957,157
8	50	0,0405862	968,38

Attachment 28. Separation edge curvature and profile distance adaptation

Parameter H253 [mm]	Mass air flow [kg/s]	Inlet Pressure [Pa]
6,6	0,043981	959,607
6,3	0,0442846	956,92
6	0,044387	958,232
5,7	0,0443991	956,561
5,4	0,0447178	955,678
5,05	0,0446785	954,357
4,7	0,0446015	947,625
4,35	0,0444835	945,924
4	0,0445088	941,172

Attachment 29. Separation edge refinement

Axis distance [mm]	Mass air flow [kg/s]	Inlet Pressure [Pa]
42,35	0,0423822	943,642
40,425	0,0443564	942,019
38,5	0,0445181	951,941
36,575	0,0439585	967,703
34,65	0,0440286	931,595

Attachment 30. Axis distance refinement

Mass flow inlet [kg/s]	Mass flow outlet [kg/s]	Flow efficiency [-]	Inlet pressure [Pa]
0,0015	0,007296	1,62	31,327
0,003	0,014558	1,62	113,66
0,0045	0,02177	1,61	240,79
0,006	0,028993	1,61	414,15
0,0075	0,0362362	1,61	636,149
0,0090938	0,0439948	1,61	935
0,0105	0,051265	1,63	1226,3
0,012	0,057862	1,61	1617,2
0,0135	0,065325	1,61	2032,2
0,015	0,072481	1,61	2489
0,0165	0,079594	1,61	2992,4

Attachment 31. Mass flow efficiency

Velocity [km/h]	Mass air flow through radiator [kg/s]	Assembly back pressure [Pa]
0	0	0
30	0,11455	509,447
50	0,190917	1390,36
70	0,267284	2702,86
90	0,34365	4450,74
110	0,420017	6620,67
130	0,496383	9235,12
150	0,57275	12270,6

Attachment 32. Back pressure and mass air flow through the radiator at speed

Velocity [km/h]	Inlet [kg/s]	Mass air flow through radiator [kg/s]	Assembly back pressure [Pa]	Average velocity at rad_out [m/s]	Profile Pressure [Pa]
30	0,003	0,12355	612	10,483	493
30	0,0090938	0,14183	662,65	12,038	1390
30	0,0165	0,16405	677,11	13,923	3456
50	0,003	0,19992	1050	16,963	1585
50	0,0090938	0,2182	1744	18,517	2067
50	0,0165	0,24042	1854	20,405	4234
70	0,003	0,27628	2979	23,443	1831
70	0,0090938	0,29457	3295	24,996	3046
70	0,0165	0,31678	5291	26,886	3493
90	0,003	0,35265	4785	29,925	2831
90	0,0090938	0,37093	5309	31,476	4297
90	0,0165	0,39315	6658	33,365	5606
110	0,003	0,42902	7032	36,405	4066
110	0,0090938	0,4473	7736	37,956	5774
110	0,0165	0,46952	8181	39,845	8335
130	0,003	0,50538	9706	42,885	5568
130	0,0090938	0,52366	10590	44,436	7499
130	0,0165	0,54588	11221	46,324	10272

Attachment 33. Mass air flow through radiator with the inlet compressor running at speed

Profile length [mm]	Volumetric air in [m3/s]	Average outlet speed [m/s]	Volumetric air out [m3/s]	Efficiency [-]	Volumetric flow per 100mm of the profile [m3/s]
440	0,0133	0,9733333	0,03126347	2,35	0,003553
133	0,0133	2,52333	0,024867	1,87	0,009348
88	0,0133	3,345556	0,021492	1,61	0,012211
52	0,0133	4,76667	0,018094	1,36	0,017398

Attachment 34. Optimised design manufactured test



Attachment 35. Remanufactured optimised profile testing apparatus